Clemson University
TigerPrints

All Dissertations | Dissertations

12-2017

Microwave Photonics for Distributed Sensing

Liwei Hua
Clemson University

Follow this and additional works at: https://tigerprints.clemson.edu/all_dissertations

Recommended Citation
Hua, Liwei, "Microwave Photonics for Distributed Sensing" (2017). *All Dissertations*. 2062.
https://tigerprints.clemson.edu/all_dissertations/2062

This Dissertation is brought to you for free and open access by the Dissertations at TigerPrints. It has been accepted for inclusion in All Dissertations by an authorized administrator of TigerPrints. For more information, please contact kokeefe@clemson.edu.

MICROWAVE PHOTONICS FOR DISTRIBUTED SENSING

A Dissertation
Presented to
the Graduate School of
Clemson University

In Partial Fulfillment
of the Requirements for the Degree
Doctor of Philosophy
Electrical and Computer Engineering

---

by
Liwei Hua
December 2017

Accepted by:
Dr. Hai Xiao, Committee Chair
Dr. Liang Dong
Dr. Eric G. Johnson
Dr. Lawrence C. Murdoch

ABSTRACT

In the past few years, microwave-photonics technologies have been investigated for optical fiber sensing. By introducing microwave modulation into the optical system, the optical detection is synchronized with the microwave modulation frequency. As a result, the system has a high SNR and thus an improved detection limit. In addition, the phase of the microwave-modulated light can be obtained and Fourier transformed to find the time-of-arrival information for distributed sensing.

Recently, an incoherent optical-carrier-based microwave interferometry (OCMI) technique has been demonstrated for fully distributed sensing with high spatial resolution and large measurement range. Since the modal interference has little influence on the OCMI signal, the OCMI is insensitive to the types of optical waveguide. Motivated by the needs of distributed measurement in the harsh environment, in the first part of this paper, several OCMI-based sensing systems were built by using special multimode waveguides to perform sensing for heavy duty applications.

Driven by an interest on the high-resolution sensing, in the second part of the paper, I propose a coherence-gated microwave photonics interferometry (CMPI) technique, which uses a coherent light source to obtain the optical interference signal from cascaded weak reflectors. The coherence length of the light source is carefully chosen or controlled to gate the signal so that distributed sensing can be achieved. The experimental results indicate that the strain resolution can be better than 0.6 με using a Fabry-Perot interferometer (FPI)

with a cavity length of 1.5 cm. Further improvement of the strain resolution to the 1 nε level is achievable by increasing the cavity length of the FPI to over 1m.

The CMPI has also been utilized for distributed dynamic measurement of vibration by using a new signal processing method. The fast time-varying optical interference intensity change induced by the sub-scan rate vibration is recorded in the frequency domain. After Fourier transform, distinctive features are shown at the vibration location in the time domain signal, where the vibration frequency and intensity can be retrieved. The signal processing method supports vibration measurement of multiple points with the measurable frequency of up to 20 kHz.

DEDICATION

To:

My parents and husband!

ACKNOWLEDGMENTS

There are many thanks to my advisor, Dr. Hai Xiao. I am very grateful that he took me on as a graduate student and drove me back to the orbit of scientific research. During my study in this group, he provided me tremendous amount of supports and insightful advices for the research, writing, and beyond. He has been very patient and encouraging to me, especially in the days after I have my baby. Without him, my research would never have been reached so far, and my life would be less interesting because of missing the ingredient of "in lab creating".

I also would like to thank Dr. Liang Dong, Dr. Eric. G. Johnson, and Dr. Lawrence C. Murdoch for taking their valuable time and being my committee member. I appreciate their advices and questions on my dissertation. Here's a special thanks to Dr. Lawrence C. Murdoch for bringing those sensing challenges to me, which pushed me to break though the research bottle necks.

I would like to thank all the lab mates for their support and help. Very lucky that I could have those talent guys on the same page with me, and we could discuss together and solve the problems together. The completion of all these research projects are really the result of hard working and team collaboration of all my group members.

Finally, I want to thank my husband, Wenzhe Li, for being not only a sweet life company, great dad, but also a wonderful listener and consultant of my research; thank my parents and parents in law, for their endless love, unconditional support, and encouraging; thank my little girl, Aira M. Li, for doing the excellent job of being cute.

TABLE OF CONTENTS

Page

LIST OF TABLES

Figure Page

LIST OF FIGURES

Figure Page

List of Figures (Continued)

Figure Page

List of Figures (Continued)

Figure Page

List of Figures (Continued)

Figure Page

Figure Page

List of Figures (Continued)

Figure Page

CHAPTER ONE

INTRODUCTION

1.1 Optical fiber distributed sensing technologies

One of the unique advantages of optical fiber sensing is its ability to acquire spatially distributed information. The combination of ultra-low loss optical fibers and high-speed electronics now make it possible to continuously monitor spatially varying parameters over tens of kilometers or longer. The applications extend from structural health monitoring (SHM) [1,2] to other areas such as the monitoring of geophysical properties [3], chemical/biological species [4], and physiological parameters [5].

In general, distributed optical fiber sensing can be categorized into two groups. One is the so-called quasi-distributed sensing, which cascades many discrete sensors (e.g., fiber Bragg gratings (FBGs) [6]) along the fiber. These cascaded sensors share the same signal processing instrument and sample the fiber at discrete points. It has the advantages of flexible deployment, multi-agent capability and high detection sensitivity. However, most of the existing systems can only multiplex a limited number of sensors (hundreds of sensors at most). Another category is the so-called fully distributed optical fiber sensing technology, which is commonly based on the measurement of back scattering of various kinds. The scatterings can be the Rayleigh scattering of the fiber or the nonlinear signals such as Raman and Brillouin scatterings [7].

In a conventional optical time domain reflectometry (OTDR) system, a short broadband optical pulse (20-2000 ns) launches into an optical fiber and the back Rayleigh scatterings are recorded by a photodetector in the order of time of arrival [8]. The backscattering power decreases exponentially as function of time (distance) because of the transmission loss. OTDR can be used to locate discontinuities in the fiber (small bubbles, breakage, etc) or tight bending of the fiber. However, OTDR relying on the single pulse measurement has relatively low signal to noise ratio (SNR). The system needs to perform hundreds of averages to achieve reliable sensing performance. The spatial resolution of OTDR is inversely proportional to the pulse width. For high spatial resolution measurements, short pulse and high bandwidth detectors have to be used, which further limits the sensitivity of the sensing [9].

Φ-OTDR is a technology that developed from OTDR with much improved sensitivity. It uses a coherent light source in a typical OTDR system. The optical interference of distributed Rayleigh scatterings within the duration of the light pulse is collected and processed. When an optical path difference (OPD) change due to perturbation (strain or temperature change) happens to a certain part of the fiber, the detector collected light intensity changes at the time corresponding to the location. The location of the perturbation can be resolved by compare the time traces captured before and after the OPD change. Since optical interference is sensitive to the OPD change, the strain sensitivity of Φ-OTDR can be as high as $4\ n\varepsilon$ [10,11]. However, Φ-OTDR has a difficulty to quantitatively link an interference signal to the specific parameters of interest because of the random nature of the Rayleigh scattering. Another advantage of Φ-OTDR is that it has

a strong dynamic measurement capability. The detection of a vibration frequency of 0.6 MHz was reported [12]. However, there is a tradeoff between the maximum distance and the maximum frequency for TDR-type technology. The measurement distance was limited to several hundreds of meters for such high frequency measurement [12].

Polarization OTDR (POTDR) is another high sensitivity distributed sensing technology that evolved from the conventional OTDR. It detects the local state of polarization (SOP) of Rayleigh backscattered light using a polarization analyzer along the optical fiber. The SOP is sensitive to temperature and strain change, as well as to the electric and magnetic field. However, the cross sensitivity of the polarization state changes makes it impossible to separate the various external disturbances through static measurement [13] [14].

Brillouin optical time domain analysis (BOTDA) and Raman optical time domain reflectometry (ROTDR) both fall in the time domain reflectometry (TDR) distributed sensing category. They both take the advantage of the nonlinear effect in optical fibers. In the BOTDA system, a pulsed pump and a continuous wave probe are counter propagating along a sensing fiber, where the pulsed pump generates Brillouin scattering during propagation. When the beat frequency between two waves is equal to the Brillouin frequency, the Brillouin scattering will be amplified. The frequency is determined by the refractive index of the fiber, so adjusting the frequency of the continuous wave can be used to determine the Brillouin gain spectrum (BGS) for any location. The difference between BGS is translated to the external measurement at any location along the fiber. The intensity and the frequency of the Brillouin scattering is sensitive to the geometry size and the

refractive index of the fiber, so BOTDA is suitable for distributed strain and temperature measurement. The strain sensitivity for BOTDA is generally around 10 με [10]. ROTDR measures the Raman stokes and anti-stokes lines, which is only sensitive to the temperature change with a sensitivity of about 1℃ [14].

The sensing range of TDR based technologies can reach tens of kilometers with meters of spatial resolution. The spatial resolution is limited by the width of the time domain pulse, which can be improved by decreasing the pulse width, but meanwhile the sensing range will be decreased. Optical frequency domain reflectometry (OFDR) has also been developed for distributed optical fiber sensing with a much improved spatial resolution of less than 1 mm [15,16]. OFDR uses a frequency-swept coherent light source and an interferometer structure (sensing arm and reference arm). The time-of-arrival information is obtained by the Fourier transform of the optical signal of the frequency sweeping range. OFDR has much higher SNR and spatial resolution compared with the conventional OTDR [17]. OFDR can resolve hundreds nε in strain [10]. However, it is limited by the size of the optical frequency sweep step, so the measurement range of conventional OFDR is short [18]. Some newly developed research results show that the measurement range of OFDR can be further increased to tens of kilometers with decreased spatial resolution [15,16]

A brief list of performance summary of optical fiber distributed sensing technologies is shown in Table 1.1. The detection method, longest sensing distance(D_{max}), highest spatial resolution(SR_h), sensitivity, and maximum measured vibration frequency (F_{vib}) are listed. For all the distributed sensing technologies, there is a trade-off between

the sensing range (D) and spatial resolution (SR), the ratio between them becomes a good indicator for a comprehensive evaluate the performance of the method, so the general D/SR for each method is also listed in the Table *1.1*. There are also some new researches that combined more than two types of sensing technologies together for the purposes of enhancing the dynamic measurement capability [19–21]. The reported measured vibration frequency was over megahertz, but most of them cannot support multi points sensing.

Table 1.1 Performance summery of the optical fiber distributed sensing technologies

Methods	D_{max}	SR_h	D/SR	Sensitivity	F_{vib} (Hz)
FBG [2]	100 channels	2 mm	100	10^{-5}	
Φ-OTDR [22]	1.25 km	5 m	250	$<10^{-7}$	39.5 k
P-OTDR [13]	1 km	10 m	100		5 k
BOTDA [23]	85 m	1.5 m	57	10^{-5}	98
OFDR [24]	30 m	20 cm	170	$<10^{-6}$	50

1.2 Motivations of this work

In the past few years, microwave-photonics technologies have been investigated for optical fiber sensing [25–28]. By introducing microwave modulation into the optical system, the optical detection is synchronized with the microwave modulation frequency. As a result, the system has a high SNR and thus an improved detection limit. In addition, the phase of the microwave-modulated light can be easily obtained and Fourier transformed to find the time-of-arrival information for distributed sensing. The microwave photonics

technology has been demonstrated for both quasi-distributed [9] and fully-distributed sensing [29,31,32].

Recently, an incoherent optical carrier based microwave interferometry (OCMI) technique has been demonstrated for fully distributed sensing with high spatial resolution and large measurement range [31]. The OCMI is insensitive to the types of optical waveguides, and the theoretically deduction as well as the preliminary results show that the modal interference have little influences on the OCMI signal. This work was initially motivated by the needs of distributed measurement in the harsh environment. Those applications addressed requirements on the mechanical and chemical properties of the sensor materials, so the first main objective of this work is to develop the OCMI based sensing systems that uses special multimode waveguides such as large core fused silica fiber and polymer fiber to perform distributed sensing to meet requirement of large strain and high temperature measurement in harsh environment. However, OCMI only read the interference in microwave domain. As we moved forward, we found that the sensing resolution of OCMI was low (in tens of με), which was limited by the intermedia frequency of the microwave source. Besides it was difficult to perform dynamic measurement for the vibration over 5 Hz. Those two limitations prevented us to fit OCMI in many applications, and improving the sensitivity and dynamic measurement capacity became the other two main objectives of this work. The specific research steps and objectives of this work includes:

1) Evaluating performance of OCMI for distributed sensing including the spatial resolution, dynamic measurement range, sensitivity and dynamic sensing

capability. Find the sensing limitation of OCMI though theoretical analysis and experimental demonstration.

2) Fitting various types of multimode optical waveguides into the OCMI system for the purposes of distributed sensing. Developing the in fiber weak reflectors fabrication methods.
3) Developing and demonstrating new technique for distributed sensing based on the microwave photonics system by using coherent light (CMPI) to achieve much improved sensitivity.
4) Exploring signal processing method for high speed dynamic measurement on the newly developed sensing platforms. Measuring the distributed continuous and pulse vibrations.

1.3 Organization of the dissertation

In this dissertation, the focus will be on developing distributed sensing systems based on the incoherent and coherent microwave photonics links. We will conduct the mathematical modeling and experimental studies to explore the performance and limitation of those systems.

The dissertation is organized as follows. Chapter 1 summarized the state of art of the optical fiber distributed sensing technologies. The motivation, background, and objective of this work was discussed as well.

Chapter 2 will introduce the optical carrier based microwave interferometer (OCMI) technology, which uses an incoherent light source as optical carrier, and constructs the

interference in the microwave domain. The mathematical model, system setup, signal processing method and the performance of the OCMI will be studied.

Followed by Chapter 2, Chapter 3 will explore the distributed sensing applications by using OCMI. Sensors fabricated by large core fused silica fiber, grade index multimode silica fiber, and multimode polymer fiber will be fitted into the system for the purpose of strain, crack, and temperature sensing.

Chapter 4 will discuss the coherent microwave photonics interferometers (CMPI) system for distributed optical fiber sensing. The system uses a coherent light source to obtain the optical interference signal from the cascaded weak reflectors for much improved sensitivity. In addition, the coherence length of the light source is carefully chosen or controlled to gate the signal so that distributed sensing can be achieved. The mathematical model as well as the experimental results will be presented.

Chapter 5 will demonstrate distributed dynamic measurement method by using CMPI. The measurement adopts a novel signal processing method, where the time varying information is recorded in the microwave frequency domain, and the varying frequency can be read in the time domain after the complex Fourier transform. With this method, the vibration frequency of up to tens of kHz can be measured. The experiment results for the multi-points continuous vibration as well as pulse vibration will be presented.

Chapter 6 will discuss the noise contribution of each component in both the OCMI and CMPI system. The effects of optical carrier spectrum will be analysed. The detection limitation will be shown by compare with the received Rayleigh scattering.

Chapter 7 will summarize the dissertation works and outline the research works to be continued in the future.

CHAPTER TWO

INCOHERENT OPTICAL CARRIER BASED MICROWAVE INTERFEROMETER (OCMI)

Incoherent optical carrier based microwave interferometry (OCMI) technique has fully distributed sensing capability with high spatial resolution and large measurement range [33]. The system used a microwave modulated incoherent (broadband) light source to interrogate cascaded intrinsic Fabry-Perot interferometers formed by adjacent weak reflectors inside an optical fiber. When the distance between two adjacent reflectors was larger than the coherence length of the light source, the optical interference components in the received signal became zero and the microwave terms were processed to form a microwave interferogram, which was further analyzed to calculate the optical path difference between any two reflectors along the fiber. The method has a number of unique advantages including high signal quality, relieved requirement on fabrication, low dependence on the types of optical waveguides, insensitive to the variations of polarization, high spatial resolution, and fully distributed sensing capability.

2.1 Mathematical model

The microwave photonics interferometer system is schematically shown in Fig. 2.1. A continuous wave laser with optical bandwidth of $\Delta\omega$ is used as the light source with its electrical field given by

$$E_0(\omega,t) = A_0(\omega)\cos(\omega t), \tag{2.1}$$

where ω is the optical frequency, t is the time variable, and A_0 is the amplitude of the light. Let's also assume that the optical power is uniformly distributed within the band $\Delta\omega$. The light intensity is modulated by the microwave signal given by

$$V_0(\Omega, t) = V_0(\Omega)\cos(\Omega t), \tag{2.2}$$

where $V_0(\Omega)$ is the amplitude of the microwave signal and Ω is the microwave frequency. The intensity modulated lightwave is launched into a single mode fiber (SMF) and the electric field of the lightwave becomes

$$E_{in}(\Omega, \omega, t) = \sqrt{1 + M\cos[\Omega t + \Phi_0(\Omega)]} \cdot A_0(\omega)\cos[\omega t + \phi_0(\omega)] \ , \tag{2.3}$$

where $\phi_0(\omega)$ and $\Phi_0(\Omega)$ are the initial phases of the optical carrier and the microwave at the launch port respectively, and $M = m \cdot V_0(\Omega)$ where m is the modulation coefficient of the electro-optic modulator (EOM) and M is much smaller than 1.

If there are N weak reflectors fabricated along the optical fiber, the electric field of the reflected lightwave from the ith reflector can be expressed as

$$E_i(\Omega, \omega, t) = \sqrt{1 + M\cos[\Omega t + \Phi_i(\Omega)]} \cdot A_{z_i}\cos\left[\omega t + \phi_i(\omega)\right] \tag{2.4}$$

where $A_{z_i} = A_0(\omega) \cdot \Gamma_i$ and Γ_i is the magnitude of the reflection coefficient of the ith reflector.

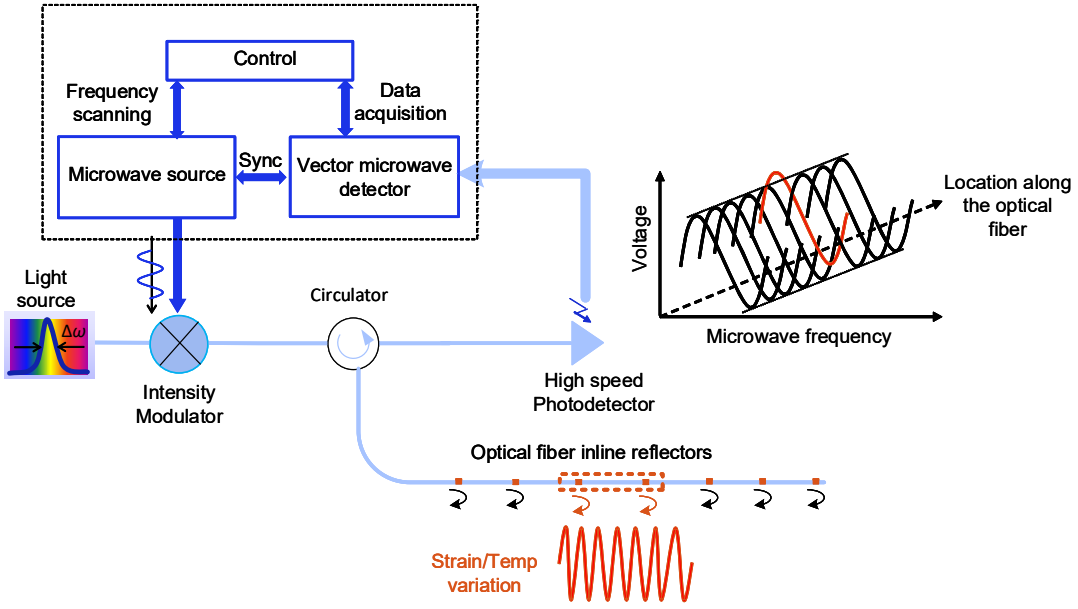

Fig. 2.1 Schematic illustration of microwave photonics sensors for distributed sensing

The optical phase and the microwave phase for the lightwave before the detector are $\phi_i(\omega) = \phi_0(\omega) - \frac{\omega z_i n}{c}$ and $\Phi_i(\Omega) = \Phi_0(\Omega) - \frac{\Omega z_i n}{c}$ respectively, where c is the speed of light in vacuum, n is the refractive index of the fiber, z_i is the distance that the light travels from the electro-optic modulator (EOM) to the ith reflector and then back to the photodetector. The total reflected signal power received by the photodetector is given by

$$I(\Omega, t) = \left| \frac{1}{\Delta\omega} \int_{\Delta\omega} \sum_{i=1}^{N} E_i d\omega \right|^2 \tag{2.5}$$

The beat among different optical frequency components creates low level noise [34], which is neglected in this work, so Eq.(2.5) can be expressed as

$$I(\Omega,t)=\frac{1}{\Delta\omega}\int_{\Delta\omega}\left|\sum_{i=1}^{N}E_i\right|^2 d\omega = I_{self}(\Omega,t)+I_{cross}(\Omega,t), \tag{2.6}$$

where $I_{self}(\Omega, t)$ and $I_{cross}(\Omega, t)$ are the self and cross products terms, respectively. Because the optical frequency is much higher than that of the photodetector, the photodetector output is the time-averaged signal over the optical period, given by

$$\left\langle I_{self}(\Omega,t)\right\rangle=\left\langle\frac{1}{\Delta\omega}\int_{\Delta\omega}\sum_{i=1}^{N}E_i^{\,2}d\omega\right\rangle=\frac{1}{2}\sum_{i=1}^{N}A_{z_i}{}^2+\frac{1}{2}\sum_{i=1}^{N}\left\{A_{z_i}{}^2M\cos\left(\Omega t-\frac{\Omega n z_i}{c}\right)\right\} \tag{2.7}$$

$$\begin{aligned}\left\langle I_{cross}(\Omega,t)\right\rangle&=\left\langle\frac{1}{\Delta\omega}\int_{\Delta\omega}(\sum_{i=1}^{N}\sum_{j\neq i}^{N}E_iE_j)d\omega\right\rangle\\&=\sum_{i=1}^{N}\sum_{j\neq i}^{N}\left\{\frac{A_{z_i}A_{z_j}}{2\Delta\omega}\int_{\Delta\omega}\cos(\phi_i-\phi_j)d\omega\sqrt{\left[1+M\cos\left(\Omega t-\frac{\Omega n z_i}{2c}\right)\right]\left[1+M\cos\left(\Omega t-\frac{\Omega n z_j}{2c}\right)\right]}\right\}\end{aligned} \tag{2.8}$$

When $\Delta\omega$ is large, the cross-product term $\left\langle I_{cross}(\Omega,t)\right\rangle$ is practically zero, as the integration $\int_{\Delta\omega}\cos(\phi_i-\phi_j)d\omega$ over the optical bandwidth in Eq. (2.8) is much smaller than $\Delta\omega$. In this circumstance, the cross-product term $\left\langle I_{cross}(\Omega,t)\right\rangle$ can be ignored. In OCMI system, an incoherent light source with wide bandwidth is used. As such, the cross-product term becomes zero.

The microwave photonics system synchronizes the detection and only measures the amplitude and phase of the signal at the microwave frequency Ω. The other frequency components (e.g., the DC term and the 2Ω terms) are excluded in the vector microwave detection. Thus, the complex frequency response S_{21} of the system, i.e., complex reflectivity normalized with respect to the input signal, is

$$S_{21,\mathrm{OCMI}}(\Omega)=\frac{1}{4}\sum_{i=1}^{N} mA_{z_i}{}^{2} e^{-\mathrm{j}\frac{\Omega n z_i}{c}} \tag{2.9}$$

By applying complex Fourier transform to $S_{21,\mathrm{OCMI}}(\Omega)$, we obtain the time resolved discrete reflections

$$F_{\mathrm{OCM}I}(t_z)=\frac{1}{4}\sum_{i=1}^{N} mA_{z_i}{}^{2}\delta(t_z-\frac{nz_i}{c}) \tag{2.10}$$

The amplitude of the *i*-th pulse is proportional to A_{z_i}, and the time gate function $g(t)$ can be applied to select any two time domain pulses. The time domain signal after applying a time gate function is thus given by $F_{\mathrm{OCMI}}(t_z)\cdot g\left(t\right)$. Fourier transforming the time-gated signal back to the frequency domain and reconstructing the microwave interferogram which can be used to find the optical distance between the two gated reflectors. The reconstructed OCMI-FPI interferogram is thus given by

$$S_{21\mathrm{Re}con}(\Omega)=S_{21,\mathrm{OCM}I}(\Omega)*\left[G(\Omega)\exp(-i\Omega\tau_0)\right] \tag{2.11}$$

where $G(\Omega)$ is the inverse Fourier transform of the gate function $g(t)$; τ_0 is the time delay of the gate function. Assume the sidelobe of the transformed gate function decays fast and the two gated reflector has the same reflectivity A, the Eq.(2.11) can be approximately expressed as

$$S_{21\mathrm{Recon}}\approx\frac{1}{2}A^2 m\cos\left[\Omega\frac{nz_i-nz_j}{c}\right]=\frac{1}{2}A^2 m\cos\left[\Omega\frac{OPD_{ij}}{c}\right], \tag{2.12}$$

where $OPD_{ij}=n\cdot\left|z_i-z_j\right|$. The OPD between the two gated reflectors can be found out by reading the free spectral range (FSR) on the reconstructed microwave interferogram,

$$FSR_{ij} = \frac{c}{OPD_{ij}}, \tag{2.13}$$

The OPD change (ΔOPD) between two reflectors could show as the interference fringe shift, and could be easily read out from the reconstructed spectrum as

$$\Delta\Omega / \Omega = -\Delta OPD / OPD. \tag{2.14}$$

It is worth to point that, n is the effective index of the optical wave guide between the two gated reflectors. The value of it is the average results based on all the exited modes in that waveguide. Any perturbation along the fiber changes the modes distribution inside the fiber, however, the average value of the refractive index wouldn't experience obviously change, so the OCMI has low dependence on the types of optical waveguides and also insensitive to the variations of polarization. More rigors equation deduction and simulation results for the distributed sensing using OCMI can be found in Ref [31].

2.2 System configuration and signal processing

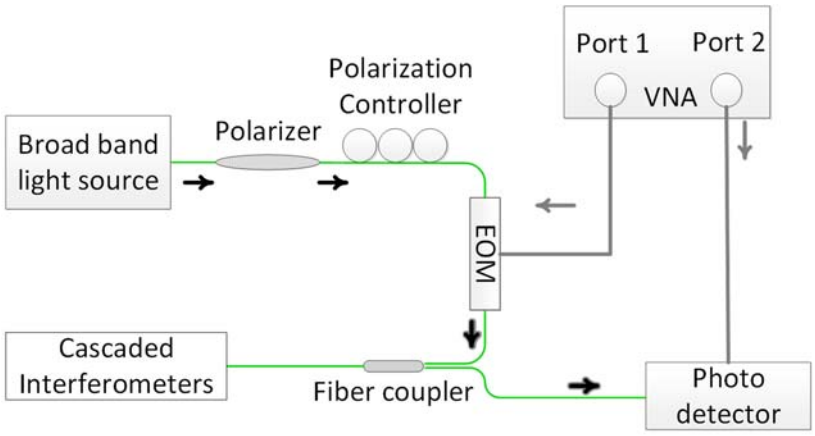

Fig. 2.2 Schematic of the OCMI system setup

The schematic configuration of the OCMI based optical fiber strain sensor is shown in Fig. 2.2.

First, the light from the broadband source (BBS) is intensity modulated by a microwave signal through an electro-optic modulator (EOM). An in-line fiber polarizer and a polarization controller followed by the light source are used to optimize the modulation depth of the EOM, which is driven by port 1 of the vector network analyzer (VNA). The microwave-modulated light, of which the optics is the carrier and the microwave is the envelope, emits from the EOM, and then couples into a 2×1 fiber coupler (a circulator also works). The fiber with cascaded interferometers is spliced to one lead of the fiber coupler. The interferometers could be F-P type, and also could be the Michelson type. Applications of adopting those two types of interferometers into the OCMI system is presented in the chapter three. The reflected light from the two arms of the interferometer is then detected by a high-speed photo-detector, which converts the optical signal into electrical signal. The electrical signal is then recorded by port 2 of the VNA. The VNA is referred to as voltage ratio measurements where a swept continuous wave (CW) source in microwave band is tracked by a transmission receiver and the results are displayed as scattering parameters S_{21}.

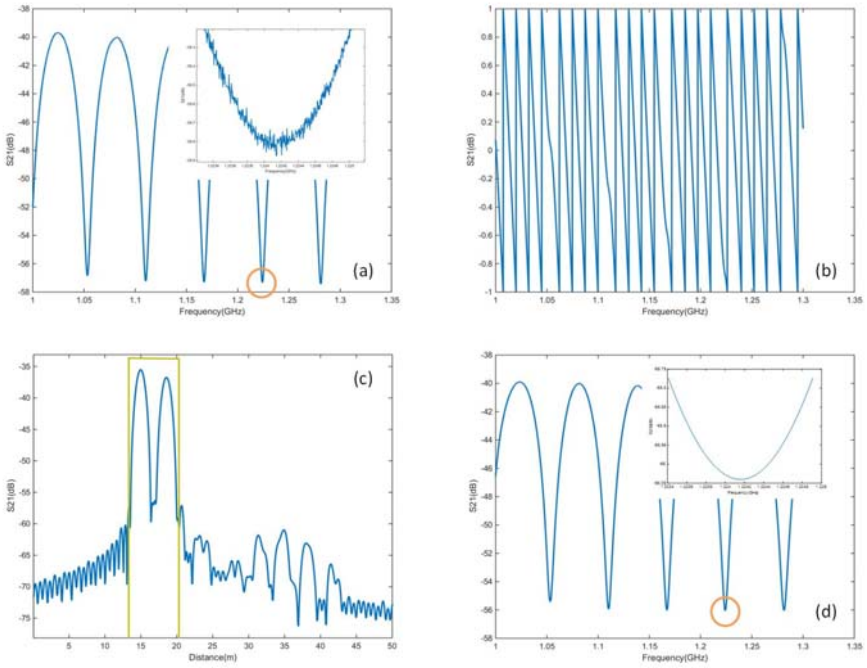

Fig. 2.3 (a) Amplitude spectrum of the original S_{21}; (b) phase spectrum of the original S_{21};(c) time domain signal got from S_{21} through the IDFT; the rectangular gate indicates the time domain band pass filter; (d) amplitude spectrum of the filtered S_{21}.

The amplitude and phase spectra of the scattering parameter (S_{21} in this illustration) obtained from a Michelson-OCMI based two reflection optical fiber sensing system are shown in Fig. 2.3(a) and (b) respectively. The time domain response of the system can be obtained by applying an inverse discrete Fourier transform (IDFT) to the complex S_{21}. Fig. 2.3 (c) shows the amplitude spectrum of the calculated time domain response where the two main pulses indicate the reflections from the fiber ends of the two sensor arms, respectively. The other pulses shown in the time domain amplitude spectrum could be caused by multiple reflections at the fiber ends. Those small pulses in time domain

contribute to the ripples on the amplitude spectrum shown in the inset of Fig. 2.3 (a). One way to eliminate the ripples is to add a time domain gate on the TDR signal to select the two main reflections and suppress other unwanted signals, as shown in Fig. 2.3 (c), and then apply a discrete Fourier transform (DFT) to the filtered signal to reconstruct its frequency spectrum. The amplitude spectrum of the reconstructed signal is shown in Fig. 2.3 (d) where the inset shows the zoomed in spectrum. A distance change between the two pulses, would show as the readable shift of the reconstructed spectrum.

2.3 Performance characterization

2.3.1 Window effect and spatial resolution

In reality, the sweeping microwave frequency has a limited bandwidth of Ω_b at the center frequency of Ω_c. To consider the limited bandwidth the time domain signal expressed in Eq. (2.10) should be modified to be

$$F'(t_z)_{OCMI} = \left[\Omega_b \operatorname{sinc}(\Omega_b t_z)\, \mathrm{e}^{-j\Omega_c t_z} \right] * F_{OCMI}(t_z) \tag{2.15}$$
$$= \frac{1}{4}\sum_{i=1}^{N} \Omega_b \operatorname{sinc}\left[\Omega_b (t_z - \frac{nz_i}{c}) \right] \mathrm{e}^{-j[\Omega_c (t_z - \frac{nz_i}{c})]} m{A_{z_i}}^2 \delta(t_z - \frac{nz_i}{c}).$$

If the reflectors are far away from each other, the side lopes of the sinc functions can be ignored. The signal at the distance z_i can be approximated to be

$$F'_i(t_z)_{OCMI} \approx \frac{1}{4}\Omega_b \operatorname{sinc}\left[\Omega_b (t_z - \frac{nz_i}{c}) \right] \mathrm{e}^{-j\Omega_c (t_z - \frac{nz_i}{c})}\, m{A_{z_i}}^2 \tag{2.16}$$

The limited frequency band actually works as a center shifted frequency domain window, and any window function can be used to before the Fourier transform to achieve different signal quality. Eq. (2.15) shows the transform results of using the rectangular window function. However, the windowing function tends to reduce the sharpness of the

response, spreading time pulses, and stretching out slopes, thereby reducing the resolution of the transform and distorting the transitions of the frequency response. There is a trade-off between sidelobe height and resolution when determining the window function [35].

The spatial resolution is defined as the ability to resolve two closely-spaced response. Spatial resolution depends upon the time domain mode, the frequency range, whether it is a reflection or transmission measurement, and the relative propagation velocity of the signal path [35]. For an OCMI system, the spatial resolution is inversely proportional to the measurement frequency span Ω_B and is also a function of the window that is selected. VNA commonly uses Kaiser-Bessel window function [35,36]

$$w(n) = \frac{I_0\left(\beta\sqrt{1-\left(\frac{n-N/2}{N/2}\right)}\right)}{I_0(\beta)}, \quad 0 \le n \le N \tag{2.17}$$

where I_0 is the zeroth-order modified Bessel function of the first kind. The length $L = N + 1$. The value of β controls the sidelobe attenuation of α dB after transform

$$\beta = \begin{cases} 0.1102(\alpha - 8.7), & \alpha > 50 \\ 0.5842(\alpha - 21)^{0.4} + 0.07886(\alpha - 21), & 50 \ge \alpha \ge 21 \\ 0 & \alpha < 21 \end{cases} \tag{2.18}$$

Increasing β widens the main lobe and decreases the amplitude of the sidelobes.

Table 2.1 Approximately relationship between window selection, spatial resolution and sidelobe level [35,37]

Window	Spatial resolution	Sidelobe level (dB)

Minimun (β=0)	1.20/ $\Omega_b \cdot c/n$	-13
Normal (β=3)	1.95/ $\Omega_b \cdot c/n$	-44
Maximun (β=6)	2.77/ $\Omega_b \cdot c/n$	-75

Table 2.1 Approximately relationship between window selection, spatial resolution and sidelobe level Table 2.1shows the relationship between the frequency span and the window selection (Kaiser window with different β value) on response resolution for responses of equal amplitude. It is obviously that the spatial resolution reaches the highest when use the minimum the β value. For example, using 10 GHz wide frequency band normal window, we can get the spatial resolution of about 4 cm. If we use the minimum window, the minimum resolved distance becomes 2.9 cm.

The ability to locate a single response in time is called time domain range resolution, which measures how closely we can pinpoint the peak of the response when a single response is present. The range resolution equals to the time domain span T_{span} divided by the number of points N_0 that used for the transform as [38]

$$Resolution_{range} = T_{span} / N_0 - 1 \tag{2.19}$$

N_0 can be much larger than the frequency domain sampling point N through zero padding, so the range resolution is always much finer than the spatial resolution. The change of N_0 only increases or decreases the spacing between data points, and it does not affect the ability to resolve two closely spaced signal. The sensing resolution of the OCMI is decided by the time domain range resolution which is limited by the system noise.

2.3.2 Sensitivity

The sensitivity of the OCMI system is decided by the minimum measurable microwave spectrum shift. The signal power, sampling points(N), and the intermedia bandwidth (IFBW) of the VNA are the three important parameters that decide the sensitivity. For the small signal detection where the thermal noise is much more substantial than the shot noise, the signal power level is critical to the SNR of the system. Hence, the sensitivity of the system is decided by the signal power level. When we create reflectors on the fiber, we don't want the single reflector has too large reflectivity, because the number of reflectors that can be cascaded along the cable will be limited in that case. Also we cannot have infinity low reflectivity reflectors, since the lower the reflectivity is, the lower SNR would have for the single reflector, thus the lower sensitivity of the sensor we will have. The IFBW of the VNA, the sampling points in frequency domain, and signal power are the factors that decide the SNR, and thus also decides the sensitivity of the OCMI.

We did some fundamental experiment to find out the received power lever of the vector network analyzer (VNA) versus the sensitivity of the sensor. The experiment results helped us to do the preliminary power budget of system and optimize the system.

There is lots of equipment in this system, and each one can add noise into the system. The noise contribution from each component will be discussed in chapter 6, but in this chapter, we simplified the model. Our experiments started with using coaxial cable FPI (CCFPI) sensor [39], where the sensing data include the noise only caused by VNA and sensor itself. The two reflectors of the CCFPI have made by two metal rings. The distance between them was about 20 cm. The reflectivity of one reflector was about -29 dB. The

microwave bandwidth was set as from 100 MHz to 6 GHz, the bandwidth of the intermediate frequency (IFBW) was set as 1 kHz, the sampling points was set as 16001, and the time domain gate was set as 11ns-15ns. We tuned the output microwave power from -87 dBm to 5 dBm, the increasing step was 5 dB, and thus, the received power for the single reflector at the receiver is from -116 dBm to -24 dBm. The spectrum at each input power level for 10 times were recorded, the total 10 sweeps cost about 20 minutes. The shifting of the dip round 3.7 GHz on the amplitude spectrum was recorded. The average of the absolute variation value was plotted as the function of the received power as shown in Fig. 2.4 Average of the absolute comparative dip frequency shift versus different output single pulse power level. The insert shows the output S21 frequency spectrum of the sensor with input microwave power to the sensor of -87 dBm.

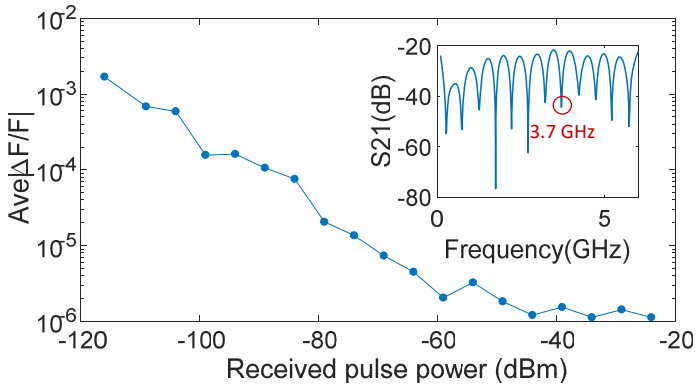

Fig. 2.4 Average of the absolute comparative dip frequency shift versus different output single pulse power level. The insert shows the output S21 frequency spectrum of the sensor with input microwave power to the sensor of -87 dBm.

As we can see from Fig. 2.4, the higher the pulse power was, the less dip variation experienced. When the received single pulse power was bigger than -64 dBm, the average absolute variation decreased to the level of 0.5×10^{-5}. The experiment results indicate that no matter how complicate the system is, if we want to measure the change of less than 10^{-5}, the electric power of the signal response that injected into the microwave receiver should be larger than -64 dBm.

When it comes to the OCMI, more electrical and optical components are added into the system, such as the EOM, and the optical receiver, and the optical amplifier. It is important to know how much noise are added into the system, and how those new added noises affect the sensing resolution. The same experiment which was exploited to investigate the sensing resolution versus the received electric power for CCFPI has been done for a pair of FPI by using the OCMI system. The setup is shown as 2.6 The output power was controlled by tuning the EDFA. Both the SMF and MMF (62.5/125 um, grade index) fabricated Michelson type interferometer have been fitted in to OCMI system separately. The distances between two arms in both scenario were about 20 cm. The reflectivity of one reflector is about -14 dB, but the optical coupler added 6 dB to the signal. The microwave bandwidth was set as from 100 MHz to 6 GHz, the IFBW was set as 1 kHz, the sampling points was set as 16001, and the time domain gate width was set as 4ns. The spectra shifting versus different received single pulse level have been recorded. The experiment results for the both SMF and MMF scenario are shown in Fig. 2.5. Once again, we didn't found any evidence showed that the multimode interference affected the stability of sensor for short range sensing. All the add-on optical, and electrical equipment didn't

show obvious influence on the stability of the sensor. As far as the received pulse power can be larger than -64 dBm, the absolute variation less than10^{-5} can still be achieved in both cases.

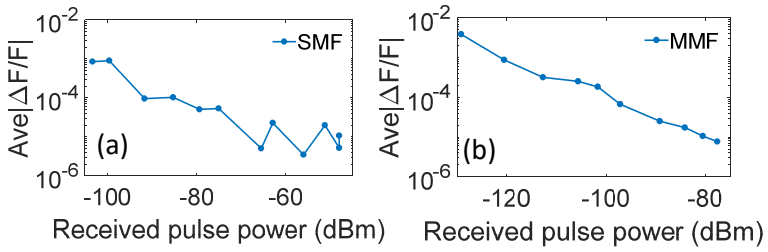

Fig. 2.5 Average of the absolute comparative dip frequency shift versus different output single pulse power level. (a) SMF sensor; (b)MMF sensor

The sensitivity of the OCMI sensor also decided by the sampling points and the IFBW of the VNA. The sampling points increase by factor of m, as a results the SNR increase s by sqrt(m), and the noise level is proportional to the IFBW. It is obviously that with the same signal power the lower the noise level is the higher sensitivity can be achieved.

2.3.3 Dynamic measuring range and sensing range

OCMI sensing system measures the FSR change on the reconstructed spectrum formed by any two time plus. According to Eq. (2.13), the FSR is monotonically decreasing as increasing of OPD, so the measurement range is not confined by the signal processing. The minimum FSR that can be detected is corresponding to the maximum measurable OPD, which is limited by the IFBW as

$$\mathrm{OPD}_{\max}=1/(2\cdot IFBW)\cdot c. \tag{2.20}$$

For instance, with IFBW of 1 kHz the maximum OPD that can be read is 150 km. In reality, the dynamic measurement range is decided by the physical property of the fiber sensors material. One of the good thing about OCMI is that it allows us to fit varieties of optical waveguide made sensors into the system, which make the large strain and high temperature distributed sensing becomes possible.

The distributed sensing range is the maximum distance from the response to the microwave source that the system can see without aliasing. The range is also limited by the IFBW, but also decided by the sampling points N and the frequency band width f_B. For the reflection based sensors, the sensing range is calculated as

$$\text{sensing range}=N / f_B / 2 \cdot c / n. \tag{2.21}$$

If we have 16001 sampling points within 1 GHz bandwidth, and the optical fiber has refractive of 1.45, the maximum sensing distance is 1655m. The sensing range can be increased by decrease the frequency sampling interval: decreasing the frequency bandwidth or increasing the number of sampling points within the giving band both can help, but there is a trade-off among the spatial resolution, sensing range, and measurement time.

2.3.4 Dynamic sensing capability

OCMI relies on the frequency measurement, and the dynamic measurement capability depends on the measurement time for the VNA to accomplish a single measurement plus the waiting time between two measurements. The measurement time for single measurement is determined by the sampling points and IFBW. When set the data points to 51, and set the IFBW of 10 kHz, the measurement time is 0.006 s. The waiting

time equals to the measure time. In this case the highest frequency we can measure by using this system is less than 35 Hz. However, with such setup, the SNR is low, to get the decent sensing information, the signal from the sensor should be strong, and also the OPD change of the sensor interferometer should be large.

A cantilever beam experiment was done to demonstrate the dynamic measurement by using the OCMI system. A SMF based Michelson interferometer was made by using the 2×2 SMF 3dB coupler. The length difference between the two arms was about 0.33 m. Part of the longer arm was fixed on a metal rod with length of 48 inch (1.21m) and diameter of 1/4 inch(6.35 cm), as shown in Fig. 2.6(a). The density of steel was used as 7.8 g/cm^3 for calculation, so the natural frequency of the rod was 4.081 Hz (the period is 0.2450 s).

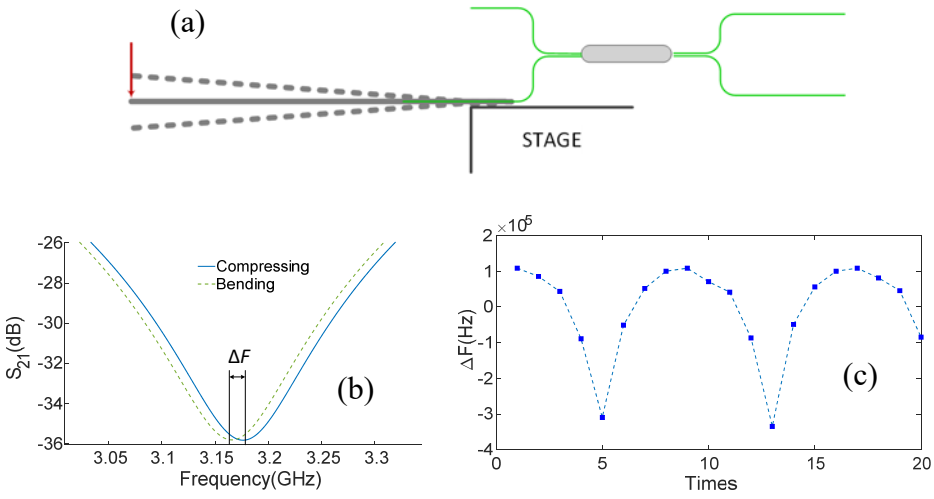

Fig. 2.6 (a) Set up of the cantilever beam. (b) the interferogram generated by the Michelson interferometer in the compressing and bending condition (c) Shifting trend of the interferogram when periodically bending the cantilever beam back and force.

The number of data points and IFBW of VNA were set to be 51 and 10 kHz, respectively. Firstly, the cantilever beam was periodically bent back and force, and the dip of the spectrum fringe in microwave domain showed periodically shifting and followed the trend as shown in Fig. 2.6 (c). Since the sensor is fixed on the top of the steel rod, bending up and down has a different effect on the sensor, thus the dip frequency shifting (ΔF) did not change sinusoidally as function of time. Let VNA do the continuous sweeping while the cantilever beam is doing free vibration. The sweeping period was set to 0.1s. Fig. 2.7(b) shows the FFT result of the Fig. 2.7(a), and the vibration frequency of 3.2 Hz is what we expected.

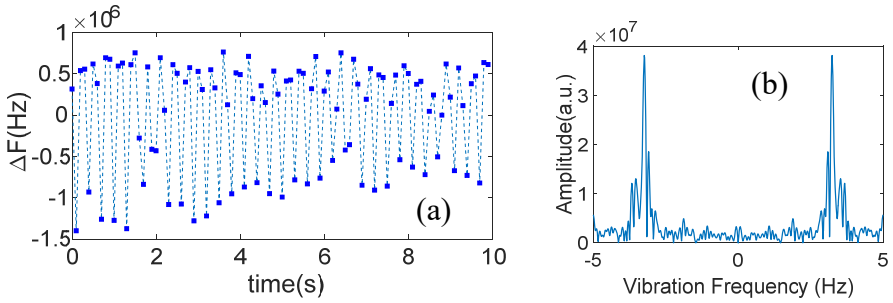

Fig. 2.7(a) Dip shifting of spectrum of the dynamic measurement. (b) FFT results of the measurement.

CHAPTER THREE

SENSING APPLICATIONS BY USING OCMI

The essence of OCMI is to read optical interferometers using microwave. As such, it combines the advantages from both optics and microwave. When used for sensing, it inherits the advantages of optical interferometry such as small size, light weight, low signal loss, remote operation and immunity to EMI, high sensitivity. Meanwhile, by constructing the interference in microwave domain, the OCMI has many unique advantages that are unachievable by conventional optical interferometry, including insensitivity to the types of optical waveguides and distributed sensing with spatial continuity. In this chapter, sensors fabricated by large core fused silica fiber, grade index multimode silica fiber, and multimode polymer fiber are fitted into the OCMI system for different purpose of sensing.

3.1 Microwave interrogated multimode large core fused silica fiber Michelson interferometer for strain sensing

Most optical fiber strain sensors are implemented based on single mode fibers (SMFs), because they form an approximately periodical spectrum fringe pattern, where the period has direct correlation with the optical path difference (OPD) generated by the sensor. A slight OPD change results in the period change of the spectrum fringe, and the change value can be read by measuring the shift in spectra. On the other hand, the process of interpreting a sensing data from the signal generated by a multimode fiber (MMF) sensor is more complicated, and is sometimes unachievable. Since different modes have different

effective refractive indices, and result in different OPDs, the interference among the modes contributes to the pattern of the spectrum fringe. The inter-modes interference can be varied by environmental perturbation and fiber operation condition variations in practice. The relationship between the period of the spectrum fringe and the OPDs becomes uncertain. Thus, the inter-modes interference dependence in MMF sensors could cause measurement errors [40].

Sensors based on MMF are desired in some circumstances, since MMF has some attractive features compared to SMF, such as a flexible core diameter and wide choices of optical material. By choosing the proper core size and fabrication material, the fiber sensor could be robust and insensitive to irrelevant environmental parameter changes. For example, the core of the most widely used SMFs is made from Germanium-doped silica. The Germanium dopants will diffuse with time leading to degradation of the signal. The diffusion rate increases with temperature, and it increases dramatically as the temperature increases beyond 650 °C [41]. Experimental results showed that, for SMF based FBG sensor, 0.01 nm drifting of the Bragg wavelength has been found within 100 hours when the ambient temperature is 800°C [9]. To solve the long-term stability issue under high temperature for fiber optic sensors, pure fused silica core fiber (FSCF) is a good platform because it is free of dopants. However, most of the commercial FSCF has the comparatively large core diameter, which results in a large number of modes propagating inside the core. This reduce the quality of the signal when FSCF is used as a sensing devise.

During the past few years, investigations have been done to find a suitable way to design a MMF based strain sensor. Some structures fabricated using MMF have been

reported. Repeating the sensing structures that have already been developed on the SMF is one approach. By adopting this, FBG sensors in MMF were created using the UV light side writing technique [42]. Later on, the inter-modes interference effect in MMF sensor systems was theoretically analyzed, where a MMF extrinsic Fabry-Perot interferometric (EFPI) sensor has been investigated [43]. Another approach is to use a single mode-multimode-single mode (SMS) fiber structure [44–46]. This approach is based on multimode interference (MMI) and the corresponding self-imaging phenomena. Sensors designed based on this technique have the advantages of high sensitivity, low cost, and ease of fabrication. However, MMI is sensitive to MPD meaning that bending slightly on the fiber would dramatically change the modal distribution along the MMF and thus influence the sensing signal. As a result, packaging for such sensors is a challenge [47].

During the past few years, microwave photonics technology has been applied for sensing applications to combine advantages from both optics and microwave. For example, by using the single microwave frequency modulation, the wavelength shift of the FBG can be converted into amplitude variation of the modulated microwave signal with fast response. The sensors interrogated in this way are suitable for the dynamic measurement [48]. Inspired by the operation principle of a discrete time microwave photonics filter, interrogating the FBG signal through swept frequency microwave modulation system has been demonstrated, and a distributed temperature sensing scheme with high spatial resolution has been realized [29,49]. Intrigued by the microwave photonics technology, we proposed using a low coherence optical carrier based microwave interferometry (OCMI) for sensing applications. The OCMI offers many unique features

including spatially uninterrupted distributed sensing, high signal quality, low dependence on multimodal influence, etc [26,31,50].

In this section, a Michelson type-OCMI is demonstrated for strain sensing in high temperature [27]. The sensor is made with two pieces of FSCF with core diameter of 200 μm and total diameter of 220 μm. Due to the relatively large size, the sensor is easy to fabricate, and quite robust. Since the fiber core material is dopant-free, the strain sensor would not suffer from the migration of dopants and thus could have promising performance in the high temperature environment. Besides, the pure fused silica has lower thermal-optic coefficient in comparison with the traditional doped silica, so the temperature-strain crosstalk can be further reduced by using such dopant-free material for strain sensing.

3.1.1 Principle of operation

The schematic configuration of the proposed Michelson-OCMI based optical fiber strain sensor is shown in Fig. 3.1. First, the light from the broadband source (ASE, 1530 – 1560 nm) with an output power of 13 dBm is intensity modulated by a microwave signal through an electro-optic modulator (EOM, Pirelli Opto-Electric Components Team, Italy). An in-line fiber polarizer (Thorlabs, US) and a polarization controller (Thorlabs, US) followed by the light source are used to optimize the modulation depth of the EOM. The EOM is driven by the port 1 of a vector network analyzer (VNA Agilent E8364B) and has an insertion loss of around 6 dB. A bias DC source (3.6 V) is used for obtaining a highest modulation index. The microwave-modulated light of which the optics is the carrier and the microwave is the envelope emits from the EOM, and then couples into a 3-dB 2X2 multimode fiber coupler. The lead-in and out fiber pigtails of the coupler are made by grade

index MMF with inner/outer diameter of 62.5/125 µm. Two pieces of 200/220 µm FSCF with different lengths are used as two arms of the Michelson interferometer. They were spliced to the two leads of the fiber coupler, respectively. The end faces of the two FSCFs are vertically cleaved to form two partial reflectors. The reflected light from the two arms of the interferometer is then detected by a high-speed photo-detector (OE-2 Wavecrest corporation), which converts the optical signal into electrical signal. The electrical signal is then recorded by port 2 of the VNA. The VNA is referred to as voltage ratio measurements where a swept continuous wave (CW) source in microwave band is tracked by a transmission receiver and the results are displayed as scattering parameters (S_{21}) [35]. The OPD of the two arms can be calculated through the recorded S_{21} amplitude and phase spectrum.

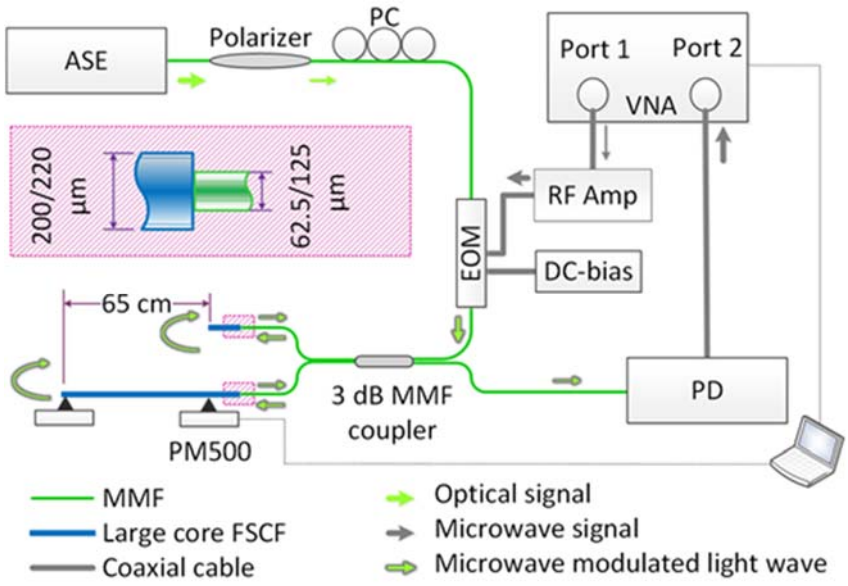

Fig. 3.1 Schematic of a Michelson- based optical fiber strain sensing system. VNA: Vector network analyzer. ASE: Amplified spontaneous emission light source (1530 –

1560 nm). PC: Polarization controller. EOM: electro-optic modulator. RF Amp: Microwave amplifier. PD: Photodetector. PM500: Programmable stage. Inset: Schematic of the splicing point between MMF and FSCF.

In this proposed Michelson-OCMI strain sensor, the shorter piece of the FSCF was used as a reference arm; the longer piece was used as a sensing arm. The smallest length difference between two arms ($L_{\min}$) is limited either by the coherent length of the light source which can be estimated as $\lambda^2/\Delta\lambda$ (λ is the center wavelength of the light source, $\Delta\lambda$ is the bandwidth of the light source) or by the spatial resolution of the system (L_{SPR}) which is decided by the microwave bandwidth (f_B) as

$$L_{\min} = \frac{c}{f_B n_{co}}. \tag{3.1}$$

In general, f_B is in the scale of GHz, so the minimal length difference is several centimeters according to Eq.(3.1). The coherence length of the optical signal is about 75 μm given the bandwidth of 30 nm. As a result, the length difference is much larger than the coherence length of the optical signal.

The largest length difference between two arms (L_{max}) should be smaller than the coherent length of the microwave source, which is limited by the intermedia frequency band width (IFBW), following the relationship $L_{max} < c$ / IFBW. Assume that IFBW equals to 1kHz, the L_{max} is in scale of 10^5 meter which is sufficiently long to let the microwave signals superimpose coherently.

In principle, a strain (ε) applied to a FSCF will induce a change in its physical length (ΔL) and refractive index of the core (Δn_{co}). The expression of length and refractive index changes caused by a strain can be written as [51]

$$\Delta L = L\varepsilon, \Delta n_{co} = -n_{co} P_{eff} \varepsilon, \tag{3.2}$$

where P_{eff} is the effective strain-optic coefficient, n_{co} is the effective refraction index of the core, L is the length difference between the two arms. As such, the change in OPD (ΔOPD) of the interferometer can be expressed by

$$\Delta OPD = 2L(-\frac{\Delta n_{co}}{n_{co}} + \frac{\Delta L}{L}) = 2L(-P_{eff} + 1)\varepsilon, \tag{3.3}$$

Consequently, the strain induced microwave frequency shift Δf can be expressed as

$$\Delta f = (-P_{eff} + 1)\varepsilon f, \tag{3.4}$$

where f denotes the interrogation frequency. P_{eff} is approximately 0.204 for fused silica material [52]. From Eq.(3.4), the strain sensitivity is dependent on the interrogation frequency and the effective strain-optic coefficient. The larger the interrogation frequency is, the higher the strain sensitivity will be. A rough calculation based on Eq.(3.4) reveals that an anticipated slope of strain response at the interrogation frequency of 3 GHz is -2.388 kHz/με.

The temperature change (ΔT) caused frequency-shifting Δf_T can be expressed as [45]

$$\Delta f_T = -\frac{L_T}{L_t}(a_{CTE} + \frac{dn}{dT}) f \Delta T \ , \tag{3.5}$$

where a_{CTE} and dn/dT are the CTE and the thermal-optic coefficient of the material, respectively. L_t is the total length difference of the two arms; L_T is the length of the part of the sensing arm which has been put into the furnace. For fused silica, the CTE is 0.55×10^{-6} /°C and the thermo-optic coefficient is approximately 7×10^{-6} /°C, which is smaller than that of the conventional Germanium doped silica optical fiber 9×10^{-6} /°C [53]. This will reduce the influence of the temperature effect. In addition, the FSCF does not have the dopant diffusion problem in high temperatures.

Based on Eqs.(3.4) and (3.5), the temperature-strain cross-talk of the OCMI sensor is given by

$$\frac{\mu\varepsilon}{\Delta T} = \frac{L_t}{L_T} \cdot \frac{\Delta f_T / \Delta T}{\Delta f / \mu\varepsilon} = \frac{(a_{CTE} + \frac{dn}{dT}) \cdot 10^6}{-P_{eff} + 1} \ , \tag{3.6}$$

The calculated result of the temperature strain cross-talk for the FSCF based sensor is 9.48 με/°C. The theoretical value shows that the FSCF based strain sensor has a relatively small temperature strain crosstalk.

3.1.2 Experimental results and discussion

Experiments were carried out to demonstrate the strain sensing capability of the large core FSCF based Michelson-OCMI. In these experiments, the VNA was configured to record the S_{21} signal with 16001 equally sampled data points. The intermediate frequency bandwidth (IFBW) was set to be 500 Hz. The sensitivity of the sensor is

proportional to the interrogation microwave frequency. To achieve a higher sensitivity, the frequency sweeping range was from 3 to 3.5 GHz. The entire measurement time including microwave frequency swept and signal processing is about 2 s and is determined by the IFBW and number of data point. As shown in Fig. 3.1, one end of the longer piece of FSCF was fixed to a motorized stage (PM500, Newport), the other end was fixed to a 3D adjustable stage. Fixing of the fiber was realized by applying the all-purpose glue (Loctite® Super Glue Ultra Liquid Control®). According to Eq.(3.1), L_{min} is about 40 cm. For easier assembling, the length difference of the two arms was fabricated as 65 cm, which is slightly larger than the length of furnace that was used for the temperature-strain crosstalk testing. The distance between the two fixing points was set as the same as the length difference of the two pieces of FSCF. The S_{21} spectra were constantly captured by the VNA as strain increased step by step. Time domain response was obtained by applying an IDFT to the S_{21}. A width of 14-ns time domain gating function was applied to improve the signal quality. Because of the mode mismatch between the FSCF and the lead-in multimode fiber, the reflected light will experience a loss at the splice point. We have found a loss of about 12 dB when evaluating the power budget of the system. Fig. 3.2 shows the recorded interferogram in the microwave domain after filtering. It is quite clear that the interference pattern was clean and has a fringe visibility of up to 40 dB, indicating that the MMI showed little influence to the OCMI interferogram. In a sense, the proposed OCMI technique has low dependence on the multimodal influences.

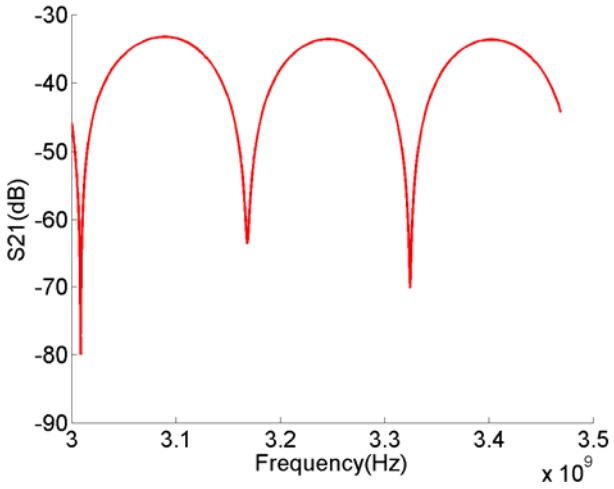

Fig. 3.2 Filtered S_{21} amplitude spectrum recorded without applying any strain to the sensing arm.

Three different strain increasing steps of 100 με, 20 με, and 10 με have been applied to the sensor, respectively. The experiments with 100-με and 20-με steps were used to demonstrate the linear frequency shifting response of the sensor to the applied strain. The experiment with 10-με step scale was used to identify the resolution of the sensor. 10 steps were executed for each step scale, and the three sets of experiment shared the same starting points.

The spectrum shifts as the tensile strain increased with a step of 100 με, which is 65 μm corresponding to for the total length of 65 cm. The third dip in the S_{21} amplitude spectra, with the initial frequency of 3.325 GHz was taken for interrogation Fig. 3.3 plots

the dip frequency shift as a function of the applied axial strain, where total 1000 με was applied with a step of 100 με. The total dip frequency change for the interrogation dip was -2.505 MHz in response to 1000 με, the slope of the strain versus dip frequency shift was -2.622 kHz/ με, around the dip frequency of 3.325 GHz, which is close to the

calculated value (-2.647 kHz/ με). Increasing the axial strain induced a redshift to the frequency spectrum as predicted by Eq.(3.4). To verify the capability of small strain sensing, the strain step was reduced to 20 με, and the frequency shift is shown in inset of Fig. 3.3. The sensor still shows linear spectrum shifting response to the applied strain, indicating that the sensor presented in this paper can be used for strain sensing after appropriate calibration. Linear fitting was applied to the spectrum shifting vs. strain data. The standard deviation (STD) of the linear regression was 9.075 kHz which corresponds to frequency shift caused by 4 με. The stain applying process was finished in less than 3 minutes, so, the minimum strain that can be detected should be larger than 4 με.

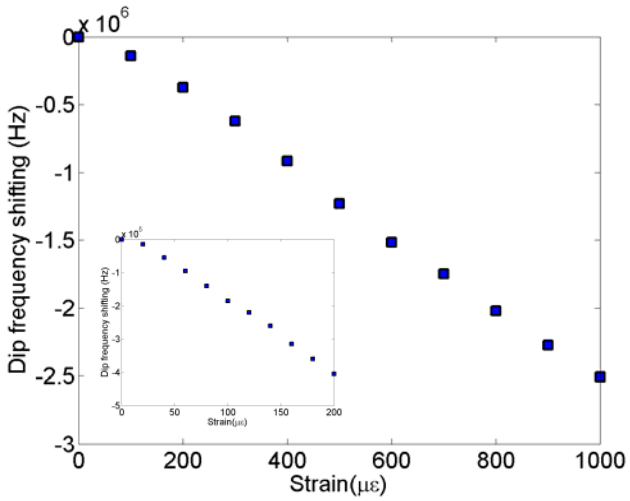

Fig. 3.3 Strain response of the large core FSCF based OCMI. The inset shows the zoom in frequency shifting vs. strain at the strain applied range from 0 – 200 με.

In order to explore the temperature strain crosstalk of the 200-μm diameter core FSCF based sensor, the center part of the longer piece FSCF was placed in a furnace, where the fiber length inside of the furnace is 40 cm.

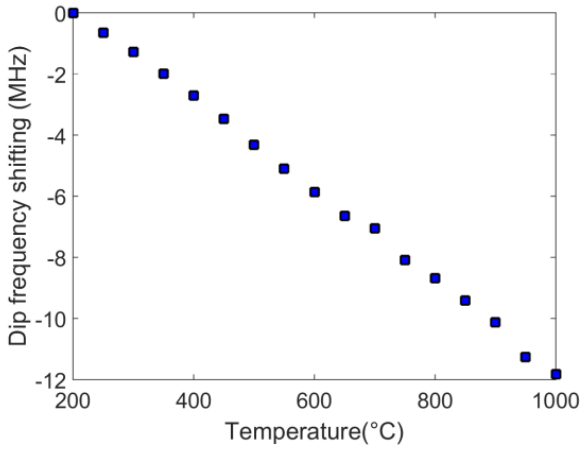

Fig. 3.4 Temperature response of the large core FSCF based OCMI

The temperature of the furnace was increased from 200 °C to 1000 °C with an increasing step of 50°C. Fig. 3.4 plots the frequency shift as a function of various temperatures at the interrogation frequency of 3.325 GHz. The temperature versus dip frequency shift slope was calculated as -15.54 kHz/°C by using Eq.(3.5), where L_T/L_t was equal to 40/65. The slope of the temperature versus dip frequency shift from the experiment is -15 kHz/°C, which is close to the calculated value. The temperature-strain crosstalk value was found to be 9.57 με /°C, which is relatively small in comparison with the one from traditional SMF with doped silica core.

3.1.3 Stability test

The stability of the sensor was first characterized at room temperature (±2°C temperature fluctuation should be taken into consideration) without applying any strain. The experiment data was taken by every 30 minutes, and the measurement has been last for 300 minutes. The recorded frequency shift over time was shown in Fig. 3.5. The STD

of the sensor was calculated to be around 20 kHz, corresponding to a relative measurement resolution of 6×10^{-6}, or 6 με.

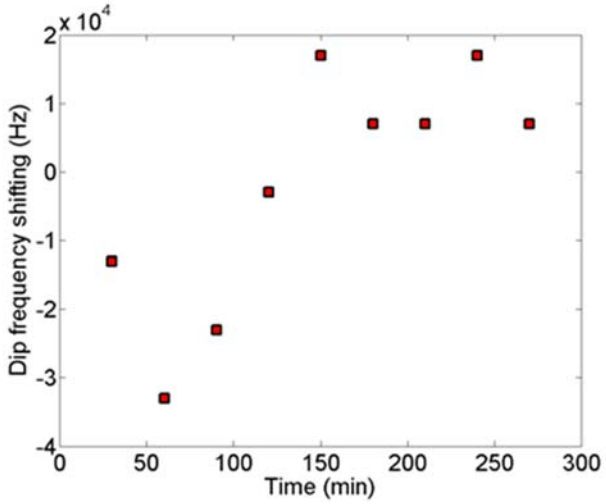

Fig. 3.5 Frequency drift of the interferogram dip at 3.325 GHz (shown in Fig. 3.2) versus time in room temperature for 300 minutes measurement.

In order to verify that the sensor can work well in high temperature environments, the stability of the sensor in high temperature has also been characterized. 40 cm of the sensing arm has been placed in the furnace whose temperature has been kept at 800 °C. The S_{21} spectrum has been recorded every 30 min for a duration of 100 hours. As shown in Fig. 3.6(a), the fringe visibility decreased as time progressed, which indicates that the attenuation for FSCF increased for exposing in high temperature environment, but the top level difference of the interference fringe indicates that no more than 2 dB attenuation occurred during the 100 h high temperature exposure. The drift of the fringe has been analyzed by monitoring the movement of the third dip with increasing of the time. As shown in Fig. 3.6 (b), the frequency drift scale is 10 times larger in high temperature than in room temperature. However, the drift includes the temperature variation of furnace,

which is about ±10 °C at the temperature of 800 °C, corresponding to frequency shift of $\pm 2 \times 10^5$ Hz at 3.25 GHz. The average value of the dip frequency drift approached zero as exposure time increased, indicating that no permanent diffusion happened during the 100 hour last. For the Germanium doped fiber sensor, at 800 °C, within 100 h the permanent refractive index change of the fiber core caused a measurement error of 1% [41]. The experimental results indicate that the sensor made from large core FSCF might have the stronger strain sensing capability at high temperature than those sensors made from a doped silica fiber.

3.1.4 Strain sensing in high temperature

To verify the high temperature sensing capability, strain has been applied to a Michelson-OCMI based optical fiber sensor made by FSCF. A sensor, with 76-cm length differences of sensing arm and reference arm was made. 40 cm out of 76 cm of the sensor was put inside a furnace. The temperature of the furnace was set at 300°C as starting point, and was increased by 100°C and held there for half an hour before doing the strain measurement. The temperature was increased to 900 °C. Fig. 3.7 shows the dip frequency versus the applied strain at different temperature, where the pink dot line on the top of the figure shows the strain response of the sensor at room temperature. The dark blue line on the bottom of the figure shows the results when the temperature of the furnace has been held at 900 °C. The frequency of the observing dip at zero-strain shifted due to the temperature change, but the lines of frequency shift as a function of strain under different temperatures are parallel with each other, indicating that the sensitivities for strain sensing were the same under different temperatures.

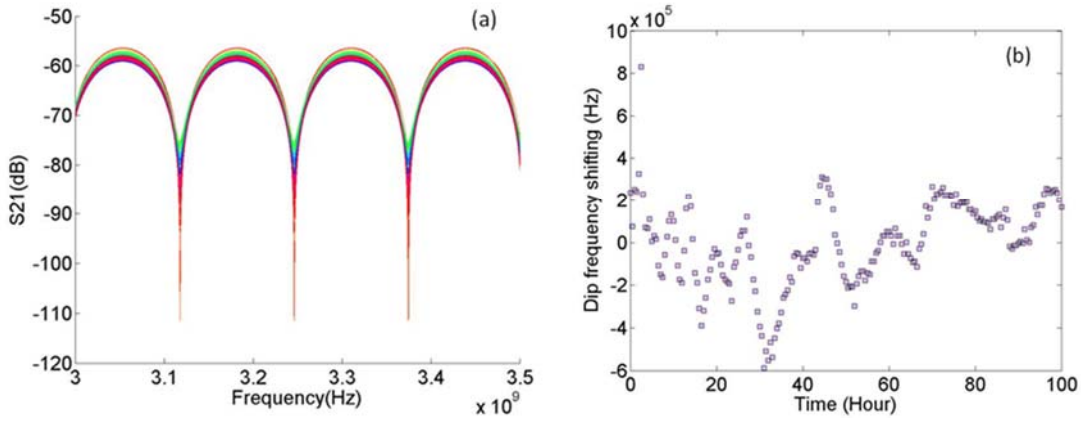

Fig. 3.6 100 hours stability test of the large core FSCF based OCMI at 800 °C. (a) Amplitude spectra of the S_{21} recorded at every 30 min during the 100 hours. (b) Frequency drifting of the 3rd dip at about 3.325 GHz versus time.

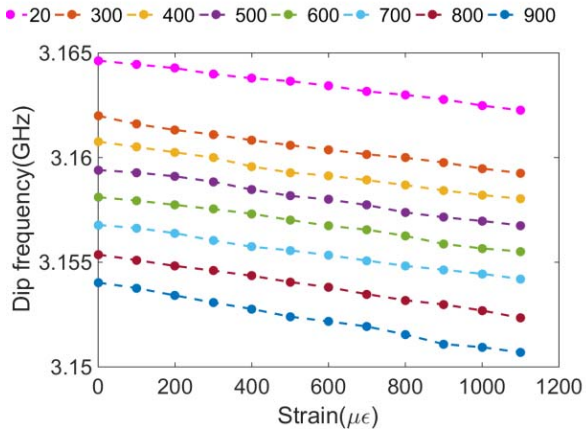

Fig. 3.7 Strain response of the large core FSCF based OCMI in different temperature. The pink dot line shows the results in room temperature, the dark blue dot line shows the results at temperature of 900 °C.

3.1.5 Conclusion

A Michelson-type OCMI has been demonstrated for strain sensing. Experimental results indicate that the strain sensitivity of the sensor is -2.622 kHz/ με at the initial

frequency of 3.325 GHz, and has a measurement resolution of 10 με at room temperature, which are in good agreement with the theoretical analysis. The sensor also has a linear temperature response, and can be used for strain sensing in high temperature environments. The temperature strain crosstalk of this sensor is 9.57 με/°C. These results indicate that the proposed sensor is competent with the existing technologies in terms of the sensitivity and measurement resolution for strain sensing. The stability testing results show that using the FSCF as sensor fabrication material could effectively enhance the sensor performance in high temperature environments, and it can also help to weaken the temperature-strain crosstalk.

3.2 Distributed sensing by using grade index MMF

In this section, a multimode fiber (MMF) based cascaded Fabry-Perot interferometer (FPI) type-OCMI has been demonstrated for distributed strain sensing [54]. The sensor is made with grade index MMF with core/cladding diameter of 62.5/125 um. 13 cascaded FPIs have been formed by 14 cascaded reflectors that have been fabricated on the fiber through femtosecond laser line-by-line irradiation. The large core size of the MMF makes the fabrication easier, and MMF based sensor is easy to assembled into a measurement system with low insertion loss. To verify the distributed sensing capability, strain was applied to the FPI formed by the first and second reflectors as well as the FPI formed by the fourth and fifth reflectors separately.

3.2.1 Sensor fabrication

We used Ti:sapphire fs laser (Coherent, Inc.) micromachining system to fabricate the reflectors. The central wavelength, pulse width, and repetition rate of the laser were

800 nm, 200 fs, and 250 kHz, respectively. The maximum output power of the laser was 1 W. The actual power used for fabrication was controlled by adjusting the laser beam optics, including a half-wave plate and a polarizer. The laser was switched on or off by electrically gating the internal clock. The actual laser energy used for fabrication was approximately 0.4 μJ per pulse [50,55].

The fiber used in experiments was a grade index MMF (Corning 62.5/125 Optical Fiber). The fiber was cleaned using acetone and clamped onto two bare fiber holders (Newport 561-FH). The optical fiber and fiber holders were immersed in distilled water during fabrication. The fiber assembly was mounted on a computer-controlled three-axis translation stage (Newport, Inc.) with a resolution of 0.1 μm. The fs laser beam was focused inside the optical fiber through a water immersion objective lens (Olympus UMPlanFL 20×) with a numerical aperture of 0.4. The spot size of the focused beam was about 1 μm in air. The velocities of the stages were set at 50 μm/s during fabrication. Fig. 3.8(a) shows a microscope image of a fabricated reflector. The microwave photonics system is connected with the MMF fiber which is under fabrication to monitor the reflectivity of each reflectors during the fabrication. In our experiment, the reflectivity of the reflector is in the scale of 10^{-3}. The whole reflector fabrication procedure can be accomplished within ten minutes.

The distances between two adjacent two reflectors were in the range of 60 to 70 cm. I did not precisely control the separation distances, because they did not change the demonstration results. However, as discussed in chapter 2, the distance is limited by the microwave frequency sweeping band. The minimum distance we can separate in time domain is inversely proportional to the bandwidth. For example, a 10 GHz microwave band,

the minimum distance we can separate in time domain is about 1 cm. Fig. 3.8(b) shows the time domain signal. The distance between two reflectors represents the light travel path difference between two reflectors, which is two times the physical length.

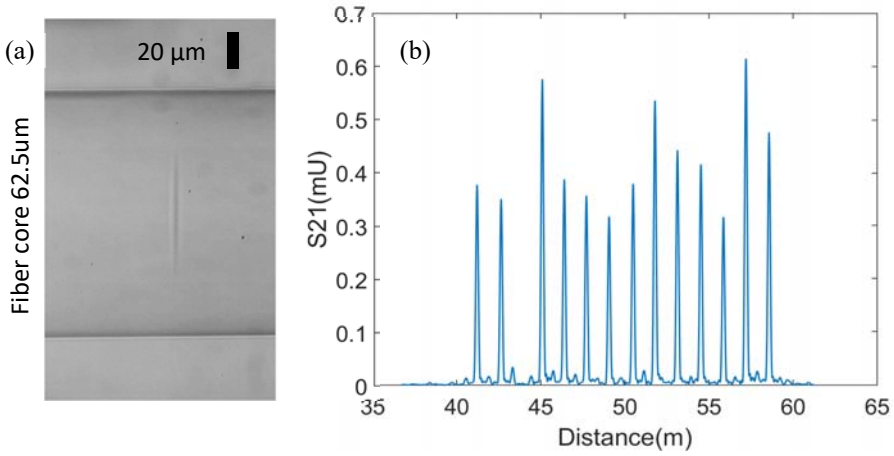

Fig. 3.8 (a)Microscope image of the fs laser fabricated reflector. (b)Reflectivity of each reflector in time domain

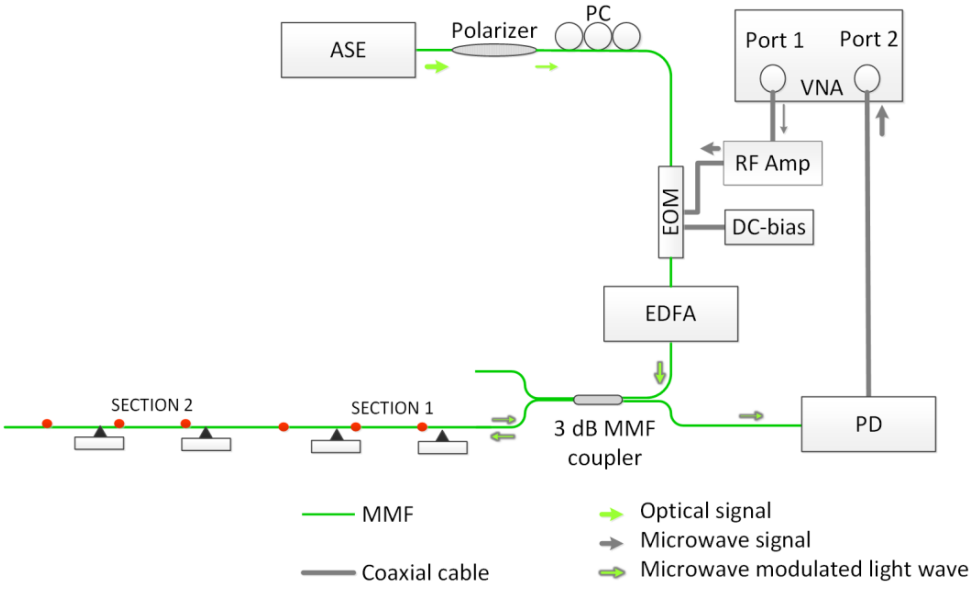

Fig. 3.9 Experiment setup. ASE: Amplified spontaneous emission light source (1530 – 1560 nm). PC: Polarization controller. EOM: electro-optic modulator. RF Amp: Microwave amplifier. PD: Photodetector.

3.2.2 Distributed stain measurement

Strain was applied to different two sections to demonstrate the distributed sensing capability of the MMF-based cascaded IFPI OCMI. The experimental setup is shown in Fig. 3.9. The VNA was configured to record the S_{21} signal with 16001 equally sampled data points. The IFBW was set to be 1 kHz. The frequency sweeping range was from 2 GHz to 4.5 GHz. First, the light from the broadband source (ASE, 1530 – 1560 nm) with an output power of 13 dBm is intensity modulated by a microwave signal through an electro-optic modulator (EOM, Pirelli Opto-Electric Components Team, Italy). An in-line fiber polarizer (Thorlabs, US) and a polarization controller (Thorlabs, US) followed by the light source were used to optimize the modulation depth of the EOM. The EOM was driven by the port 1 of a vector network analyzer (VNA Agilent E8364B) and has an insertion loss of around 6 dB. A bias DC source (3.6 V) was used for obtaining a highest modulation index.

Four manually controllable stages were aligned and fixed on the optical platform. As shown in Fig. 3.9, the SECTION 1 and SECTION 2 of the sensor were fixed on the four stages by using all-purpose glue (Loctite® Super Glue Ultra Liquid Control®). The fixing points were 0.5 cm away from the reflector 1, 2, 4, 5 respectively, and located outside

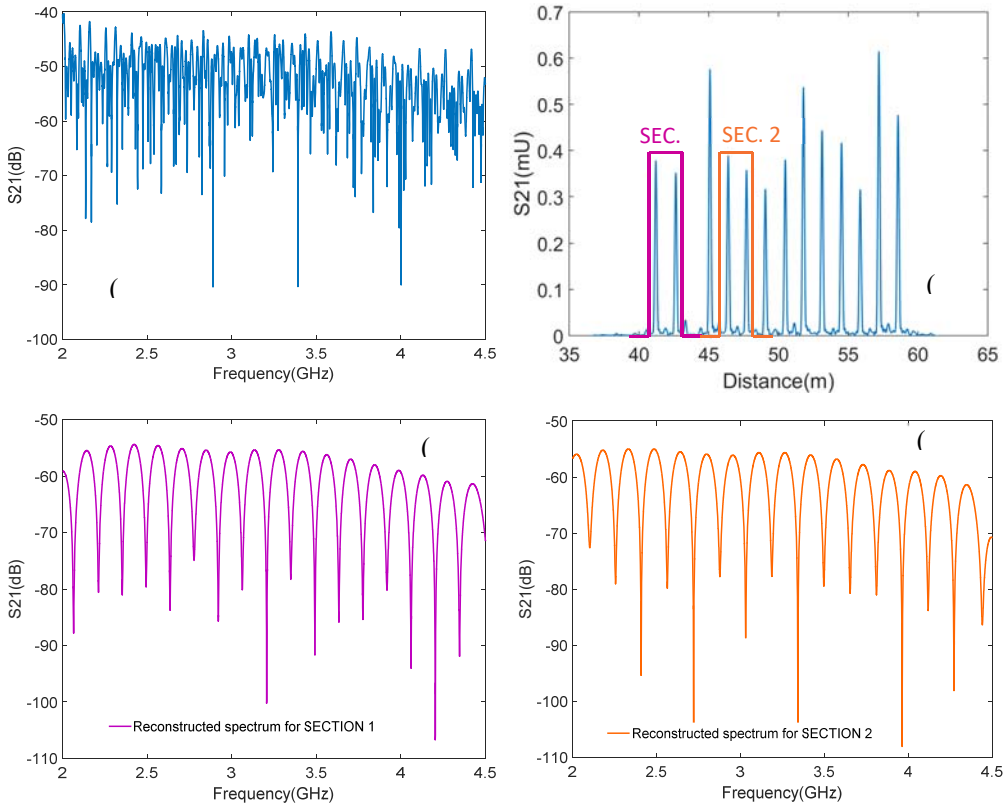

Fig. 3.10 (a) frequency domain signal reflected from the cascaded sensors; (b) time domain signal. The purple and orange lines are the time domain gates added on the SECTION 1 and 2 respectively. The reconstructed spectrum for (c) SECTION1 and (d) SECTION 2.

of the two sections. Strains with 100 εμ /step and 50 εμ /step were applied to the two sections separately. The frequency domain spectra were recorded for each step. The frequency domain spectrum at the initial state before applying any strain to the sensor is shown Fig. 3.10 (a). The time domain gates were multiplied to the FPIs formed by reflectors 1, 2 and reflector 4, 5 separately as shown in Fig. 3.10 (b). The reconstructed spectra for those two FPIs after multiplying the gate function were shown in Fig. 3.10 (c)

and (d). The dips (locates around 3.34 GHz) shifting corresponding to the applied strain on both the reconstructed spectra were monitored. Fig. 3.11(a) [(b)] shows when apply the strain to the SECTION 1[2], the reconstructed spectrum shifting for both section. The experiment results show that, the reconstructed spectrum shifts linearly to the applied strain for the section under the strain, while the other section only experiences slight spectrum variation ($f_{variation}$). The $f_{variation}/f_{dip}$ is in the scale of 10^{-5}, which reflects the sensitivity level of this distributed sensing system. Actually, the $f_{variation}$ is at the same level as the minimum strain the OCMI system can detect, and this indicates that the cross talk between the sections is small and the mode dispersion induced by MMF is not the major concern in this application.

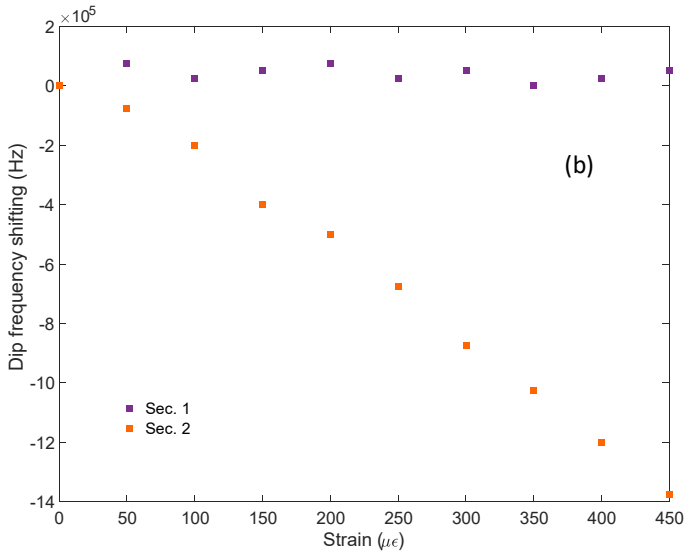

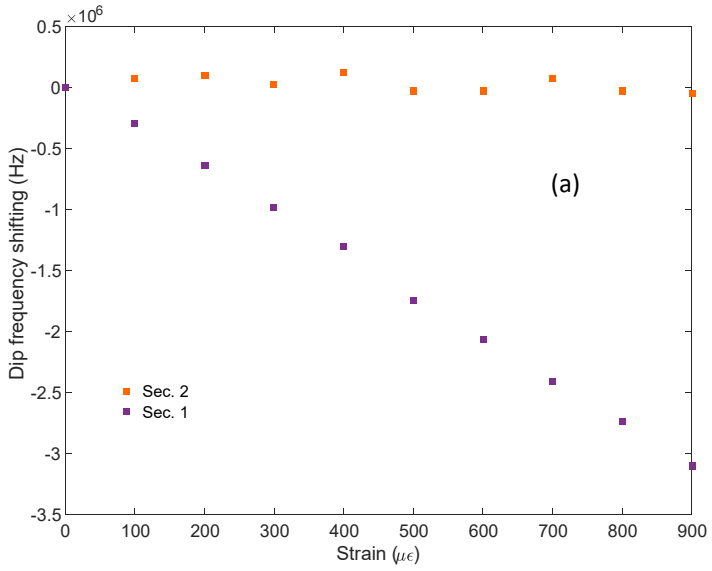

Fig. 3.11 Dip frequency shift (locates around 3.34 GHz) of the reconstructed frequency spectra for both SECTION 1 and 2, when applied strain on (a)SECTION 1 and (b) SECTION2

3.3 Distributed large strain measurement by using multimode polymer fiber

Polymer optical fibers (POFs) have many of the same advantages as silica optical fibers, including low weight, immunity to electromagnetic interference and multiplexing capabilities. In general, POFs provide a much lower cost alternative to silica optical fibers in short-haul applications [56], as they are easier to terminate, polish, and connect. POFs is more pliable than silica. POF has a shorter bend radius, and is more resilient to damage and abuse than glass due to its intrinsic material characteristics [57]. Because of POFs have the good tensile strength and large ultimate elongation, it is a very good candidate for the large strain sensing. It is possible to write fiber Bragg gratings in single POF [58], though it is hard to make single mode POF with low loss. Previously, sensors based on multimode

POFs have been usefully applied, but due to the characteristics of multimode fibers, these sensors generally produce lower measurement accuracy and resolution than single mode silica fiber sensors [59]. The POF fiber sensors utilized the MMF interference can have high sensitivity, however, they have the practical challenges in calibration after installation [45]. OCMI is insensitive to the types of optical waveguide. The difference in optics (e.g. dispersion and modal interference) have little influences on the OCMI signal, so it can integral MMF fabricated sensor into system and realize distributed sensing. It is promising to take advantages of POF to achieve distributed large strain based sensing, such as crack sensing by using the POF-OCMI configuration.

3.2.3 Sensor fabrication

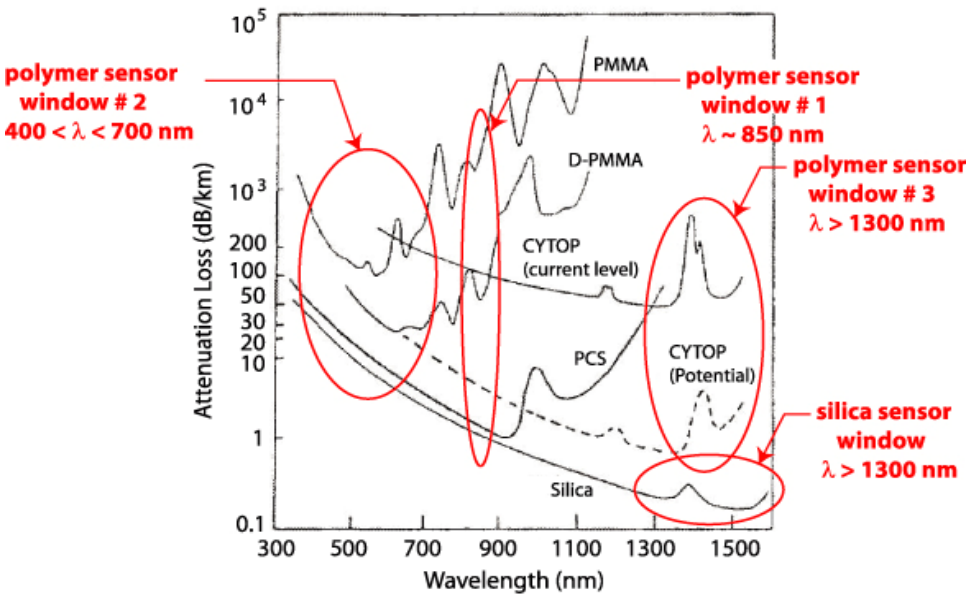

Fig. 3.12 Attenuation of common optical polymers as a function of wavelength [60]

The biggest limitation of POF is its high attenuation. The attenuation loss of POF is greater than that of glass fiber. Attenuation for glass fiber is generally in the range of 3 dB/km or less, but that for POF is generally in the range of 50 dB/km to 100 dB/km or more [60]. Consequently, glass fiber can transmit light for tens of kilometers without difficulties associated with loss, but POF is seldom useful in lengths over 100 m. The graded-index fiber and low-NA POF are two solutions to reduce attenuation problem [61]. Graded-index POF contains many layers of plastic, each with a lower index of refraction (the most dense plastic in the middle, and less-dense layers outward toward the surface of the fiber). Since light travels faster in the less-dense layers of plastic, the light rays refracted to the outside of the fiber race to match those traveling in the center, and thus enhances the capability for high-speed data transmission over a long distance.

The POF we used to fabricate the POF-OCMI sensors is caller GigaPOF from *Chromis Fiberoptics*, which is a perfluorinated (PF) grade index polymer optical fiber(GI-POF). One advantage of this POF is that it has low attenuation at inferred range. Fig. 3.12 shows the attenuation of different types of fibers as function of wavelength, where the attenuation for PF GI-POF at wavelength of 1550 nm is about 150 dB/ km. The core/cladding diameter of the GigaPOF fiber is 62.5/500 um respectively and the effective refractive index is 1.33. The core size of 62.5 um matches with the standard input and output port size of the optical communication equipment, though the numerical aperture (NA) of the GigaPOF is 0.185 ± 0.015 and the 62.5/500 μm grade index optical fiber usually has the NA of 0.275 ± 0.015, and the NA mismatching would induce power loss about 3.4 dB. The Fabry-Perot interferometer (FPI) fabricated by GigaPOF can be

integrated through the inferred microwave photonics system, where the modulation bandwidth can be larger than 10 GHz [62]. Compared with the visible light modulation whose bandwidth is normally below 1 GHz [63], the inferred microwave photonics system can provide a 10 times higher spatial resolution.

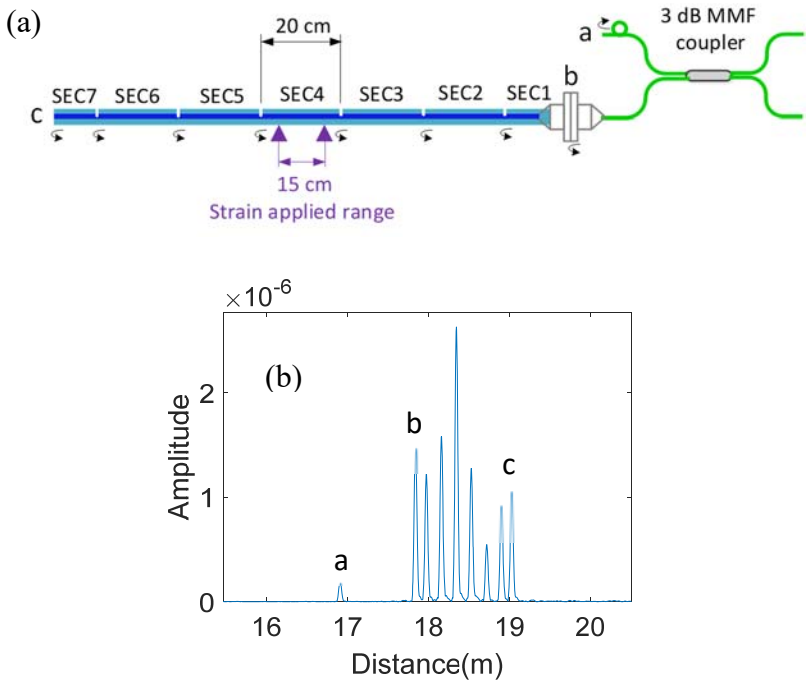

Fig. 3.13(a)Schematic of the cascaded sensors (b) Time domain signal. Pulse 'a' was generated by the terminated end of the other lead of the MMF coupler, pulse 'b' was generated by the FC to FC adaptor, pulse 'c' is generated by the unpolished end of the POF.

In POF-OCMI, the reflectors were basically a series of shallow air gaps on the POF, which were made by blade cutting. The POF was clamped onto two fiber holders and the fiber assembly was mounted on an optical table. The blade (double sides standard shaving

blade, edge thickness: 0.1 mm) was installed on the three-axis translation stage (Newport, Inc.) with a resolution of 0.1 μm. One edge of the blade was normal to the POF, and the cutting was achieved by vertically moving the blade 1 μm/step towards the cross-section center of the POF. One end of the POF was well polished and terminated by the FC connector. The assembled POF was connected with the microwave photonics system through FC to FC adaptor. The reflected light from the POF reflectors was injected into an index MMF (62.5/125) coupler. The reflectivity of each reflectors was monitored during the fabrication. The concentricity of core /over clad of the GigaPOF was about 5 μm, so each reflector was accomplished with different steps of cutting. The in-situ fabrication helped precisely control the reflectivity of each reflector. In our experiment, to prevent large loss induced by each reflector, all the gaps have the depth of less than 1 μm within the fiber core. The reflectivity of the reflector was in the scale of 10^{-3}. We fabricated six reflectors between two POF ends, and the distance between two adjacent reflectors are about 20 cm. Those reflectors along with the two POF ends formed 7 sections as shown in Fig. 3.13(a). The amplitude spectrum of the time domain signal is shown in Fig. 3.13(b), where pulse 'a' was generated by the terminated end of the other lead of the MMF coupler, pulse 'b' was generated by the FC to FC adaptor, pulse 'c' is generated by the unpolished end of the POF.

3.1.1 Distributed strain

The seven sections were seven cascaded FPIs. We fixed the SEC 4 on two translation stages (PM 500, Newport). To avoid stretching the blade induced air gaps, we placed the two fixing points inside of the section 4, and let them 15 cm apart from each

other. A piece of rubber was placed on the top of the fixing point to increase friction, all purposes glue was applied to the fixing point.

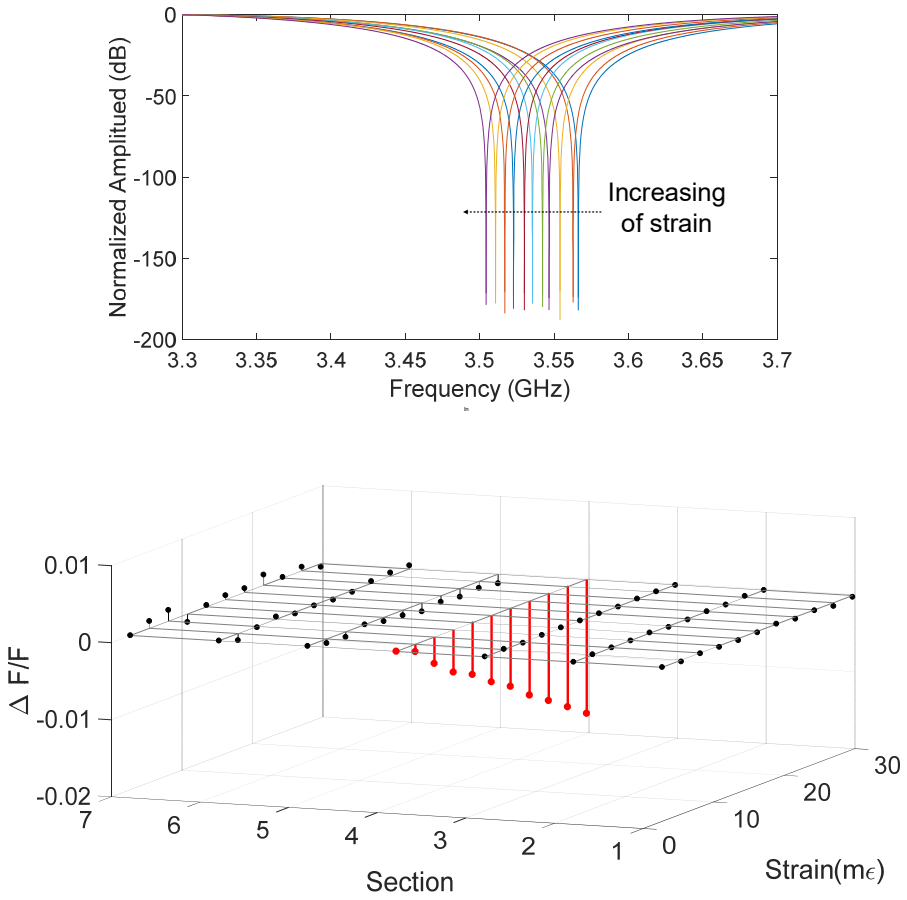

Fig. 3.14 Apply the strain (a) Reconstructed amplitude spectra for the section 4.

(b) Dip frequency shifting as function of strain for all the 7 sections

The VNA was set to have the number of sampling points of 16001 in the microwave bandwidth from 1 GHz to 6 GHz and the intermediate frequency bandwidth (IFBW) of 1 kHz. Axial strains of 2.7 mε per step were applied to the 14-cm regime by pulling the POF at distance of 400 μm per step. 10 forward steps were made first, and then 10 backward

steps. The fifth dip in the reconstructed S_{21} amplitude spectra for each section was taken for interrogation, of which the initial frequency fell within in the range of 3.3 GHz to 3.7

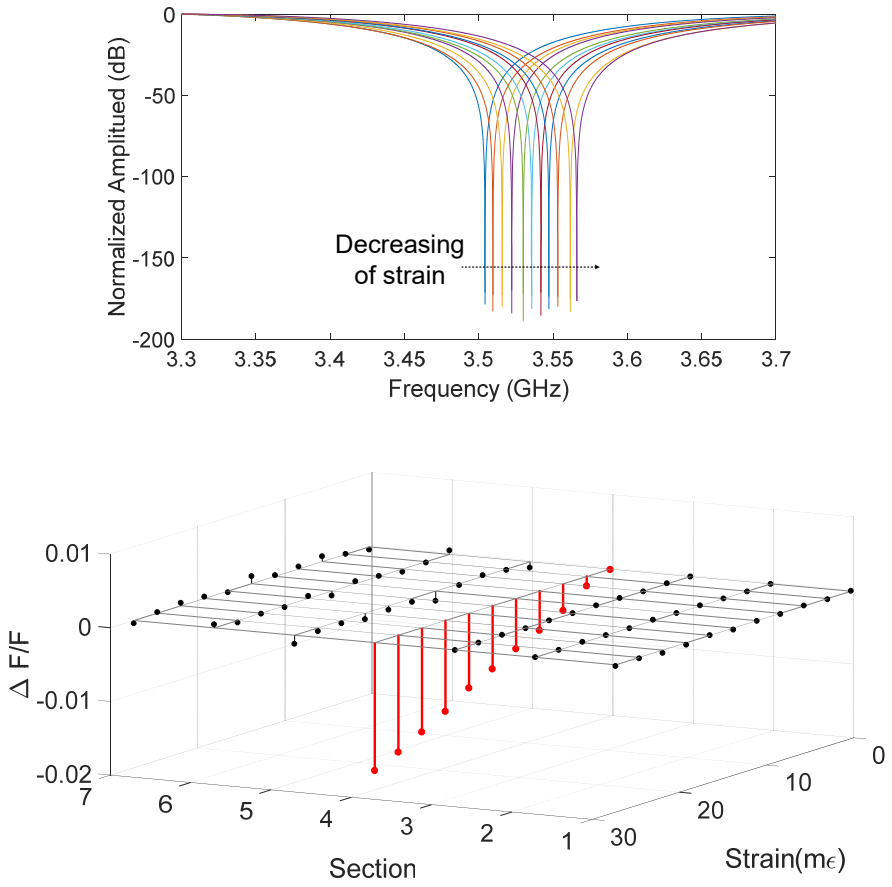

Fig. 3.15 Release the strain (a) Reconstructed amplitude spectra for the SEC4. (b) Dip frequency shifting as function of strain for all the 7 sections

GHz. The reconstructed frequency domain spectrum of SEC 4 shift linearly to the applied strain, while the reconstructed spectrum of other sections experienced slightly variance. Fig. 3.14(a) shows the reconstructed amplitude spectra for the section 4 under different applied strains. The total dip frequency changing for the interrogation dip was -62.015

MHz in response of 27 mε, where the initial dip frequency was 3.56 GHz. Fig. 3.14 (b) plots the ratio of the dip frequency shift to the initial frequency as a function of the applied axial strain for all the sections. The slope of the strain versus dip frequency shift for the section 4 was -2.3528 MHz/ mε, which is close to the calculated value (-2.4877 MHz/ με).

We released the strain step by step (2.7 mε per step) by moving the stage backwards. After 11 steps, the reconstructed spectra of the SEC4 shifted back to the original place. Fig. 3.15(a) shows the reconstructed amplitude spectra for the SEC4 as we release the strain, and Fig. 3.15 (b) shows the 5th dip frequency shift for all the 7 sections as function of the released strain. The frequency shift was still linear to the change of strain for SEC4, and the slope is 2.3528 MHz/ mε.

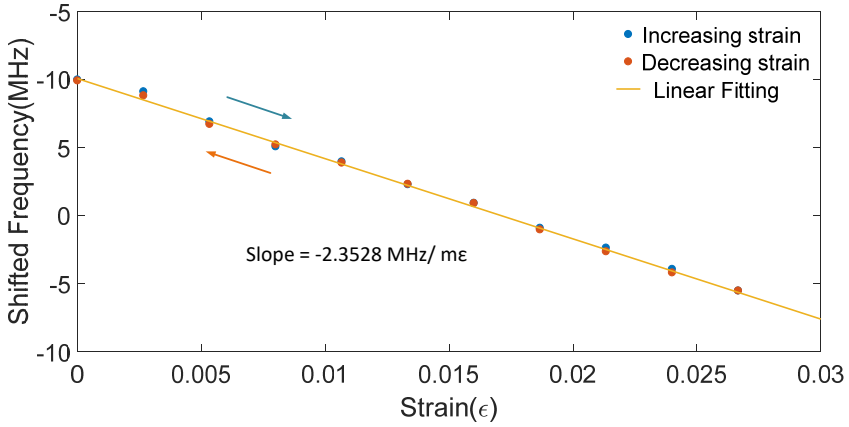

Fig. 3.16 Dip frequency shifting as function of strain of the section 4 when increasing strain (blue), and decreasing strain (red).

Fig. 3.16 shows the comparison of frequency shift to the increased and decreased strain of the reconstructed spectra for SEC4, and the it shows that with the same step of

increasing or decreasing the spectrum had the same amount of shifting but with opposite shifting direction. The experiment results indicate that this POF sensor can survive when the strain as large as 27 mε was applied.

All the reflectors were well protected to avoid the width of the airgap change generated reflectivity change, but when applied strain, the amplitude of the time domain signal shows dramatic change as shown in Fig. 3.17(a). The mode distribution inside of POF changed within the strain applied range, and it also changed the sections after that range. The effective refractive index changed slightly for those sections, and the most severely change was the reflectivity of the reflectors which located after the strain applied range. Fig. 3.17(b) shows the amplitude of each time domain pulse as function of the strain. The dramatic pulse amplitude change started at pulse 5, and toward to the fiber end. The change was not revertible, the pulse amplitude didn't go back when the strain released. The change also didn't follow an increase or decrease trend to the applied strain, which indicates that the change was not induced by the loss of the fiber. The reflectivity change results in the slightly shifting of the reconstructed spectrum for the related sections. It is clear that, in Fig. 3.14(b) and Fig. 3.15(b), the strain induced reconstructed spectra shift

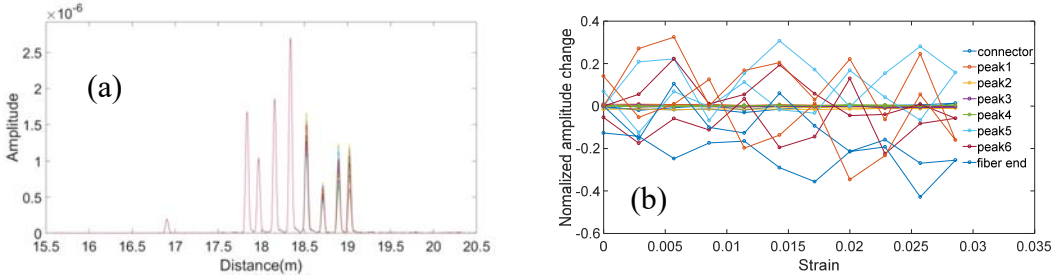

Fig. 3.17 (a)Amplitude of the time domain signal under different strain. (b) Normalized amplitude of the time domain pulse as function of strain

were larger for SECs 5, 6, 7 than those of SECs 1, 2, 3.

3.1.2 Strain distribution along beam

The young's modulus E is a measure of the stiffness of a solid material, and it defines the relationship between stress $\sigma(\varepsilon)$ and the strain ε, which can be calculated as

$$E = \frac{\sigma(\varepsilon)}{\varepsilon} = \frac{N/A}{\Delta L / L_0}, \tag{3.7}$$

where N is the force exerted on an object under tension, A is the actual cross-section area through which the force is applied; ΔL is the amount by which the length of object changes, L_0 is the original length of the object [64]. With the given force N, the strain is inversely proportional to the Young's modulus of the structure, and can be expressed as

$$\varepsilon = N / (E \cdot A). \tag{3.8}$$

When the object has uniform thickness, A for each discrete section of the object along the force applied direction is proportional to the width of cross-section.

9 reflectors along the POF were fabricated through blade cutting method as showed in the last section. The distance between two adjacent reflectors is about 5 cm. The whole POF with reflectors on part was bonded on a surface of 3 mm thick acryl beam through epoxy adhesive (LOCTITE EAE-20P). The surface of the beam was roughed by the sandpaper to avoid sliding. Two triangle shape symmetric notches were made on the beam to create the strain concentration area on the beam. The schematic of the described beam along with the bounded POF is shown Fig. 3.18(a). The POF-FPI formed by reflectors

segment the beam into 8 sections, and the POF-FPI formed by the 2nd and 3rd reflectors was cover the section 2 which had the notch on. Fig. 3.18(b) shows the photo of the embed polymer sensor round the notch area.

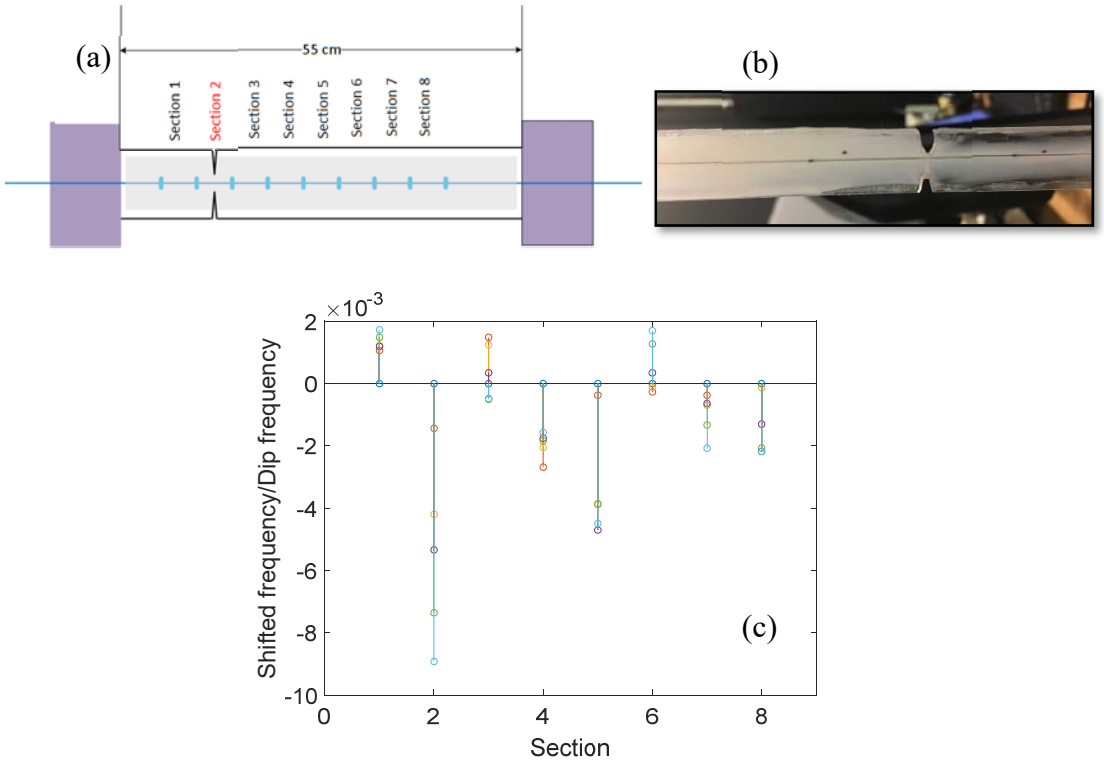

Fig. 3.18(a) schematic of the acryl beam along with the POF. (b) The acryl beam around the notch area. (c) Reconstructed spectra shifting under different applied displacement for all the sections

The beam was fixed on a force machine by clamping the two ends of the beam on the machine. Axial force was applied to the beam by giving displacement to one clamp step by step, and the strain distribution of the beam was got though OCMI method, by analyzing the shifting of the reconstructed spectra for each air gap formed POF-FPI. The

microwave bandwidth was set from 1G to 12 GHz with sampling points number of 16001, and the IFBW was set as 1 kHz. The dip fallen within the range of 5.2 GHz to 6.9 GHz was picked for the reconstructed spectra shifting tracking. Fig. 3.18(c) shows the shifting of the reconstructed spectra for each POF-FPI after each time of increasing. All the POF-FPI experience different scale of reconstructed spectra shift, and it is obvious that, the one on the top of section 2 had the largest shift of the reconstructed spectrum. This indicates that the average strain for section 2 is larger than the rest sections. The strain distribution along this acryl plat is similar to the strain distribution along around the crack area on the structure [1,65]. The results show that, it is possible to use the same setup to monitor the structure health, and when the crack happens, the sensor section with cross the crack should experience the largest reconstructed spectrum shift.

CHAPTER FOUR

COHERENT MICROWAVE-PHOTONICS INTERFEROMETRY (CMPI)

In last two chapters, OCMI technique has been demonstrated for fully distributed sensing with high spatial resolution and large measurement range [31]. However, the OCMI system only read the interference in microwave domain. As such the sensing resolution was low (in tens of με), limited by the IFBW of the microwave source. In this chapter, a new coherent microwave-photonics interferometry (CMPI) system for distributed optical fiber sensing is proposed. The system uses a coherent light source to obtain the optical interference signal from the cascaded weak reflectors for much improved sensitivity. In addition, the coherence length of the light source is carefully chosen or controlled to gate the signal so that distributed sensing can be achieved [66].

4.1 Mathematical model

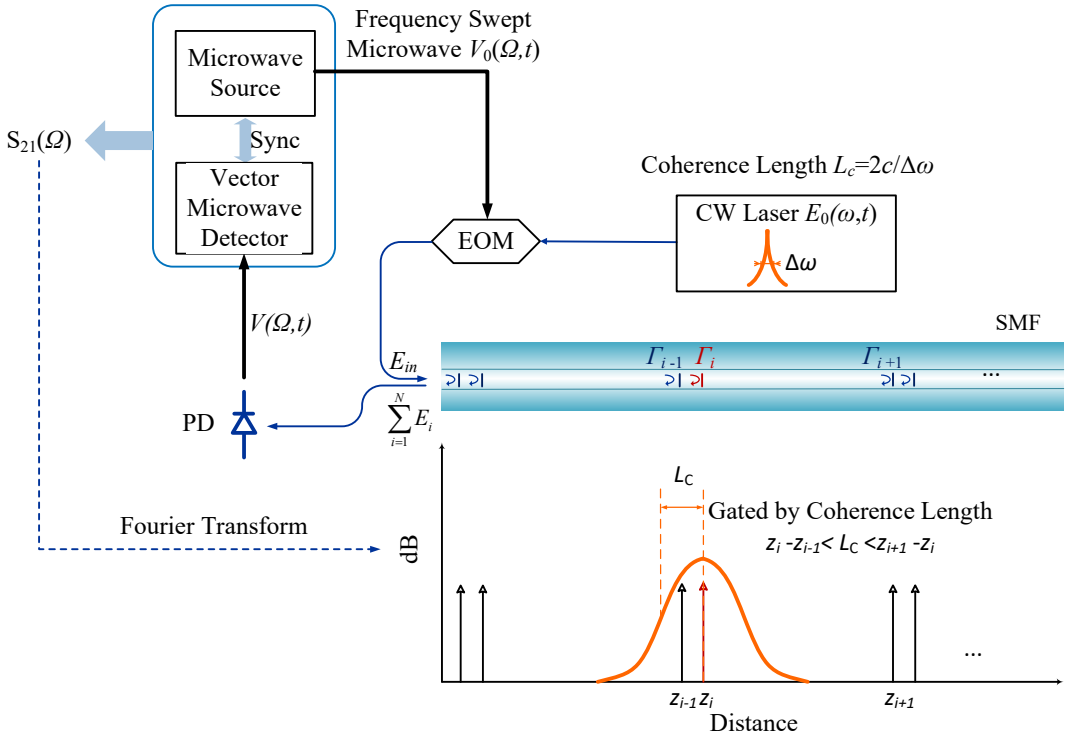

Fig. 4.1 Schematic illustration of coherent length gated microwave-photonics interferometry (CMPI). EOM: electro-optic modulator; PD: photodetector; S21(Ω) = V(Ω)/V0(Ω).

The proposed CMPI system is schematically shown in Fig. 4.1. The system this very similar as the OCMI system, but in CMPI, we choose narrow band light source with its coherence length L_c larger than the OPD between two adjacent reflectors (ith and jth reflector). As such, the cross-product term $\langle I_{cross}(\Omega,t)\rangle$ expressed in Eq. (2.8) becomes none

zero term, and cannot be ignored. Applying Taylor expansion to Eq.(2.8), we can find the fundamental frequency component of $\langle I_{cross}(\Omega,t)\rangle$, which is given by:

$$\begin{aligned}&\langle I_{cross}(\Omega,t)\rangle\big|_{\text{at }\Omega}\\&=\frac{M}{2}\sum_{i=1}^{N}\sum_{j\neq i}^{N}\left\{\int_{-\infty}^{\infty}A_{z_i}A_{z_j}\cos(\phi_i-\phi_j)d\omega\cdot\cos\frac{\Omega n(z_i-z_i)}{2c}\cdot\cos\left[\Omega t-\frac{\Omega n(z_i+z_j)}{2c}\right]\right\}\end{aligned}\tag{4.1}$$

Consequently, the complex frequency response of the system shown in Eq. (2.9) should be modified as

$$\begin{aligned}S_{21}(\Omega)&=\frac{1}{4}\sum_{i=1}^{N}mA_{z_i}{}^2e^{-\mathrm{j}\frac{\Omega nz_i}{c}}+\frac{1}{8\Delta\omega}\sum_{i=1}^{N}\sum_{j\neq i}^{N}mA_{z_i}A_{z_j}\int_{\Delta\omega}\cos(\phi_i-\phi_j)d\omega\cos\frac{\Omega n(z_i-z_i)}{2c}e^{-\mathrm{j}\frac{\Omega n}{2c}(z_i+z_j)}\\&=\frac{1}{4}\sum_{i=1}^{N}mA_{z_i}{}^2e^{-\mathrm{j}\frac{\Omega nz_i}{c}}+\frac{1}{8\Delta\omega}\sum_{i=1}^{N}\sum_{j\neq i}^{N}mA_{z_i}A_{z_j}\int_{\Delta\omega}\cos(\phi_i-\phi_j)d\omega\left(e^{-\mathrm{j}\frac{\Omega nz_i}{c}}+e^{-\mathrm{j}\frac{\Omega nz_j}{c}}\right)\end{aligned}\tag{4.2}$$

By applying complex Fourier transform to $S_{21}(\Omega)$, we obtain the time domain signal $F(t_z)$

$$F(t_z)=\frac{1}{4}\sum_{i=1}^{N}mI_N(z_i)\delta(t_z-\frac{nz_i}{c})\tag{4.3}$$

where t_z denotes the time variable. $F(t_z)$ is the superposition of N delta functions with different time delays nz_i/c, $I_N(z_i)$ is expressed as

$$I_N(z_i)=A_{z_i}{}^2+\frac{1}{\Delta\omega}\sum_{j\neq i}^{N}A_{z_i}A_{z_j}\int_{\Delta\omega}\cos(\phi_i-\phi_j)d\omega\tag{4.4}$$

As shown in Eq.(4.4), the amplitude $I_N(z_i)$ of each time domain pulse is the sum of two parts. The first part is a constant determined by the reflectivity of the reflector and the input light power. The second part is the superposition of the optical interference among the reflected lightwaves of the *i*th and any other reflectors in the system.

Now let's consider that the Lorentzian shape light source has a coherence length of Lc , which is inversely proportional to $\Delta\omega$, given by [67]

$$L_c = \frac{2c}{\Delta\omega}. \tag{4.5}$$

Eq. (4.4) can be simplified as

$$I_N(z_i) = A_{z_i}{}^2 + \sum_{j\neq i}^{N} A_{z_i} A_{z_j} \frac{L_c}{(z_i - z_j)n} \cdot \sin\frac{n(z_i - z_j)}{L_c} \cos\frac{\overline{\omega} n(z_i - z_j)}{c} \tag{4.6}$$

where $\overline{\omega}$ is the center optical frequency of the light source.

The coherence length L_c performs as a truncating function, which limits the number of reflectors contributing to the amplitude of the time domain pulse. If the OPD between the *j*th and *i*th reflectors is much larger than the coherence length of the light source L_c, the *j*th reflector's contribution becomes very small and can be neglected in Eq.(4.6). On the other hand, if the OPD between the *i*th and *j*th reflector is smaller than L_c, slightly change of the OPD can change the value of the second part dramatically. Thus, the amplitude variation of the time domain pulse can provide a sensitive indication of the OPD changes.

We can engineer the system to make sure that at any fiber location there are only two reflectors within the coherence length of the light source. It becomes apparent that we can either control the linewidth ($\Delta\omega$) of the optical source or the distance between two adjacent reflectors to include or exclude the reflectors to contribute to the second term of $I_N(z_i)$. If we further assume that the OPD between the two reflectors is much smaller than L_c, or $n(z_i - z_j)\pi << L_c$, then Eq. (4.6) can be simplified and approximated to be

$$I_2(z_i) = A_{z_i}{}^2 + A_{z_i} A_{z_j} \frac{L_c}{(z_i - z_j)n} \cdot \sin \frac{n(z_i - z_j)}{L_c} \cos \frac{\overline{\omega} n(z_i - z_j)}{c}$$
$$\approx A_{z_i}{}^2 + A_{z_i} A_{z_j} \cos \frac{\overline{\omega} n(z_i - z_j)}{c} \tag{4.7}$$

According to Eq. (4.7), $I_2(z_i)$ varies sinusoidally as a function of the OPD between the two reflectors. The period of the sinusoidal function equals to the average optical wavelength. A small change in OPD between the two reflectors can produce a detectable change in the amplitude of the time domain pulses. The locations of the reflectors can be identified by their corresponding position in the time axis. Therefore, the coherence gated microwave-photonic system can be used for distributed sensing with very high sensitivity.

When a coherent source is used, the optical interference between the *i*th and its neighbor reflectors makes the value of $I_N(z_i)$ a very sensitive function of the OPD change between those reflectors. On the other hand, because the microwave frequency (Ω) is much smaller than the light frequency (ω), a small change in distance z_i would cause an insignificant change in the microwave phase $\Phi_i(\Omega)$ than that in the optical phase $\phi_i(\omega)$. Thus, under the assumption of small change of z_i, the microwave phase terms in Eq. (4.2) become constant.

In reality, the sweeping microwave frequency has a limited bandwidth of Ω_b at the center frequency of Ω_c. To consider the limited bandwidth the time domain signal expressed in Eq. (4.3) should be modified to be

$$F'(t_z) = \left[\Omega_b \operatorname{sinc}(\Omega_b t_z) \mathrm{e}^{-j\Omega_c t_z} \right] * F(t_z)$$
$$= \sum_{i=1}^{N} \Omega_b \operatorname{sinc}\left[\Omega_b (t_z - \frac{nz_i}{c}) \right] \mathrm{e}^{-j\Omega_c (t_z - \frac{nz_i}{c})} I_N(z_i) \tag{4.8}$$

If the reflectors are far away from each other, the side lobes of the sinc functions can be ignored. The signal at the distance z_i can be approximated to be

$$F'_i(t_z) \approx \Omega_b \mathrm{sinc}\left[\Omega_b(t_z - \frac{nz_i}{c})\right] \mathrm{e}^{-j\Omega_c(t_z - \frac{nz_i}{c})} I_N(z_i) \tag{4.9}$$

4.2 Experiments, results and discussions

We have analytically shown that the CMPI system can effectively convert the OPD change between reflectors into the intensity change variation of the time domain pulses corresponding to the specific reflectors. The intensity of the time pulse changes as a function of OPD according to the optical interferometry formula which can be used to measure very small OPD variations for distributed sensing. To validate the proposed concept, we designed two sets of experiments. The first set of experiments using a pair of in-fiber reflectors to study the effects of the coherence length and cavity length to the performance of the sensor. The second set of experiments use an array of in-fiber reflectors to demonstrate the CMPI's capability for highly sensitive distributed sensing.

4.2.1 System configuration

The experiment setup to validate the CMPI concept for distributed sensing is shown in Fig. 4.2. Two types of light sources were used to study the coherence dependence of the system. The two sources had different linewidths which allow us to study the coherence length effect on the system. The first source was a tunable laser with a linewidth of 100 kHz (81640A, Agilent) whose coherence length was about 3km at the center wavelength of 1543nm. The second light source was a F-P laser (81554, HP). A single longitude mode of laser was filtered out by adding a 1nm band pass filter (BPF) after the laser. The single

longitude mode had a linewidth of about 1.5 GH at the center wavelength of 1543 nm, which had a coherence length of 6 cm.

The light from the source was intensity modulated by a microwave signal via an electro-optic modulator (EOM). An inline polarization controller (Thorlabs, US) was used to optimize the modulation depth of the EOM which was connected to the port 1 of a vector network analyzer (VNA Agilent E8364B). The microwave-modulated light output from the EOM was first amplified by an EDFA, and then launched into the port 1 of a fiber circulator. Port 2 of the fiber circulator was connected to the sensing fiber on which cascaded weak reflectors were fabricated using femtosecond laser micromachining [68,69]. Each two adjacent reflectors formed a weak reflection FPI. The reflected signals travelled back to the port 3 of the circulator and were further amplified by another EDFA. Another BPF was used to pass the signal and cut down the amplified spontaneous emission (ASE) of the EDFA. The filtered and amplified signal was detected by a high-speed photo-detector, which converted the optical signal into an electrical signal. The electrical signal was then connected to the port 2 of the VNA, which measured the amplitude and phase of the signal at the modulation frequency. After the VNA swept through the designated microwave bandwidth, the S21 spectrum was obtained which was further processed according to the method outlined in Section 2 to realize distributed sensing. In all the experiments below, the VNA was set to have the number of sampling points of 3201 in the microwave band and the intermediate frequency bandwidth (IFBW) of 5 kHz.

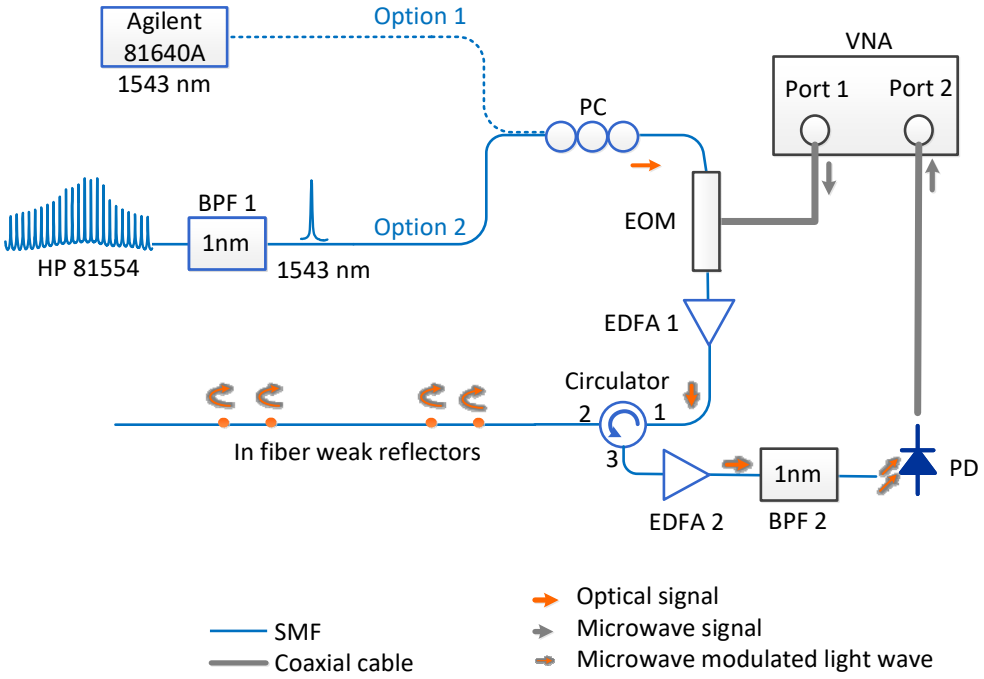

Fig. 4.2 Schematic of the system configuration for concept demonstration. Two types of light sources were used to study the coherence length effect on the system. EOM: Electro-optic modulator, EDFA: Erbium-doped fiber amplifier, PD: photodetector, BPF: band pass

4.2.2 System validation using a pair of reflectors

To validate the signal processing method given in Mathematical model, a single pair of reflectors separated by 10 cm were fabricated on a SMF by femtosecond laser micromachining. The femtosecond laser beam was focused into the fiber core to slightly modify the refractive index of the focusing area without striping the polymer coating of the fiber [68,69]. The two reflectors had very close reflectivity and they formed a weak

reflection FPI with a cavity length of 10 cm. The two fiber ends of the FPI were glued onto two motorized translation stages (PM500, Newport) respectively. The two fixing points were separated by 1.55 m and the FPI was positioned in the middle of the two stages. Axial strains were applied to the FPI by moving one stage at 1μm (corresponding to about 0.6 με) per step. The sweeping microwave bandwidth of the VNA was from 0.1 GHz to 4.1 GHz, and the tunable laser source (Option 1) was used in the experiment.

The amplitudes of the time domain signals under different applied strains are shown in Fig. 4.3(a). The insert shows the amplitudes of the two peaks (at the time points t_{s1} and t_{s2}) as function of the applied strain. The microwave bandwidth was large enough to separate the two reflectors as two time-domain pulses. It is obvious that the amplitudes of the two reflector pulses changed sensitively as a function of the applied strain. The changes of the two peak amplitudes were in phase. Fig. 4.3(b) plots the real part of the signal and the insert shows the peak of the real part at the time points t_{s1} and t_{s2} as a function of the applied strain. The amplitudes of the real part of the signal were also in phase. A close comparison of the Fig. 4.3 (a) and (b) also appears that the time-domain signal changed faster than the real part of the signal. The amplitude of the time domain signal shown in Fig. 4.3(a) is the absolute value of the cosine function of $I_N(z_i)$ given in Eq. (2.19) while the real part of the signal is the sinusoidal function itself. It has been reported that a cross phase modulation might be resulted in the intensity modulated light using an EOM [70]. The cross phase modulation is neglected in our derivations but deserves a detailed study in the future.

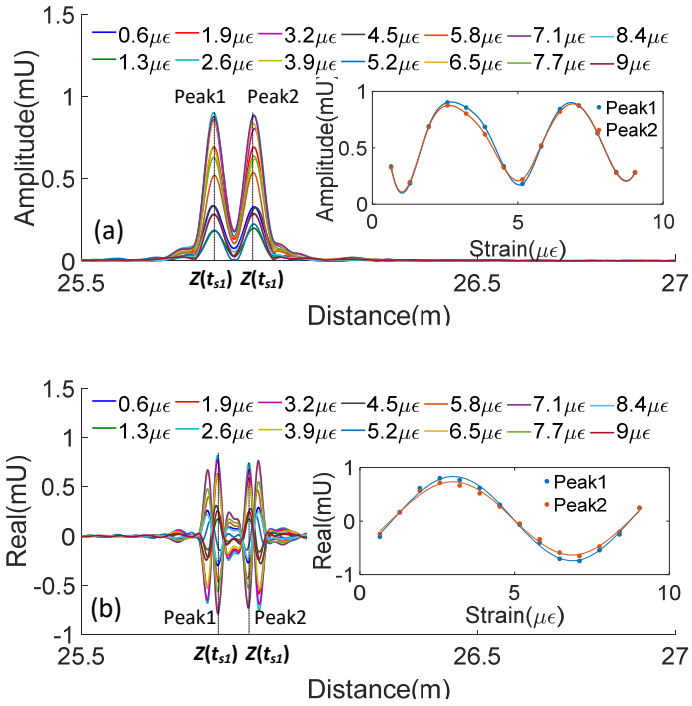

Fig. 4.3(a) Amplitude of the time-domain pulse under various applied strains using a microwave bandwidth of 4 GHz. Inset: amplitudes of the two peaks as a function of the applied stain. (b) Real parts of the time-domain signals shown in (a). Inset: amplitudes of the two peaks as function of the applied stain.

The period of the sinusoidal function is 7.2 με, which is slightly larger than the theoretical period 6.5 με got from Eq.(4.7), where we assume the effective strain-optic coefficient P_{eff} is about 0.204 [27]. Several possibly reasons lead to the mismatch. The major reason is that the fiber was glued on the stage without striping off the coating, so the applied strain didn't 100 percent transferred to the sensor due to the shear deformation at the coating and adhesive [71].

4.2.3 Dependence on the microwave bandwidth

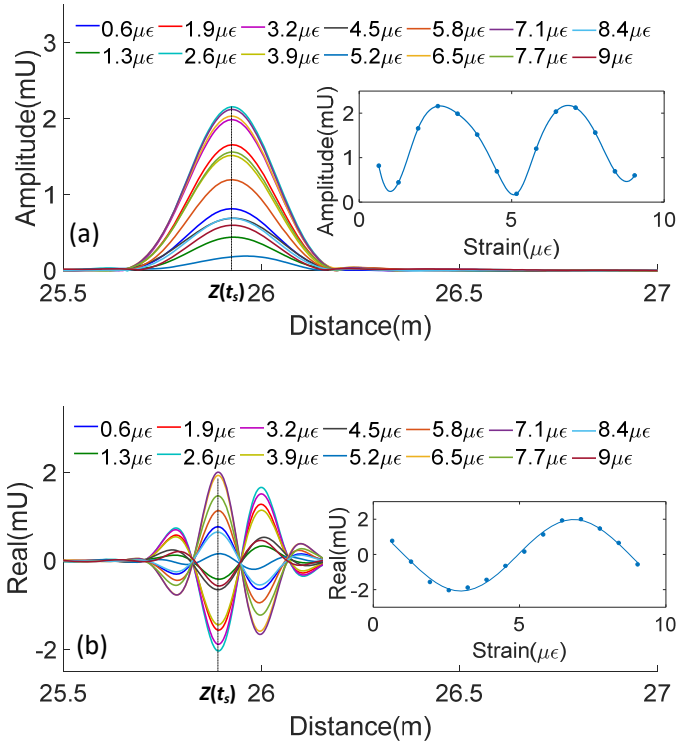

Fig. 4.4(a) Amplitude of the time-domain pulse under various applied strains using a microwave bandwidth of 0.8 GHz. Inset: amplitudes of the two peaks as a function of the applied stain. (b) Real parts of the time-domain signals shown in (a). Inset: amplitudes of the two peaks as function of the applied stain.

When the microwave bandwidth was chosen to be 4 GHz, the two reflectors spaced 10cm apart showed as two separate pulses in the time domain plot. It is worth to know what will happen if the microwave bandwidth becomes small and the individual reflectors cannot be resolved in the time domain. To experimentally investigate this, we reduced the microwave bandwidth to 0.8 GHz (from 1.1 GHz to 1.9 GHz). With the reduced bandwidth, the two pulses were inseparable. However, because the time domain signals of the two

reflectors ($I_2(z_i)$ and $I_2(z_j)$) have the same optical inference information and they are in phase, the combined time domain signal of these two reflectors should have the same response to the OPD change (in this case the applied strain) as the individual pulses.

Fig. 4.4(a) and (b) show the amplitude response and the real part of the signal as a function of the applied strain. The two pulses practically merged into one pulse in the time domain plots. The inserts of Fig. 4.4(a) and (b) plot the amplitudes of the time pulses as a function of the applied strain. It is obvious that the response of the merged pulse is very similar to that of the individual pulses, providing the same sensing information. This becomes very useful because smaller bandwidth means less data points to be processed and small cavities can also be read by the system.

4.2.4 Gating by coherence length

The coherence length of the light source limits the maximum distance between two adjacent reflectors that participate in optical interference. We can thus use the coherence length to select the specific reflector pair that will contribute to optical interference. In a general design, the cavity length should be smaller than the coherence length to obtain a high interference contrast. The distance between two adjacent FPIs (i.e., reflector pairs) needs to be much larger than the coherence length of the light source to avoid cross talks. Under this design, the optical coherence length determines the spatial resolution when the system is used for distributed sensing.

To verify the coherence length effect, we used the filtered F-P laser source (Option 2 in Fig. 4.2) whose single longitudinal mode had a linewidth of about 1.5 GHz,

corresponding to a coherence length of about 6 cm. Axial strains were applied to an FPI with a cavity length of 10 cm by using the same translation stages as described in section 3.2 (with the applied strain resolution of 1/1.55με per step). The microwave bandwidth was set to be 0.8 GHz (from 1.1 GHz to 1.9 GHz). Fig. 4.5(a) shows the comparison of using the two light sources, where the peak real values were normalized and plotted as a function of the applied strain. Using the tunable laser, the signal showed a clear interference pattern with a contrast close to 100%. When interrogated using the filtered F-P laser source, the signal was almost flat with a variation less than 1% because the OPD of the FPI was larger than the coherence length of the filtered F-P laser source [16]. Fig. 4.5 (b) shows the normalized peak real values change as a function of the applied strain for an FPI with a cavity length of 1 cm, interrogated by the filtered F-P laser source with the same VNA setup. This time, the contrast was about 80% because the coherence length (6 cm) was larger than the OPD (~ 2.9 cm). A similar experiment was performed to use the filtered F-P laser source to interrogate an FPI of 1 mm cavity length, whose OPD is much smaller than the coherence length and resulted in increased contrast of close to 100%.

4.2.5 Distributed strain measurement by using reflector array

The distributed sensing capability of the proposed CMPI technique was studied using an array of 29 cascaded reflectors as schematically shown in Fig. 4.6(a). Three different separation distances of 1mm, 1.5 cm and 30 cm between two adjacent reflectors were planned as shown in Fig. 4.6 (a). In theory, any two reflectors can form an FPI. However, only those two with a separation distance smaller than the coherence length of the light source can produce interference fringes with good visibility. The light source used in the

experiment was the filtered F-P laser with a linewidth of 1.5 GHz (Option 2 in 2). As a result, closely spaced two reflectors (i.e., separation distances of 1mm and 1.5 cm) will produce an optical interference signal, and the reflectors separated by a distance of 30 cm will not produce an optical interference. The microwave bandwidth was set to be 2 GHz, scanning from 2 to 4 GHz. Fig. 4.6 (b) shows the time domain signal of the distributed sensors where only 19 pulses can be seem because the small gapped reflectors (e.g., 1 mm and 1.5 cm) merged together when the microwave bandwidth was 2 GHz.

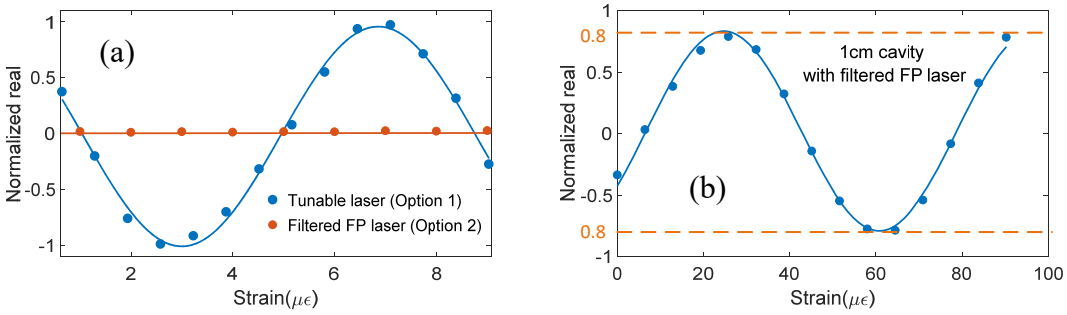

Fig. 4.5 Normalized real part of time pulses as function of strain (a) for the time domain pulse generated by the 10-cm cavity FPI by using two different linewidth light source; (b) for the time domain pulse generated by the 1-cm cavity FPI by using filtered F-P laser.

Axial strains of 0.6 με per step were applied to the range (1.55 m total length) marked as purple rectangular section shown in Fig. 4.6 (a) and (b) by pulling the fiber at a small distance of 1 μm per step using a translation stage. In this section, there are 6 time domain pulses shown in the inset of Fig. 4.6 (b), where I_4, I_5 and I_6 are the pairs of reflectors and the rest are single reflectors. Pulses I_4 and I_6 were formed by a pair of reflectors with a

separation distance of 1.5 cm, and Pulse I_5 was formed by a pair of reflectors with a separation distance of 1 mm. Because these three paired reflectors (I_4, I_5 and I_6) had

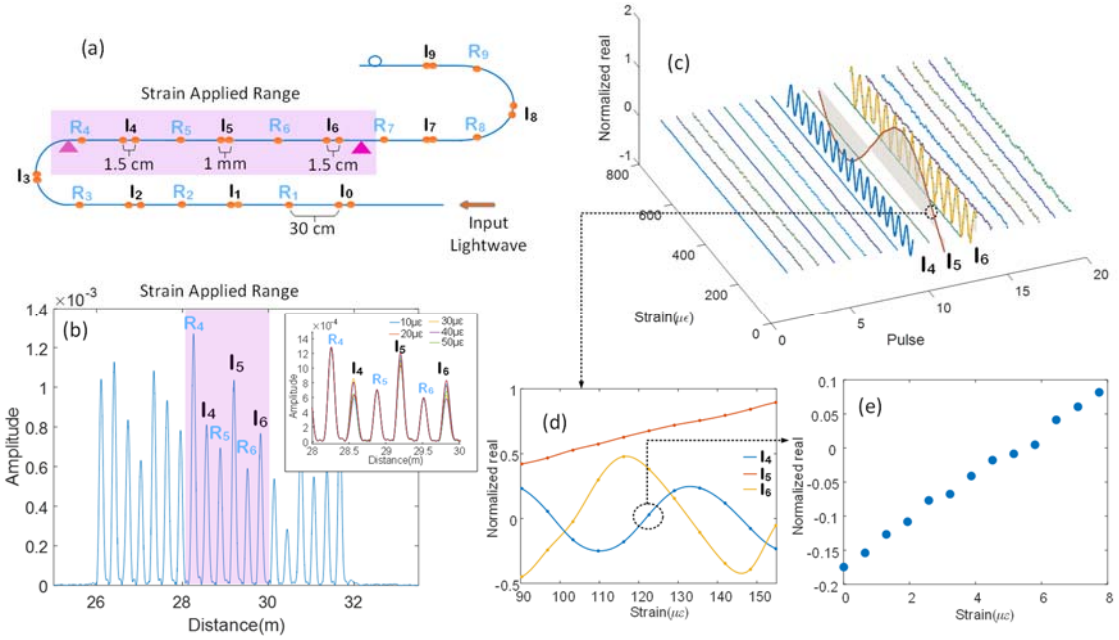

Fig. 4.6 Schematic of SMF distributed sensors with 29 cascaded reflectors. (b) Amplitude of the time domain signal, where the pulses with separation distance 1 mm and 1.5 cm from each other merged together. The inset shows the amplitude of the time domain signal under different applied strain within the strained section regime. A, B, C are the three merged pulses formed by the FPIs with cavity length of 1.5 cm, 1mm, and 1.5 cm respectively. (c) Normalized real part changes of the 19 pulses as a function of the applied strain. (d) Normalized real part changes for pulse A, B, C as function of strain around the quadrature point on the strain spectrum of A, which is circled in (c). (e)The zoomed in circled regime in (d)

separation distance smaller than the coherence length of the light source, their time domain

pulse amplitudes varied as a function of the applied strain as a result of effective optical interference. On the other hand, the pulse amplitudes of the single reflectors (located at R_4, R_5 and R_6) had shown negligible variation when the applied strain changed, because their distances to the adjacent reflectors were much larger than the coherence length of the light source.

Fig. 4.6 (c) plots the amplitudes (real part) of all time domain pulses as a function of strain and distance in 3D. The amplitudes of the I_4, I_5 and I_6 reflector pairs varied sinusoidally as the applied strain changed, while those of single reflectors remained almost unchanged as the applied strain varied. The experiment result proved that the coherence length of the light source could be used to optically isolate the reflectors based on their separations and optical interference contrasts. Using the microwave-photonic system, the locations of these reflector pairs can be clearly identified in the plot, indicating the distributed sensing capability of the system. The spatial resolution of the sensing system is determined by both the coherence length of the light source and microwave bandwidth, which are about 6 cm in this experiment. In real applications, the coherence length of the light source, the microwave bandwidth and the separation of the cascaded reflectors can be varied to fulfill the specific requirement in spatial resolution.

Fig. 4.6 (d) shows the zoomed-in plots of the amplitude (real value) variations of the I_4, I_5 and I_6 reflector pairs as a function of the applied strains (i.e., the circled region in Fig. 4.6 (c)). The amplitudes of the I_4, I_5 and I_6 pulses changed apparently with the applied strains as predicted by Eq.(4.7). Figure 6(e) shows the further zoomed-in plot of the amplitude of pulse I_4 (i.e., the circled region in Fig. 4.6 (d)) in response to the applied

strains of 7.2 με (or 12 steps) in total. The results clearly indicated that even a small strain step of 0.6 με could be resolved without ambiguity using the FPI with a cavity length of 1.5 cm, proving the very high measurement sensitivity of the system. The slightly offset of some individual points may be caused by two reasons. The first is the system error and the second is the inaccurate applied strain. In our case, the strain was applied using a translation stage with a nominal resolution of 0.1 μm and a repeatability of 0.2 μm. Such inaccuracy accounted for the major contribution of the offset in the experiment. Nevertheless, the sub-micron strain resolution is high comparing with other types of distributed sensing techniques, especially when considering the gauge length of the sensor is only 1.5 cm.

4.2.6 Strain sensitivity and dynamic range

Using Eq. (4.7), we can calculate the strain sensitivity of the individual sensors. If we assume that the i_{th} sensor (i.e., reflector pair) has a cavity length of $L_i = z_i - z_j$, the signal of the i_{th} sensor is

$$I_2(z_i) \approx \frac{m}{4}\left(A_{z_i}{}^2 + A_{z_i} A_{z_j} \cos\frac{\overline{\omega} n L_i}{c} \right) \tag{4.10}$$

By taking the partial derivative of L_i in Eq. 18, we have

$$\frac{\partial I_2(z_i)}{\partial L_i} = -\frac{\overline{\omega} n m}{4c} A_{z_i} A_{z_j} \sin\left(\frac{\overline{\omega} n L_i}{c} \right) \tag{4.11}$$

By plugging in the strain definition ($\varepsilon_i = \Delta L_i / L_i$) into Eq. (4.11), we obtain

$$\Delta I_2(z_i) = -\left[\frac{\overline{\omega} n m}{4c} L_i A_{z_i} A_{z_j} \sin\left(\frac{\overline{\omega} n L_i}{c} \right) \right] \varepsilon_i \tag{4.12}$$

Eq. (4.12) indicates that the change of signal amplitude is a sinusoidal function of the applied strain, meaning the sensitivity is nonlinear. In addition, the strain sensitivity is

proportional to the initial cavity length (L_i) of the sensor, which is the distance between two adjacent reflectors in our case. To further increase the strain sensitivity, we can increase the gauge length of the sensor by increasing the cavity length. This can be clearly seen in Fig. 4.6(d), with the same amount of applied strain of about 65 με, the amplitudes of long-cavity FPIs (I_4 and I_6, with a cavity length of 1.5 cm) changed more than an entire sinusoidal period while that of shorter cavity FPI (I_5 with a cavity length of 1 mm) varied much less than a sinusoidal period.

It took about 50 με to produce one period of change in amplitude when using the FPI with a cavity length of 1.5 cm as shown in Fig. 4.6 (d). This 1.5 cm cavity length FPI could clearly resolve 0.6 με in strain measurement as shown in Fig. 4.6 (e). For the FPI with a cavity length of 10 cm, the amplitude of the pulse changed an entire sinusoidal period with the amount of applied strain of about 7.2 με as shown in Fig. 4.3(b). This indicates that the 10-cm cavity FPI had much higher strain sensitivity than the 1.5-cm cavity FPI. We expect that the strain measurement sensitivity will further increase when the cavity length of the FPI increases, potentially reaching the nε level when the cavity length reaches 1m. However, the sensitivity is not linear as indicated by Eq. (4.12). The sensitivity is maximum in the quadrature region of the sinusoidal response curve, but it can become zero at the peak or valley of the sinusoidal curve.

Another issue is that the high sensitivity comes with a sacrifice in the dynamic range due to the sinusoidal nature of the signal, in which the 2μ ambiguity prevents the continuous tracking of the response curve in a range that is larger than the period. In general, there is a tradeoff between the sensitivity and the dynamic range. A long cavity length FPI

has a high strain resolution by a small dynamic range. The situation becomes opposite when the cavity length of the FPI is small.

Knowing this allows one to optimize the distributed sensing system in terms of sensitivity and dynamic range by choosing the proper separations of the reflector pairs (i.e., the cavity length of the FPI) at specific locations. This provides the desired flexibility to design a distributed sensing system to satisfy the different sensitivity and dynamic range needs at different locations in a specific application. In addition, we can use a combination of FPIs with different cavity lengths at a close proximity to achieve both large dynamic range and high sensitivity, if these FPIs are under the same applied strain.

Another interesting observation that can be made by comparing the two FPIs I_4 and I_6 which have about the same cavity length of 1.5 cm, in response to the applied strain as shown in Fig. 4.6 (d). First to notice is that their magnitudes are different which is due to the different reflectivity of the reflectors. The second is that their changing periods are about the same because they have about the same cavity length. The third is that the two response curves have a phase difference, which is caused by the initial cavity length difference between the two FPIs. This phase difference, if they can be adjusted to $\pi/2$ (quadrature phase shift), might be potentially to expand the dynamic measurement range based on bi-directional counting of the interference fringes.

CMIP is based on the measurement of the time-domain pulse amplitude of each FPI. The power fluctuations of the light source and microwave signal could induce measurement errors. To minimize the source power variation induced errors, a single reflector R_i (where i = 1, 2, 3..) just before each FPI I_i, as shown in Fig. 4.6 (a), can be

added to the system for compensation. The ratio between the amplitude of the single reflector and the reflector pair is not depended on the input power level. To verify this, we varied the input optical power by changing the gain of EDFA 1. Fig. 4.7(a) shows the time pulses before and after changing the power of the light source where the amplitudes changed significantly. However, the ratio between the amplitude of the reflector pair R_i, and that of the single reflector I_i just before it remained practically unchanged as shown in Fig. 4.7 (b). Because each FPI has a reference reflector located just before it, the power compensation should work when there is an optical loss in the middle of the fiber such as that caused by fiber bending.

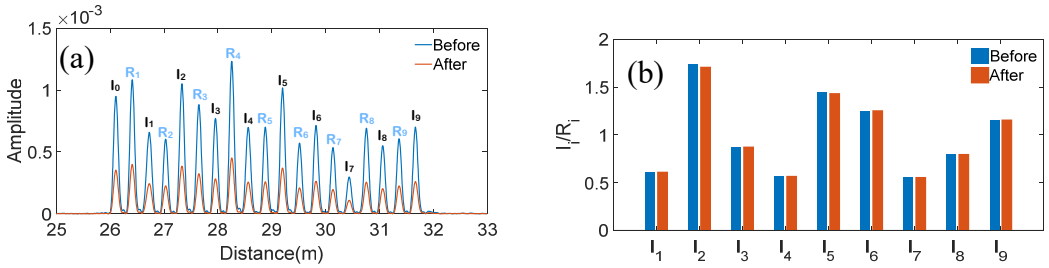

Fig. 4.7 Compensation for power fluctuation. (a) Time pulses at different power levels of the light source, showing as much as 2.7 times in power difference. (b) Power ratio between the FPI pair (I_i) and the single reflector(R_i) before it before and after input optical power change.

4.3 Conclusion

CMPI uses frequency measurement, and allows us to embed the optical carrier interference information into the microwave signal and covert the small OPD change into the huge vertical time domain pulse valued change; therefore, it offers key advantage of

the high sensing resolution. The experimental results indicated that the sensitivity for strain measurement can be much higher than 0.6με. There are three ways to further increase the sensitivity of the sensor. Making the reflectivity of the both faces of the FP cavity balanced, pre-strain the FP cavity and shifting the initial optical phase difference to the quadrature point, or slightly increasing the cavity length.

The time domain pulse value is optical carrier power based, so the measurement accuracy of CMPI relies on the power stability of the light source. However, the slightly power change would show as the value change of all the time domain pulses, and we could decrease the power instability effects by setting a time domain pulse from single reflector as power reference. The drifting of the center frequency of the optical carrier also can cause the sensing error, and the effect is even more dramatic when the larger cavity has been used. Setting a reference cavity and put it within temperature well controlled environment is one way to compensate the centerline drifting caused sensing signal error.

There's a trade-off between sensitivity and the dynamic measurement range which is limited by the 2π ambiguity. To increase the measurement range while maintain the high sensitivity, one approach is to cascade FPIs with different cavity length, and use strain spectrum of the shorter-length cavity to locate the respective period on the strain spectrum of the large cavity FPI, and then get the precise strain information. Another approach is use narrow band optical carrier to do the high resolution measurement within small changing range, and then switch to wide band light source to use OCMI to read the large scale change [50]. Also, the traditional fringe counting approach in optical interference is expected to be used to resolve the 2π ambiguity in the future work.

CHAPTER FIVE

DISTRIBUTED DYNAMIC MEASUREMENT BASED ON CMPI

There is a growing demand for measuring dynamic perturbation in the geophysics [72] , civil engineering [2], and the industry of oil and gas [73], etc. Fiber optical sensors are deployed for distributed dynamic measurement in recent years [74]. The high sensitivity and fast response are required for the sensing technologies to read the high frequency and low magnitude perturbations, such as the ground vibration caused by seismic wave. The interferometric based distributed sensing technology has the advantage of high sensitivity, thus addressed high attentions for reading the dynamic information from the low magnitude vibration [75,76]. However, most of the interferometric based sensing technology cannot support multipoint testing and the spatial resolution is low. Φ-OTDR relies on the localized optical interference., and has the capability to perform multipoint vibration measurement [73–75], but it is challenge to read the vibration amplitude from the signal unless complex phase recovery methods are deployed [11].

In chapters 2 and 3 a fully distributed fiber optic sensing technology based on optical carrier based microwave interferometry (OCMI) is demonstrated [31]. The OCMI has numbers of unique advantages including high signal quality, relieved requirement on fabrication, low dependence on the types of optical waveguides, insensitive to the variations of polarization, high spatial resolution, and fully distributed sensing capability. However, OCMI system reads the interference in microwave domain. Limited by the scan

rate of the microwave instrument the maximum vibration sensing rate of the reported OCMI system is several Hz as demonstrated in chapter 2.

In chapter 4, a sensitivity enhanced distributed sensing method based on coherent light microwave-photonics interferometry (CMPI) is presented. The system utilizes a coherent light source with its coherence length larger than the distance between two adjacent weak reflectors in a single-mode fiber (SMF). As a result, the optical interference between two adjacent reflectors is nonzero and recorded as part of the microwave signal. By adjusting the microwave bandwidth, the optical interference signal can be derived based on the peak amplitude of the pulses in the time (distance) domain which is obtained by complex Fourier transform of the microwave S_{21} spectrum. The peak amplitude of the microwave pulse varies as the optical path difference changes as a result of the applied strain. The scan rate of the microwave instrument is the same as when we use the OCMI system, however, CMPI based on the power measurement, and the small OPD change at any location along the sensing system within a small-time frame would immediately show as the amplitude change for the respective scanned microwave frequency band within that time frame. When the vibration induced periodically changed strain happens between two adjacent reflectors within the time of one microwave frequency scan, the vibration location, intensity and frequency can be retrieved from the time domain signal.

In this chapter, a new sensing signal processing method is provided for the distributed dynamic measurement based on the CMPI. The theoretical analyse and experiment results show that this method has the capability to perform the sub scan rate vibration measurement of up to 20.832 kHz.

5.1 Mathematical model

Let's start with two reflector (i , j) CMPI system, and assume the OPD of the two reflected wave is much smaller than the coherence length of the optical carrier, the time varied S_{21} can be evolved from Eq. (4.2) and expressed as

$$S_{21}(t,\Omega)=\frac{1}{4}\sum_{i=1}^{2}mA_{z_i}{}^2e^{-\mathrm{j}\frac{\Omega nz_i}{c}}+\frac{1}{4}\sum_{i=1}^{N}\sum_{j\neq i}^{N}mA_{z_i}A_{z_j}\cos\left[\Delta\phi_{ij}(t)\right]\left(e^{-\mathrm{j}\frac{\Omega nz_i}{c}}+e^{-\mathrm{j}\frac{\Omega nz_j}{c}}\right), \tag{5.1}$$

where $\Delta\phi_{ij}(t)=\Delta z_{ij}(t)n\omega/c$. If $\Delta z_{ij}(t)$ changes sinusoidally to the time due to the vibration, it can be expressed as

$$\Delta z_{ij}(t)=(z_i-z_j)+\delta z\cos(\Theta t) \tag{5.2}$$

where Θ is the vibration frequency, δz is the amplitude of the vibration (assume $|\delta z|<<\frac{1}{2}\lambda_c$, where λ_c is the center wavelength of the optical carrier).

In above equations, t is the time point when sweeping the frequency Ω . The frequency is sampled with equal interval $\Delta\Omega$, and if the dwelling time for each swept frequency is a constant Δt , we can express

$$t=\Omega/\Delta\Omega\cdot\Delta t \tag{5.3}$$

Since t and Ω are correlated, Eq. (5.1) can be written as

$$S_{21}(\Omega)=\frac{1}{4}\sum_{i=1}^{2}mA_{z_i}{}^2e^{-\mathrm{j}\frac{\Omega nz_i}{c}}+\frac{1}{4}mA_{z_i}A_{z_j}$$
$$\underbrace{\cdot\cos\left\{\left[(z_i-z_j)+\delta z\cos(\Theta\Omega/\Delta\Omega\cdot\Delta t)\right]n\omega/c\right\}}_{\text{dynamic term}}\left(e^{-\mathrm{j}\frac{\Omega nz_i}{c}}+e^{-\mathrm{j}\frac{\Omega nz_j}{c}}\right) \tag{5.4}$$

The blue term in Eq. (5.4) is sensitive to the optical phase change, and after applying Euler's formula it can be expanded as

$$\begin{aligned}\text{dynamic term} = &\frac{1}{2}\exp\left[j(z_i - z_j)n\omega / c\right]\cdot\exp\left[j\delta z\cos(\Theta\Omega / \Delta\Omega\cdot\Delta t)n\omega / c\right]\\ &+\frac{1}{2}\exp\left[-j(z_i - z_j)n\omega / c\right]\cdot\exp\left[-j\delta z\cos(\Theta\Omega / \Delta\Omega\cdot\Delta t)n\omega / c\right]\end{aligned} \tag{5.5}$$

We assumed that $\delta z \ll \lambda_c / 2$, thus the $\delta z n\omega / c \ll 1$. by using Taylor expansion,

$$\begin{aligned}\text{dynamic term} \approx &\frac{1}{2}\exp\left[j(z_i - z_j)n\omega / c\right]\cdot(1 + j\delta z\cos(\Theta\Omega / \Delta\Omega\cdot\Delta t)n\omega / c)\\ &+\frac{1}{2}\exp\left[-j(z_i - z_j)n\omega / c\right]\cdot(1 - j\delta z\cos(\Theta\Omega / \Delta\Omega\cdot\Delta t)n\omega / c)\end{aligned} \tag{5.6}$$

Expand the sin term in Eq. (5.6) results in

$$\begin{aligned}\text{dynamic term} = &\frac{1}{2}\exp\left[j(z_i - z_j)n\omega / c\right]\cdot\left[1 + \frac{j}{2}\delta z n\omega / c\left(e^{\mathrm{j}\Theta\Omega/\Delta\Omega\cdot\Delta t} + e^{-\mathrm{j}\Theta\Omega/\Delta\Omega\cdot\Delta t}\right)\right]\\ &+\frac{1}{2}\exp\left[-j(z_i - z_j)n\omega / c\right]\cdot\left[1 - \frac{j}{2}\delta z n\omega / c\left(e^{\mathrm{j}\Theta\Omega/\Delta\Omega\cdot\Delta t} + e^{-\mathrm{j}\Theta\Omega/\Delta\Omega\cdot\Delta t}\right)\right]\\ &= \cos\frac{(z_i - z_j)n\omega}{c} - \frac{1}{2}\delta z n\omega / c\left(e^{j\Theta\Omega/\Delta\Omega\cdot\Delta t} - e^{-j\Theta\Omega/\Delta\Omega\cdot\Delta t}\right)\sin\frac{(z_i - z_j)n\omega}{c}\end{aligned} \tag{5.7}$$

Substitute Eq. (5.7) and into Eq. (5.4) for dynamic term, and the Fourier transform of the $S_{21}(\Omega)$ can be expressed as

$$\begin{aligned}F(t_z) = &\frac{1}{4}mA_{z_i}{}^2\delta(t_z - \frac{nz_i}{c}) + \frac{1}{4}mA_{z_j}{}^2\delta(t_z - \frac{nz_j}{c})\\ &+\frac{1}{4}mA_{z_i}A_{z_j}\left\{\cos\frac{(z_i - z_j)n\omega}{c}\cdot\left[\delta(t_z - \frac{nz_i}{c}) + \delta(t_z - \frac{nz_j}{c})\right]\right.\\ &-\frac{1}{2}\delta z n\omega / c\cdot\sin\frac{(z_i - z_j)n\omega}{c}\cdot\left[\delta(t_z - \frac{nz_i}{c} + \Theta / \Delta\Omega\cdot\Delta t) - \delta(t_z - \frac{nz_i}{c} - \Theta / \Delta\Omega\cdot\Delta t)\right.\\ &\left.\left.+\delta(t_z - \frac{nz_j}{c} + \Theta / \Delta\Omega\cdot\Delta t) - \delta(t_z - \frac{nz_j}{c} - \Theta / \Delta\Omega\cdot\Delta t)\right]\right\}\end{aligned} \tag{5.8}$$

The red colored terms are the time pules generated by the vibration. Those time pulses show in pairs for one vibrate frequency. The location of the pulses in one pair are symmetric to the location of the reflector, and the distance is proportional to the vibrate frequency with a scaling coefficient of $\Delta t / \Delta\Omega$. The neat thing about this system for the dynamic measurement is that the amplitude of the vibration generated time pulse has been amplified by the optical frequency. The vibration induced OPD change about half wave length of the optical carrier (1550 nm) induce the same amplitude level of pulse to the optical interference part of the main pulse.

In most scenarios the vibrations have a small DC offset δz_{dc} ($\left|\delta z_{dc}\right| \ll \frac{1}{2}\lambda_c$, and Eq. (5.2) should be modified as

$$\Delta z_{ij}(t)_{ac+dc} = (z_i - z_j) + \delta z \cos(\Theta t) + \delta z_{dc}. \tag{5.9}$$

Then Eq. (5.8) is modified as

$$\begin{aligned}
F(t_z)_{ac+dc} &= \frac{1}{4} m A_{z_i}{}^2 \delta(t_z - \frac{nz_i}{c}) + \frac{1}{4} m A_{z_j}{}^2 \delta(t_z - \frac{nz_j}{c}) \\
&+ \frac{1}{4} m A_{z_i} A_{z_j} \left\{ \cos \frac{\left(z_i - z_j + \delta z_{dc}\right) n\omega}{c} \left[\delta(t_z - \frac{nz_i}{c}) + \delta(t_z - \frac{nz_j}{c}) \right] \right. \\
&- \frac{1}{2} \delta z n\omega / c \cdot \sin \frac{\left(z_i - z_j + \delta z_{dc}\right) n\omega}{c} \left[\delta(t_z - \frac{nz_i}{c} + \Theta / \Delta\Omega \cdot \Delta t) - \delta(t_z - \frac{nz_i}{c} - \Theta / \Delta\Omega \cdot \Delta t) \right. \\
&\left. \left. \delta(t_z - \frac{nz_j}{c} + \Theta / \Delta\Omega \cdot \Delta t) - \delta(t_z - \frac{nz_j}{c} - \Theta / \Delta\Omega \cdot \Delta t) \right] \right\} \cdot
\end{aligned} \tag{5.10}$$

According to above equation, if there's a DC strain added onto the periodical changed strain, besides the emerging of the side lobes, the main lobe of the time pulse at the respective location will also show the amplitude change.

5.2 Performance characterization

5.2.1 Frequency measurement range

The largest vibration frequency ($f_{\text{vib,max}}$) that can be measured through this method is inversely proportional to the dwelling time (t_{dwelling}) at each swept frequency, which is expressed as

$$f_{vib,max} = \frac{1}{2t_{dwelling}} \tag{5.11}$$

The dwelling time for each swept frequency point is decided by the IFBW of VNA, the larger the IFBW is the shorter the dwelling time will be. The minimum dwelling time for the VNA we were using (E8363B, Keysight) was 24.001 μs, thus the maximum frequency $f_{\text{vib,max}}$ the system can detect is 20.832 kHz.

5.2.2 Frequency resolution

This method can be used for multi points vibration measure, and if each vibrate source has single frequency, the vibration frequency can be found for each vibrate source location and the respective vibrate frequency no matter what are the frequency differences between vibrate sources. However, if one location has been vibrated by more than one frequencies, the smallest frequency difference that the system can resolve is inversely proportional to the total time for the microwave frequency scanning. There is a trade-off between the frequency measurement range and the frequency resolution. If we use IFBW

of 40 kHz, and use sampling points of 16001 for the microwave frequency domain sampling, the frequency resolution is 5 Hz.

5.2.3 Measurement accuracy

The accuracy of the vibration frequency reading equals to the $f_{vib,max}$ divided by the number of points N_0 that used for the transform. As we talked in sec. 2.3.1, N_0 can be much larger than the frequency domain sampling point N through zero padding, so the accuracy of the measured vibration frequency is always much finer than the vibration frequency resolution.

5.3 Experiment and result

The configuration of the system was exactly the same as shown in Fig. 4.2. The description of the figure can be found in section 4.2.1. The filtered FP laser in the configuration was used to demonstrate the idea.

5.3.1 Measurement of vibration frequency

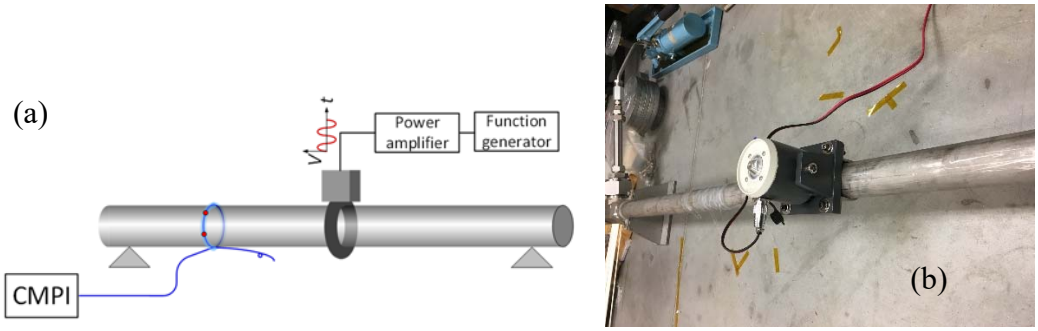

Fig. 5.1 Vibration excitation with a on tube vibration motor with tunable frequency range from 0 to 1k (a) schematic of the setup. (b) Photo of the experimental setup.

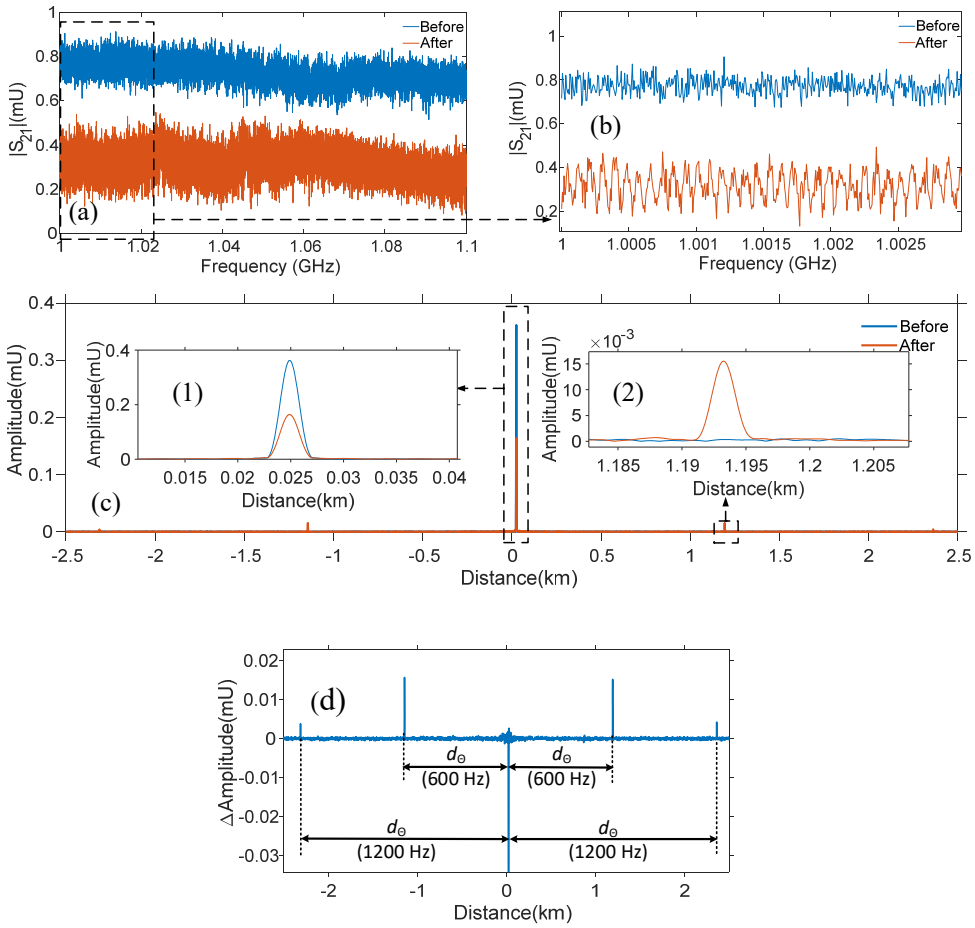

Fig. 5.2 Amplitude of the microwave frequency response of the sensing system before and after turning on the vibrator. The zoomed in amplitude spectrum within the frequency band from 1 GHz – 1.0025 GHz is shown in (b). (c) Amplitude of the time domain signal. Inset (1) the zoomed in amplitude spectrum in the distance range around the location of the reflector pair. Inset (2). (d)Amplitude difference between the time domain signals (before and after turning on the vibrator)

A single pair of reflector with separation of 1cm is fabricated by the fs laser on a piece of 2m long SMF. Each reflector has reflectivity of -30 dB. One end of the SMF was

spliced with the port 2 of the circulator (shown in Fig. 4.2), and the SMF was tightly coiled on a metal tube (diameter = 5cm) and fixed by epoxy as shown in Fig. 5.1. A vibrator was fixed on the metal tube with and driven by a sinusoid electric signal, which is generated by the function generated and amplified by a power amplifier. The vibration frequency can be set from 0 to 2 k Hz, but the amplitude of the vibration decreases as increase the frequency, due to the limited input power.

The VNA was set to have the number of sampling points of 16001 in the microwave band from 1 GHz to 1.1 GHz, and the intermediate frequency bandwidth (IFBW) of 10 kHz. The dwell time for each sampling points was 0.11781 ms, and it took 1.8849 s for VNA to finish one time of frequency band sweep. The amplitude of the frequency response of the system (S_{21}) before and after turning on the vibrator is shown in Fig. 5.2 (a).

The average amplitude dropped after turning on the vibrator, due to the vibration induced DC deformation on the tube. Fig. 5.2 (b) shows the zoomed spectra within the frequency band from 1GHz to 1.003 GHz. It is obviously that, the amplitude changing periodically after tuning on the vibrator. The amplitude of the time domain signals before and after turning on the vibrator is shown in Fig. 5.2 (c). With the microwave bandwidth of 0.1 GHz, the two pulses generated by the two reflectors were inseparable. The reflection happens at the location that about 25-m away from the output port1 of the VNA. A close comparison between the two amplitude time spectra appears that, after turning on the vibrator, the amplitude of the pulse reflected from the reflector pairs dropped, and also, there are four small pulses show up at the location -2287 m, 2387m and -4624m, 4723 m. The four small pulses appear in pairs, and the locations of each two pulses in one pair are

symmetric to the location of the reflector pairs. Fig. 5.2 (a) shows the amplitude difference between the time domain signals before and after turning on the vibrator. The distance d_Θ between the pulse and either side lobe is proportional to the vibration frequency Θ, which can be calculated through

$$\Theta = d_\Theta n / c \cdot \Delta\Omega \cdot \Delta t. \tag{5.12}$$

There are two calculated frequencies, 600 Hz and 1200 Hz. The side lobes at 1200 Hz are probably corresponding to the second order harmonic term of the Taylor expansion of the dynamic term in Eq.(5.4). However, the amplitude of the pulse for the 600 Hz is much larger than the other frequencies.

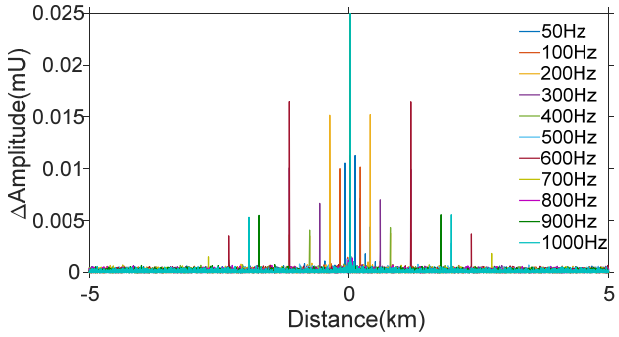

Fig. 5.3 Amplitude difference between the time domain signals before and after turning on the vibrator with difference setting frequency.

Fig. 5.3 shows that as we increased the vibrate frequency from 50 Hz to 1k Hz, the side lobs generated by the vibration moved away from the pulse reflected by the reflector pair. When vibrated the tube with different frequency, the amplitudes of the side lobes were different from pair to pair, due to the mechanical property of the metal tube.

5.3.2 Measurement of vibration intensity

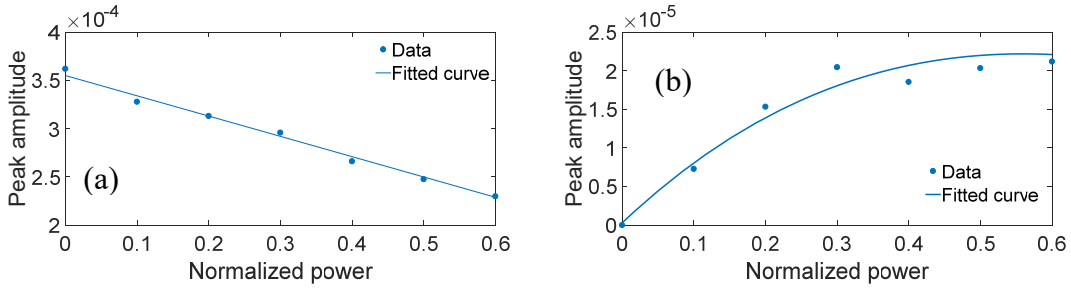

Fig. 5.4(a) Peak amplitude of the main lobe as function of the vibrating power. (b) Peak amplitude of the right-side lobe as function of the vibrating power. The vibrating frequency was 600 Hz.

The vibration frequency was set as 600 Hz. The vibrate intensity was decided by the input power to the vibrator, which can be controlled by changing the output power from the power amplifier. When gradually increasing the input power to the vibrator, both the DC strain and AC strain that applied to the FPI formed by the reflectors increased. The amplitude of the main lope decreases as increasing the vibration intensity as shown in Fig. 5.4 (a), while the amplitude of the side lobe increases as increasing the vibration intensity as shown in Fig. 5.4 (b). The changings are opposite in directions, and the results matches with the prediction in Eq. (5.10), as there is a $\pi/2$ optical phase difference for the two terms related to the amplitude of the main lobe and the side lobe. The vibration intensity can be calculated by using the amplitudes of the main lobe and side lobes, but proper calibration is needed before the calculation.

5.3.3 Multiple vibration locations

This method also has ability to perform multiple location vibration sensing with spatial resolution of 1m (less than 1m is easy to achieve). To validate the concept, we

fabricated four pairs of weak reflectors along a SMF, each pair form a FPI with cavity length of 1cm. The distance between each two adjacent pairs was 1m. The schematic of the system is shown in Fig. 5.5. Two actuators were attached to two FPIs respectively as shown in the inset of Fig. 5.5. The actuators were driven by the sinusoidal changed voltage. The driving signals were provided by two arbitrary waveform generators (AWG, Agilent 33120A) and amplified by a power amplifier. The voltage that was sent to the actuators was round 97 V, and the frequency was set as 1.6 kHz and 2.3 kHz to actuator 1 and 2 respectively.

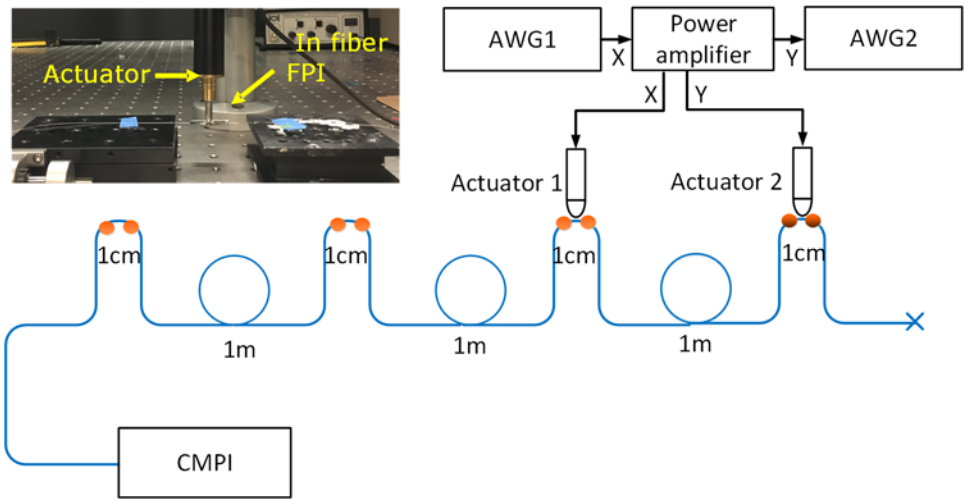

Fig. 5.5 Schematic of experiment setup for the multi-vibrations locations demonstration. Inset: photograph of the set up.

The amplitude (in dB) of the time domain signal before turned on the actuators are shown in Fig. 5.6 (a). There are six pulses shown in the plot, where the one locates around 34 m was the reflection from the terminated end of one lead of the SMF coupler, the second

pulse located at around 43 m was the reflection from the FC to FC adaptor. The rest four pulses formed by the four FPIs were centred at 43.29 m, 44.35m, 45.38 m, 46.41m respectivelyThe VNA was set to have the number of sampling points of 16001 in the microwave band from 200 MHz to 10 GHz, and the IFBW of 15 kHz. The microwave band was large enough to partially separate the two reflections from the 1cm cavity FPI. The dwell time for each sampling points is 0.096 ms, and it took 1.5361 s for VNA to finish one time of frequency band sweep. Firstly, we turned on the Actuator 1 (2.3 k Hz), which was attached to the third reflector pair located at 45.38 m. Fig. 5.6 (b) plots the amplitude of the time domain signal in dB after turned on Actuator 1. The time domain side lobes induced by the vibration appeared in pairs, and were symmetric to the location of the vibration position (45.38 m) with same amplitude as shown in the Figure. Secondly, we turned off the Actuator 1 and turned on the Actuator 2 (1.6 kHz) which was attached to the fourth reflector pair. The amplitude of the time domain signals in dB after turned on Actuator 2 is plotted in Fig. 5.6 (c), where the time domain side lobes induced by the vibration appeared in pairs were symmetric to the location of the fourth reflector pair (46.41m). There are two pair of side lob pairs shows in the Fig. 5.6 (c), as the movement of the actuator exited some other frequency of the mechanical vibrations. The mechanical analyse of the system is out of the scope of this paper, but from the figure we can see that the calculated vibration frequency read from the side lob pair with largest amplitude is 1.601 k Hz. Thirdly, two actuators were excited simultaneously with frequency of 2.3 kHz and 1.6 k Hz. The amplitude of the time domain signals after turning on those two actuators is plotted in dB as shown in Fig. 5.6 (d). The plot is just a superposition of the plots in Figs.

Fig. 5.6 (b) and (c). Since the vibration induced side lob pairs were symmetric to the location where the vibration happens, the location, intensity, and frequency of each vibration can be read from the time domain signal when the vibration happens at multiple locations.

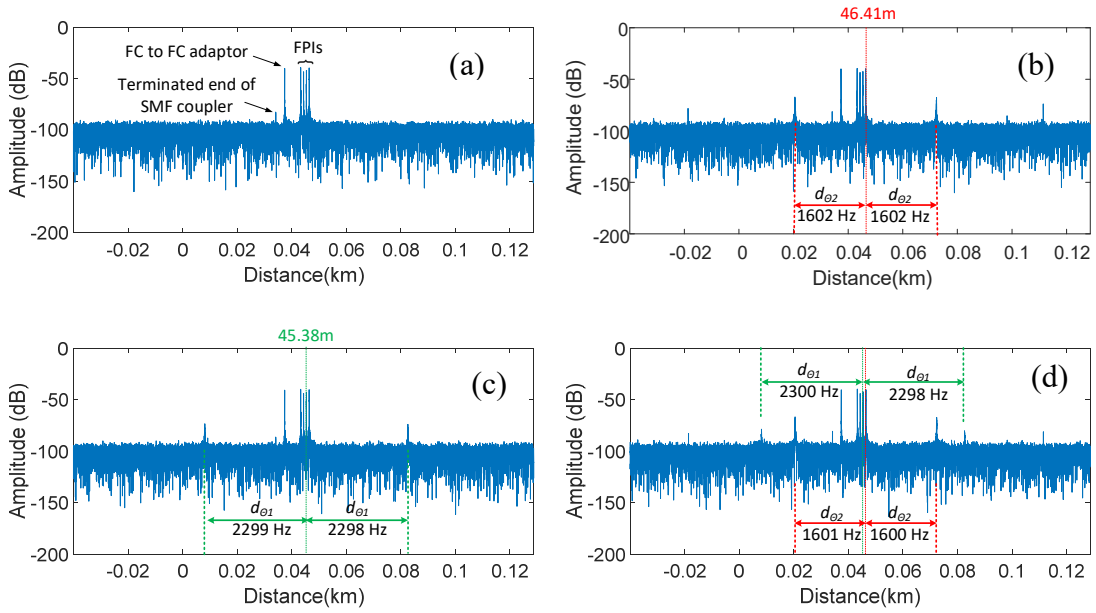

Fig. 5.6 Amplitude of the time domain spectrum (a)before turning on actuators, (b) Actuator 1 was on, (c) Actuator 2 was on, (d) both actuators were on

5.3.4 Pulse response of the system

Besides the long-term vibration measurement, the provided system can also capture the short time vibration, whose vibration time is much smaller than the time for VNA achieve one time of microwave frequency sweep. We used the same setup as shown in 5.1 (a) to demonstrate the idea. Instead of turning on the vibrator, a wrench was used to give a light and fast knock to the tube while the VNA was scanning the microwave

frequency. The VNA was set to have the number of sampling points of 16001 in the microwave band from 1 GHz to 1.1 GHz, and the intermediate frequency bandwidth (IFBW) of 10 kHz. The dwell time for each sampling points is 0.11781 ms, and it took 1.8849 s for VNA to finish one time of frequency band sweep. The amplitude difference of the frequency spectra which were taken before knocking and during knocking is plotted Fig. 5.7(a), and it is shown that the knocking induced an obvious amplitude change. The starting time point when the knocking starts as well as the lasts time of the knocking induced vibration can be read from the frequency domain signal, since there's a linear relationship between each swept frequency point and the time as expressed in Eq. (5.3). The same amplitude can be plotted as function of time as shown in Fig. 5.7(b). The knocking started at around 1.09 s, and there was some strong high frequency vibration generated first, and then the vibration damped out within 0.15s. The knocking also generated some low frequency vibration, which lasted longer. The amplitude of the FFT result of the frequency domain signal (S_{21}) is plotted in Fig. 5.7(c). The vibration location (24.87 m) and vibration frequencies were found through the FFT results. 2944.5 Hz and 30 Hz were the two major frequency components as shown in Fig. 5.7.

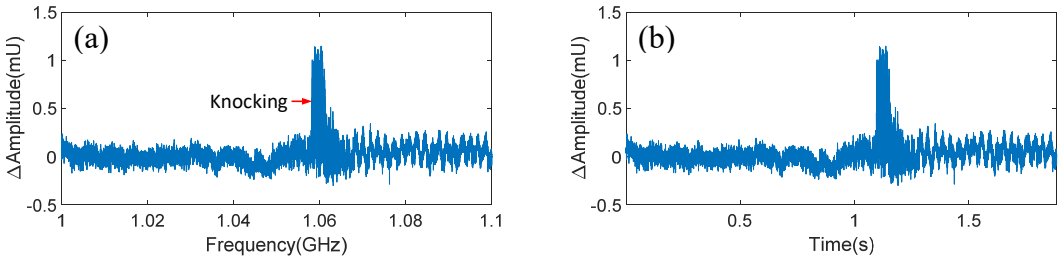

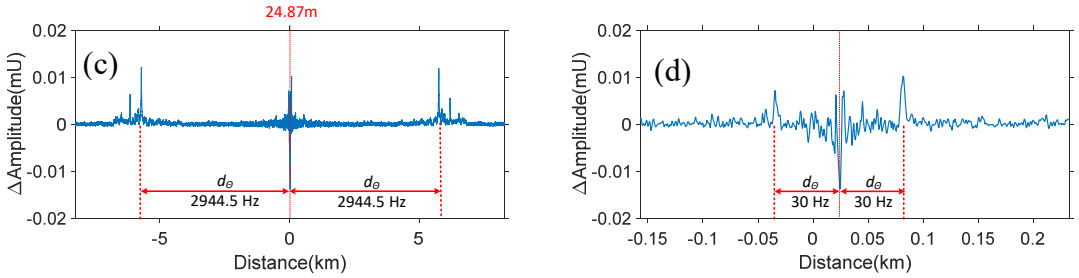

Fig. 5.7 Pulse response of the system. (a)Amplitude of the frequency spectrum. (b)Amplitude of the received signal as function of time. (c)Time domain signal. (d)Zoomed in time domain signal.

The result indicates that the current system has the capability of locating the in impulse vibration in space and reading the respective vibrate frequency. In theory, the impulse vibration with time width larger than the dwelling time can be detected through this system. If there are several cascaded FPIs, we can read the microwave frequency signal change induced by each single FPI in the sequence of time. This distributed impulse vibration measurement capability can be helpful for characterizing the pressure wave in terms of propagate direction, velocity, amplitude, and the attenuation during the propagation.

CHAPTER SIX

NOISE AND DETECTION LIMIT

Like all the area of measurement, the ultimate limit to the detectability of small changes of the signal is set by noise which obscure the desired signal. Various noises contribute to the total noise and limit the performance of the microwave photonics sensing systems. In this chapter, we focus on examining the main noise sources in both the proposed OCMI and CMPI systems, and find the detection limit of both systems.

6.1 Noise from light source

6.1.1 Relative intensity noise

Relative intensity noise (RIN) is the power noise normalized to the average power level. The optical power of the laser can be expressed as the sum of an average value $\bar{P}$ and a fluctuation quantity $\delta P(t)$ with zero mean value. The relative intensity noise is then the ratio between $\delta P(t)$ and $\bar{P}$. The relative intensity noise can be statistically described with a power spectral density [80],

$$S(f) = \frac{2}{\bar{P}^2} \int_{-\infty}^{\infty} \left\langle \delta P(t) \delta P(t+\tau) \right\rangle \exp(i 2\pi f \tau) d\tau, \tag{6.1}$$

which depends on the noise frequency *f*. The unit of the RIN power spectrum density (PSD) is Hz-1 or dB/Hz. When RIN is limited by the shot noise, the PSD of it becomes independent to the noise frequency, and it increases with decreasing average power.

The RIN of light sources we are using are all around -155 dB/Hz, which is very small compare with other noise, so we can neglect the RIN for when perform the each short time microwave frequency band sweep. However, there's also long-term power stability issue. OCMI based on the spectrum shift measurement, and the power difference between two times of measurement would not affect the sensing signal reading. CMPI based on the power measurement, the power change between two measurements will induce the sensing signal reading error, and decrease the sensitivity of the sensors. Setting single reflector to get the power level is one way to decrease the affect caused by the power fluctuation.

6.1.2 Phase noise

The output of a single-frequency laser is not perfectly monochromatic but rather exhibits some phase noise. This leads to a finite linewidth of the laser output. The fundamental origin of phase noise is quantum noise, spontaneous emission of the gain medium into the resonator modes, but also quantum noise associated with optical losses. In addition, there can be technical noise influences, e.g. due to vibrations of the cavity mirrors or to temperature fluctuations. In many cases, there is also a coupling of intensity noise to phase noise [81]. Phase noise may occur in the form of a continuous frequency drift, or as sudden phase jumps, or as a combination of both. The influence of phase noise to the CMPI is significant, slow center frequency drifting affects the optical interference power and reduce the sensitivity of the sensors.

6.1.3 Beat noise and spectrum influence

There is a beating process among the different optical frequency components results in appearance of several components that can be classified as the beat noise

component [82]. As shown in Eq. (2.5) the beat noise increase with increasing of the bandwidth of the light source. The relationship between the spectrum of the optical light carrier and the noise level has been investigated. Three different types of light source, ASE with bandwidth of 30 nm, Fabry Perot (FP) laser (comb shape spectrum with total line width smaller than 1nm), and 0.1 pm distributed feedback (DBF) laser, have been used in the following experiment. All of those light sources have been modulated by the EOM, and the power at the detector are

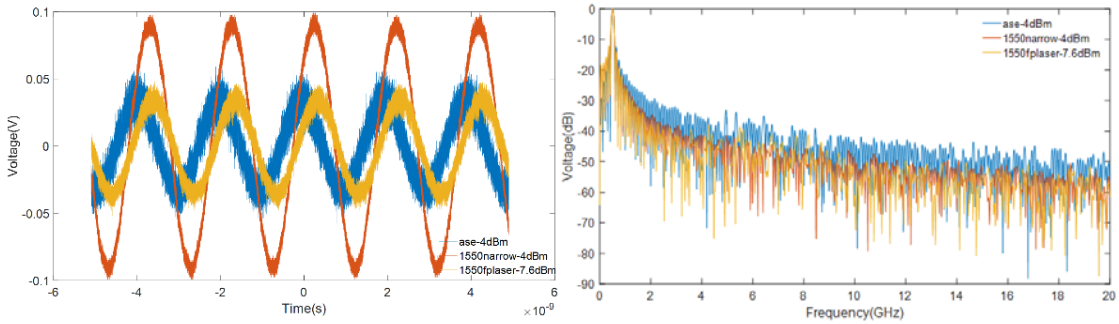

Fig. 6.1(a)Time domain signal and (b)Fourier transfer result of the signal got by using different light source

-4 dBm by using the ASE and the DBF laser, while the experiment with using FP laser has the input power at detector of -7.6 dBm. The ASE has the random SOP, while both lasers emits the linear polarized (LP) wave. Since EOM is polarization sensitive, and the LP light can reach the highest modulation depth. The time domain signal received by oscilloscope for both three cases are shown in Fig. 6.1(a). The peak to valley value is the same for using FP laser and ASE, which indicates that the modulation depth is higher when use the FP laser as light source. When use the light from DFB laser as the optical carrier, the peak to

valley value of the microwave signal is two times of that of the other two cases, which indicates that the modulation depths are not far off by using both lasers. There is 3-dB peak to valley difference between the DFB laser and the ASE light source because of the average effect on the modulation depth of all the wavelength light from ASE. Fig. 6.1 (b) shows the normalized Fourier transform result of the respective time domain signal. As we can see that the white noise level for the ASE light source is 5 dB higher than the other two signals, due to the beat among the optical frequencies [83,84].

The above experiments give us a clear picture that the narrower the linewidth of the optical carrier the higher modulation depth can reach, the lower white noise level we can have. However, VNA has the narrow bandpass filter which centers at the target frequency, and can dramatically reduce noise. The VNA demonstrates a better SNR by the factor of f_c/IFBW, where f_c is the cutoff frequency [85]. When design the OCMI type sensor, we need to make sure that the optical difference between two different paths is larger than the coherent length of the optical light to exclude the interfering caused by the optical interference. Therefore, there's a tradeoff between the sensitivity of each sensor and the spatial resolution of the OCMI distributed sensing system. For the CMPI type sensor, narrow band laser is used to get the optic inference information between two reflectors, so the noise power from this part for CMPI system is lower than that for OCMI system.

6.2 Noise from EDFA

The noise power at the output of our ideal amplifier, measured in a certain bandwidth, is not only the input noise times the amplifier gain (power amplification factor), but significantly higher due to added excess noise [86].

A laser amplifier, working with stimulated emission of radiation, can come close to such an ideal amplifier if it uses a pure four-level laser transition and has no parasitic power losses, e.g. from absorbing impurities or light scattering [87]. Its excess noise can be interpreted as resulting from unavoidable spontaneous emission into the amplified mode. The noise figure NF is measure of how much noise the amplifier adds to the signal. The NF of EDFA can be written as:

$$NF = [1 + 2P_{ASE} / (\mathrm{h}\nu\Delta\nu_{sp})] / G \ , \tag{6.2}$$

where P_{ASE} is the amplified spontaneous emission (ASE) power from the EDFA over the measure spectrum band $\Delta\nu_{sp}$, h is the Planck constant, ν is the corresponding frequency of the signal, G is the gain of the EDFA. The smallest possible NF is 2 (3 dB) due to quantum noise [88].

Excessive ASE leads the increasing of shot noise at the detector, and thus increased the minimum detectable signal level. The ASE of amplifier also produce beat noise which happens between the ASE and the signal electric fields [82]. For the CMPI system, narrow band light source is used. The optical bandpass filter of smaller than 1 nm can be used to transmits the useful signal while rejecting most of the ASE. However, for OCMI system, board band light is needed to eliminate the optical interference and stable the signal, adding band pass filter is a less effective method as larger filter bandwidth is required.

6.3 Noise from photodetector

6.3.1 Shot noise

Shot noise results from the discrete electronic charge of electrons or other carriers as they pass across a potential barrier. Be specifically, photons that generate electron-hole pairs in a PIN photodiode produce a photon current which has random fluctuation about its mean value. The shot noise is proportional to the received power and is assumed to be white noise. In both OCMI and CMPI systems, PIN detectors have been used and the noise power can be expressed as,

$$\sigma_{q,PIN}^2 = 2qI_p\Omega_B R_L \tag{6.3}$$

where q is the electric charge, I_P is the average photocurrent, Ω_B is the frequency bandwidth, R_L is the resistance of the load resistor [82]. A roughly calculation shows that, for an input lightwave signal with 10 mW power and 10 GHz receiving bandwidth, with load resistance of 50 Ω, the shot noise that created by the PIN detector (with responsivity of 0.8A/W) is 1.3 nW(-58.9279 dBm).

6.3.2 Dark current noise

Dark current is the relatively small electric current that flows through photosensitive devices even when no photons are entering the device; it consists of the charges generated in the detector when no outside radiation is entering the detector [82]. It is referred to as reverse bias leakage current in non-optical devices and is present in all diodes. Physically, dark current is due to the random generation of electrons and holes within the depletion region of the device. The noise power that induced by the dark current (I_L) is expressed as

$$\sigma_{DB,PIN}^2 = 2qI_L\Omega_B R_L \ . \tag{6.4}$$

The dark current noise is even much smaller than shot noise.

6.3.3 Thermal noise

Thermal is the electronic noise generated by the thermal agitation of the charge carriers (usually the electrons) inside an electrical conductor at equilibrium, which happens regardless of any applied voltage. Thermal noise is approximately white noise. The power spectral density is nearly constant throughout the frequency spectrum. Thermal noise for the photodiode itself is usually neglected, because the parasitic shunt resistance associated with a reverse-biased PN junction is very large. Thermal noise of the subsequent amplification stages particularly the first stage of amplification or transimpedance amplifier can be important for low input light levels.

$$\sigma_T^2 = 4k_b T\Omega_B \tag{6.5}$$

where k_b is the Boltzmann's constant in J/K, T is the absolute temperature [82]. For a 10 GHz bandwidth receiver, at room temperature (300 K) the calculated thermal noise is 0.166 nW(-67 dBm), which is several times smaller than the shot noise under same condition. The thermal noise is dominating when the input light signal is power is smaller than 1.3 mW.

6.1.1 Total noise

The total noise produced by the detector is the sum of shot noise, dark current noise, and the thermal noise. It is approximately equals to the thermal noise, when the input optical power is small. The minimum detectable power—the optical power that is

necessary to produce a photocurrent of the same magnitude as the total noise current (SNR=1), which can be calculated as

$$P_{\min} = \sqrt{\sigma_T^{\,2} / R_L} / r \ , \tag{6.6}$$

where r is the responsivity. With r = 0.8 W/A, R_L =50 Ω, the minimum detectable signal power is about 2.27μW/10G$\sqrt{Hz}$. (-26.43 dBm//10G$\sqrt{Hz}$) in room temperature (300K). High responsivity, and large load results in lower minimum detectable signal. As we can see that the noise power is bandwidth dependent, the noise level decrease with the decreasing of bandwidth. Therefore, the minimum detectable power is often referred to as noise equivalent power (NPE) and has the units of W/$\sqrt{Hz}$. The OCMI and CMPI systems using VNA as the electric signal receiver which use a narrow bandwidth filter, so the minimum detectable power for those systems can be much smaller than above calculated results. We will talk about this in the following sections.

6.3.4 Phase to intensity noise

Phase to intensity noise is shown as the second term in Eq. (4.2). It comes from the cross product $\langle I_{cross}(\Omega, t) \rangle$, and basically, it shows the optical interference among the target reflected signal and all the other reflected signal in the sensing system. The phase to intensity noise is a function of the modulation frequency and it changes dramatically as the spectrum of the optic carrier change and optical phase change among the reflections in the sensing system. In OCMI system, wideband light source has been used, the influence of the phase to intensity is small. In CMPI system, the phase to intensity noise composes by the optical interference between the reflected light from the target reflector and the

Rayleigh scatters fell within the coherence length range. The CMPI relies on the power detection, so the phase to intensity noise level directly decided the minimum signal change that the system can read. Normally, we fabricate the reflector with reflectivity of -30 dB, and the Rayleigh scattering level is about -82 dB for 1 ns pulse at the wavelength around 1550 nm. Thus, limited by the phase to intensity noise, the minimum intensity change that can be read regardless of other noise in the system is about 10^{-4} of the amplitude of the time domain peak.

6.4 Detection limit

6.4.1 Noise power received by VNA

For the small signal detection, the most dominant noise in those two sensing systems are phase-to-intensity noise and thermal noise [89,90]. Since initial filtering is used at the intermediate frequency stage which helps to keep a large share of the received broadband noise out of the single processing chain of this microwave photonics sensing system, only the spectral noise power around the modulation frequency is the SNR-determining value. The phase-to-intensity noise is frequency dependent which decided by the structure of the fiber sensor system and the, so it is hard to setup general model to describe it. Thermal noise exhibit approximately white noise characteristics, which means that the power spectral density is approximately constant throughout the frequency spectrum. The thermal noise superimposed on the measured values involves random measurement uncertainty. As we talked before, at room temperature (300K), the noise power density of thermal noise is about -67 dBm/10GHz. If we use an ideal rectangular filter with a 1 Hz bandwidth, the VNA would not produce any internal noise, a noise level

-177 dBm would be superposed on the measured signal. However, the IF filter that has been used in the VNA does not have a rectangular transmission characteristic, and it have an approximately Gaussian transmission characteristic with a shape that is identical for all of the filters and which is scaled only in terms of the bandwidth. The noise bandwidth of the IF filter is always greater than 3 dB bandwidth which has been used to characterize the filter setting. The ratio of the two bandwidths (real and 3dB Gaussian) yields the shape factor S_F>1. Also, the displayed noise level is increased by the noise figure (NF) of the instrument. Accordingly, the noise level L_N can be calculated accordingly.

$$L_N = -177\,\text{dBm} + NF + 10\log_{10}(\text{S}_F)\,\text{dB} + 10\log_{10}(\text{IFBW/ Hz})\,\text{dB}. \tag{6.7}$$

The noise level increases by 20 dB, if the IF bandwidth increases by a factor of 100. Unfortunately, any change in the IF bandwidth also influences the sweep time. For small IF bandwidth, these two quantities are inversely proportional. Double the IF bandwidth cuts the sweep time in half [37].

6.4.2 Rayleigh scattering

In amorphous materials such as silica glass, there are always random density fluctuations due to the irregular microscopic structure. These are even substantially stronger than they would normally be at room temperature, because during fiber fabrication, the density fluctuation which occurred for the fiber near the glass softening temperature are “frozen in”. The Rayleigh scattering sets a lower limit to the propagation losses in optical fibers. Most of the Rayleigh scattered light in a fiber exits the fiber on the side. Only a small portion of the scattered light is scattered back such that it is again guided

in the fiber core. Therefore, detecting the Rayleigh scatting becomes challenging and address high requirement on the sensitivity of the detecting system.

We used the setup as shown in Fig. 6.2(a) to measured reflection spectrum of the Rayleigh scattering in the SMF, after Fourier transform we got the time of arrival information of the scattering. the scatted power level is plotted as function of time shown in Fig. 6.2 (b). The laser we used was a directly modulated laser, which has linewidth of about 20 MHz, centered at 1543 nm. The output laser power was about 5 dBm, and after EDFA, the light power was about 13 dBm. The swept microwave frequency was set as 200 MHz to 300 MHz, the IFBW was set as 1kHz, the microwave power from amplifier was about 15 dBm. The light launched into a 4.5 km single mode fiber roll through a circulator, and then the Rayleigh scattering has been reflected to the circulator and amplified by EDFA 2. An optical bandpass filter placed in front of photo detector to suppress the ASE and decrease the shot noise from the photodetector. The optical power that input into the photo detector was about -10 dBm. The Rayleigh scattering was eventually received by the photodetector in the sequence of time. Fig. 6.2 (b) shows the Rayleigh scattering signal got from this system. The high peak located at around 9 km, is the reflection from the terminated fiber end. The comparison between the signal level before and after the fiber end shows that the scattering is 34 dB higher than the noise level. After smoothing the scatting spectrum over every 124 m, we can clearly see the fiber loss slope in Fig. 6.2 (c). The linear fitting results show that the slope of the loss line is about -0.37146 dB/km. As the scattered light travelled double ways to reach the photodetector, the loss of the fiber at

wavelength of 1543 nm is half of the measure value, which is -0.185 dB/ km as shown in Fig. 6.2 (d).

The Rayleigh scattering power level should be accumulated within time period. The provided microwave photonics system use the frequency measurement, so the time period for the power accumulating is inversely proportional to the width of the swept microwave band. In this experiment, the with is 0.1 GHz, which is corresponding to 10 ns period.

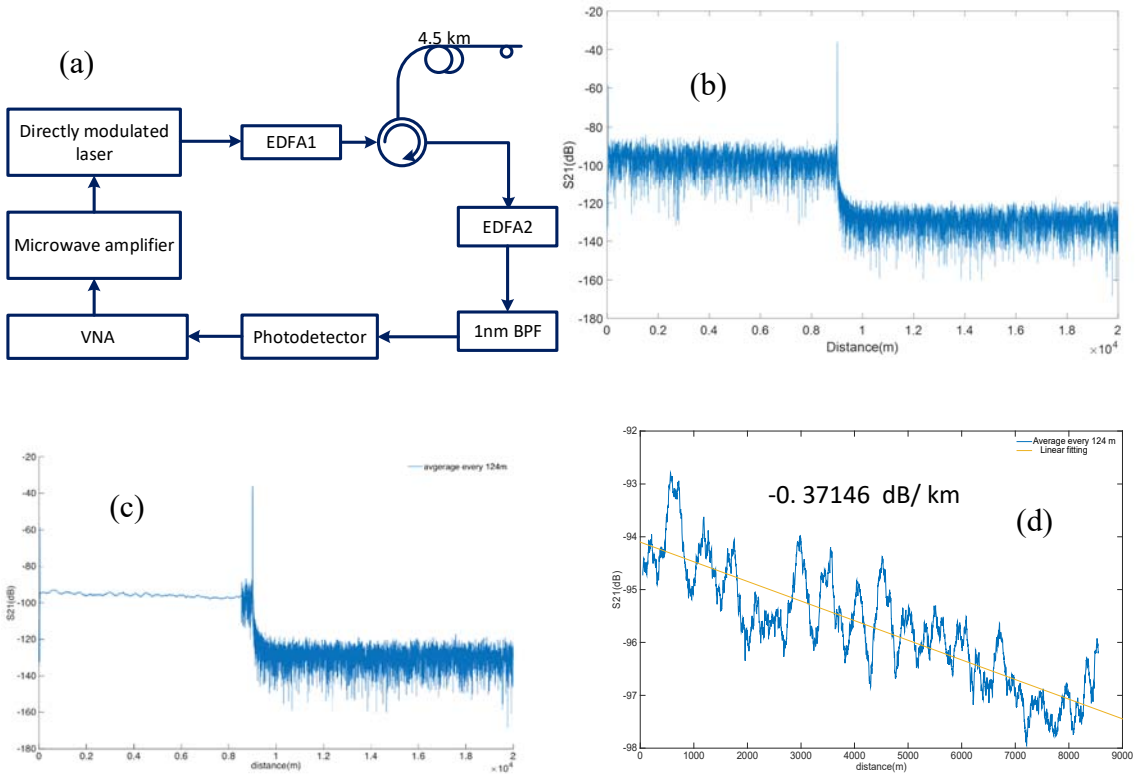

Fig. 6.2 Schematic of the system using for the Rayleigh scattering measurement, (b) Rayleigh scatting, (c) Space average on the Rayleigh scattering signal (smooth), and (d) linear fitting based on the smoothed curve.

Assume the Rayleigh scattering coefficient is -82 dB at wavelength around 1550 nm for 1ns width [91]. Then for the 10 ns width pulse, it should be -72 dB. The noise level shown in Fig. 6.2 (b) is 34 dB lower than the signal level in the beginning, which indicates that based on the current configuration the minimum detectable reflection can be as low as -89 dB (As VNA records the voltage ration, there is a 2 factor when calculate the reflectivity in the optical link). Further improvement can be done by improving the responsivity of the photodetector or decrease the IFBW.

CHAPTER SEVEN

CONCLUSTION AND FUTURE WORK

7.1 Conclusion

This dissertation work includes the studies on demonstration the static and dynamic distributed sensing base on the microwave photonics links. In this work, the concepts of OCMI and CMPI by using the incoherent light and coherent light respectively were studies. Both the mathematical modeling and experiments were carried up to explore the capability, potential, and limitations of the sensing systems that build up based on OCMI and CMPI.

The OCMI is a technology that uses incoherent light as optical carrier and reads the sensing information by tracking the spectral shift of the microwave interferogram. In OCMI distributed sensing system, the sensors are FPIs formed by any two adjacent in fiber reflectors with the OPD much larger than the coherence length of the light source, and as a results, the optical interference including the mode interference in MMF have little influent on the OCMI signal. Thus, multimode optical waveguides fabricated sensors can be fit into the OCMI systems to produce high quality microwave interferogram. The sensing systems developed based on the OCMI by planting sensors fabricated by different types of multimode waveguides (large core silica fiber, POM, etc.) for distributed large strain and high temperature measurement have been built up and investigated firstly in this dissertation.

However, OCMI only reads the interference in microwave domain. As such the sensing resolution was low (in tens of με, limited by the intermedia frequency of the microwave source. Driven by the interest on the high sensing resolution, we proposed the

CMPI, which uses a coherent light source to obtain the optical interference signal from the cascaded weak reflectors for much improved sensitivity. In addition, the coherence length of the light source is carefully chosen or controlled to gate the signal so that distributed sensing can be achieved. To demonstrate the concept, cascaded fiber Fabry-Perot interferometers were fabricated in a SMF using femtosecond laser micromachining. Our modeling and analysis provided the relation between the time-domain pulse amplitude and the OPD of the cascaded interferometers. By carefully select the separation distances among the cascaded reflectors, the coherence length can gate the signal so that only two adjacent reflectors participate in the optical interference and ambiguity can be avoided to achieve distributed sensing. The experimental results indicated that the strain measurement resolution can be better than 0.6 με using a FPI with a cavity length of 1.5 cm. Further improvement of the strain resolution to the nε level is achievable by increasing the cavity length of the FPI to over 1m. However, the theoretical analyses and experimental results showed that the signal was a sinusoidal function of the OPD. As a result, the sensitivity is nonlinear and there is a tradeoff between the sensitivity and dynamic range due to the 2π ambiguity. A longer cavity length will result in a higher resolution but smaller dynamic range. Knowing this tradeoff allows the strategy and flexibility to design a distributed sensing system to satisfy the different sensitivity and dynamic range needs at different locations in a specific application. To minimize the optical power instability (either from the light source or the fiber loss) induced errors, a single reflector can be added in front of an individual FPI as an optical power reference for the purpose of compensation. The theoretical analyses and experimental results all showed that CMPI could have a great

potential for distributed sensing, especially for its high sensitivity, though many aspects of the concept still remain for further research.

We demonstrated that CMPI could be also utilized for the distributed dynamic measurement. CMPI based on the power measurement, and the small OPD change at any location along the sensing system within a small-time frame would immediately show as the amplitude change for the respective scanned microwave frequency band within that time frame. When the vibration induced periodically changed strain happens between two adjacent reflectors within the time of one microwave frequency scan, the vibration location, intensity and frequency can be retrieved from the time domain signal. It was shown that the provided system can support the multi-points distributed vibration measurement with the maximum vibration frequency of up to 20.832 kHz.

Besides of building distributed sensing systems with the high performance in respect to high sensitivity, high spatial resolution, long measurement range, fast response for dynamic measurement, etc, moreover, the research in this dissertation established a distributed sensing platform which can provide a suite of solutions to meet the requirements for varieties of sensing applications. The controllable sensing performance is achieved by but not limited to 1. carefully choosing the spectrum of the light carrier, 2. adjusting the band and the IFBW of the modulation RF signal, 3. selecting the material and geometry of the optical fiber that used for fabricating sensors, and 4. the separation between the in fiber reflectors.

7.2 Innovations and contributions

The major scientific and technical merits of this work include:

1. The performance and sensing limitations of the OCMI has been theoretically analyzed and experimentally demonstrated. The noise contribution from each part of the system was analyzed. The sensing applications by using OCMI were explored.
2. A Michelson type OCMI was fabricated by using two pieces of fused silica fiber with core diameter of 200 μm. The strain sensing capability in high temperature environment was experimentally demonstrated.
3. Distributed large strain sensing through OCMI system by using grade index multimode polymer fiber was demonstrated. The in fiber reflectors were fabricated by precisely controlled knife cutting, and the distributed reflected signal from each reflector were monitor during fabrication. The sensor showed linear response to the applied strain, and it survived under the applied strain of as large as 27 mε.
4. The concept of CMPI was proposed for the purpose of high sensing resolution. The mathematical model for CMPI was built. Experimental results show that the sensing resolution of CMPI is at least ten times higher than that of the incoherent type distributed sensing technologies (e.g. OTDR, BOTDR, OCMI), and is comparable to that of OFDR. However, the measurement range of CMPI is up to tens of kilometers, which is much larger than that of the traditional OFDR. The strain sensitivity of phase-OTDR can be as high as 10 nε, but it's challenging for phase-OTDR to quantitatively evaluate the sensing results. The experimental results indicated that the strain measurement resolution can be better than 0.6 με using a FPI with a cavity length of 1.5 cm. Further improvement of the strain

resolution to the nε level is achievable by increasing the cavity length of the FPI to over 1m.

5. CMPI for dynamic measurement was firstly proposed and demonstrated. The mathematical model for the dynamic CMPI was explored. Experimental results show that the proposed method can measure the multi-points weak vibration with frequency up to 20.832 kHz and measurement range up to tens of kilometres. The vibration frequency, location, as well as the intensity can be read by using this method. Dynamic CMPI inherits all the advantages from CMPI, so the sensitivity and measurement range can compete with most of the current sensing technologies. The obtained results imply that the proposed dynamic CMPI can be implemented for many kinds of applications such as geophysical parameter monitoring during infusion.

7.3 Future works

7.3.1 Characterization of pressure wave propagation

CMPI has high sensing resolution, and it has been demonstrated for the distributed dynamic sensing capability by measuring the distributed vibration. However, there are some sensing applications that requires dynamic information which is quite beyond the vibration intensity and frequency. One example of the applications will be characterizing the propagation of the pressure wave, such as measuring the velocity and amplitude and the attenuation of the pressure wave, which can be further extended to detect the seismic waves from an earthquake.

Here is one of the possible way to measure the pressure wave. In this experiment, the pressure wave was provided by the oil pump as shown in Fig. 7.1. Two cascaded in fiber FPIs were used for the measurement. The FPIs were on a same SMF and separated by about 2.3 km and have cavity length of 1 cm and 30 cm respectively. The two FPIs have tightly coiled on a metal tube (diameter = 5cm) and fixed by epoxy. The tube was 2m long, and the distance between the fixing location of the two FPIs along the tube was about 1.5 m. The signal was interrogated by using the setup as shown in Fig. 4.2. One end of the SMF was spliced with the port 2 of the circulator shown in Fig. 4.2. A DFB laser with centre wave length of 1550 nm, and bandwidth of 10 MHz is used as light carrier. The microwave frequency was set from 1.1 G to 1.11GHz with sampling point number of 16001, and the IFBW was set as 40 k. The sweep time over the frequency band was 384.024 ms, so the dwelling time for each frequency point was 0.024 ms.

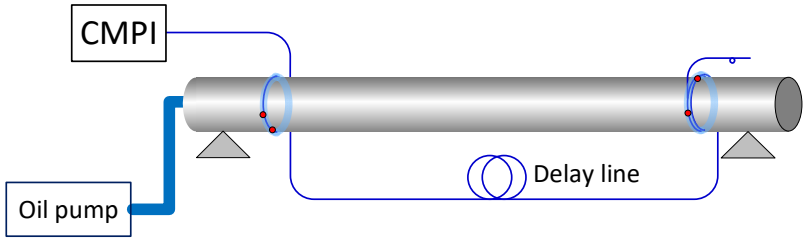

Fig. 7.1Schematic of the setup for pressure wave measurement

The statistic pressure measuring was performed first by using CMPI technology.

The time domain signal before applying any pressure is shown in Fig. 7.2(a). The pulse formed by the FPI 1 with cavity length of 1cm was used for signal processing. Fig. 7.2(b) shows the peak amplitude (real part) as function of pressure. It took about 500 psi

to produce one period of the real part change for the first pulse. It is calculated that for 1cm long cavity, it took about 77 με to produce one period of the peak real part change with the same optical carrier wavelength. Thus, 1 psi creates 0.15 με to the fiber coiled on it by expanding the tube.

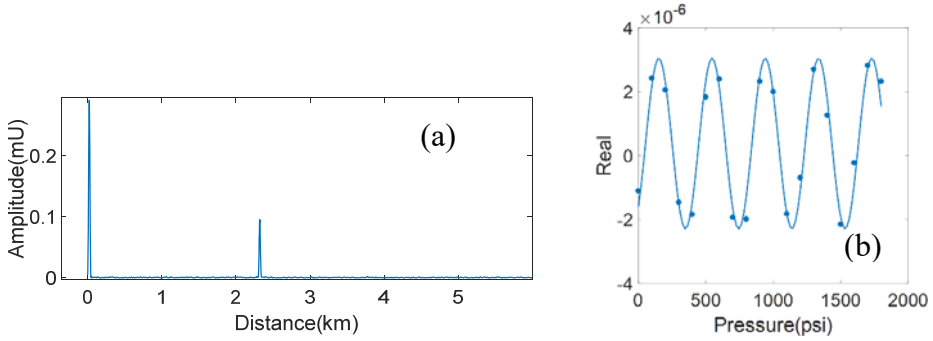

Fig. 7.2 (a) Amplitude of the time domain signal for the two cascaded FPIs sensor. (b) Real value of the first peak as function of the applied pressure.

The pulse wave was created by slightly tap the oil pump. One end of metal tube that located closer to the oil pump should have deformation first, and then the other end. Fig. 7.3(a) shows the difference between the amplitude of the frequency domain signals before ($S_{21before}$) and during taping ($S_{21tapping}$) the oil pump. The slightly tap caused signal change lasted for about 90 ms, and the place on the tube where we placed the first pair of FPI1 (1cm) experienced the deformation caused by the pressure change first, and then the place where we placed the second FPI2 (30 cm) experienced the deformation. As a result, the frequency domain signal change should be only caused by the OPD change of FPI 1 in the beginning, and then caused by the OPD change of both FPIs. The time delay between

the start time point of FPI 1 solo working zoom and two FPIs multi working zoom was decided by the propagation velocity of the pressure wave inside of the tube.

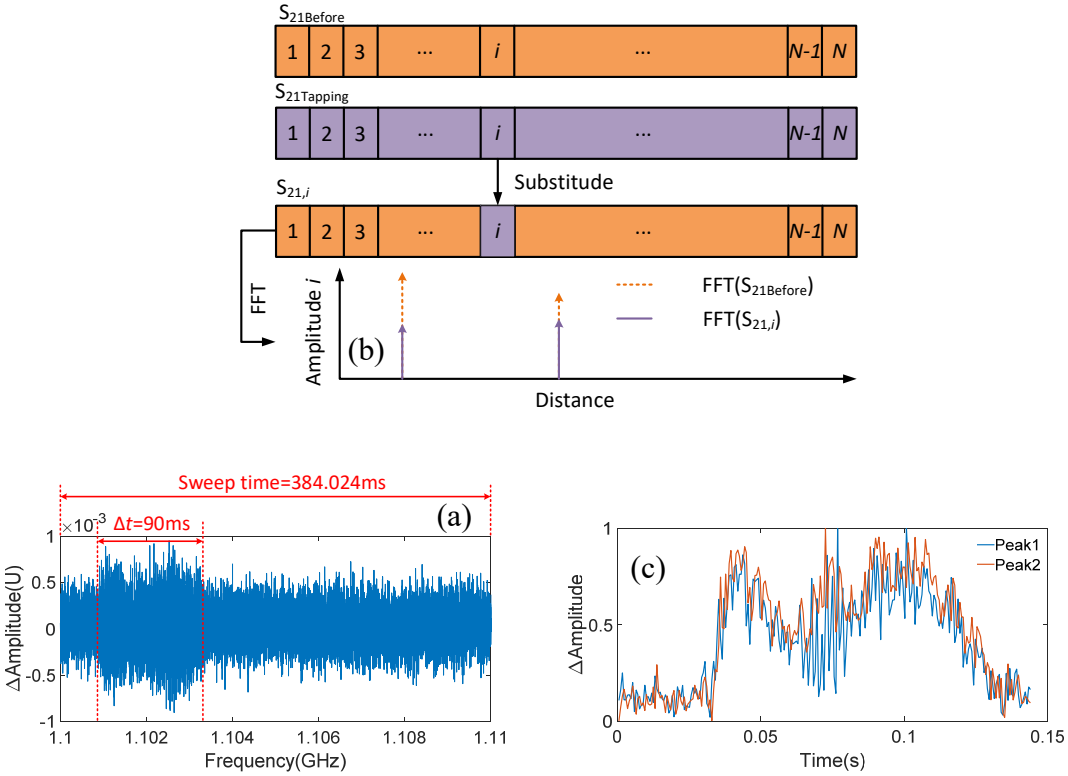

Fig. 7.3 (a) Amplitude difference between the frequency spectra before and during tapping. (b) Signal processing method for reconstruct time (space) domain signal for each time frame. (c)Time pulse amplitude change at each time frame for two peaks.

Fig. 7.3(b) illustrate one way to find the time delay. Firstly, slice the two frequency domain signals ($S_{21before}$ and $S_{21tapping}$) into N equal width adjacent narrow bands. Secondly, substitute the ith (i =1,2,3, …N) sliced band of $S_{21tapping}$ into $S_{21before}$. Each new frequency domain signal is called $S_{21,i}$. Perform FFT for each $S_{21,i}$ to get the time (distance) domain signal at each time frame i, and record the amplitudes of the two time pulse peaks. The

width of the sliced band decides the time resolution and pressure sensitivity of the system. The wider the sliced band is, the lower time resolution the algorithm provides, but consequently higher the pressure sensitivity the system can have, since the amplitude change within the substitute band is averaged by all the frequency component within the swept frequency band after FFT, and the amplitude change of the time domain signal is small if the ratio of the bandwidth of the substitute narrow band to the overall band is small. On the other hand, the amplitude change will be much more dramatic, if the ratio is large. For a better sensitivity, we could truncate the frequency band to smaller band where the pulse wave shows up, and do the signal processing explained above.

In this experiment, firstly, we truncated the amplitude spectrum to the frequency band from 1.1G to 1.1038G Hz. The width of the sliced band was set as 15.625 kHz (25 frequency points), and it took 0.6 ms for VNA to finish the sliced band scan. After that, the amplitude of the two pulse peaks can be plotted as function of the time frame i, as shown in 7.4 (b). The delay between the two pulses should equal to the time of the pressure wave travels from IFPI 1 to IFPI 2.

7.3.2 CMPI with phase modulation

The intensity modulation encodes the microwave information as variations in the instantaneous intensity change of the carrier, and it has been used in both OCMI and CMPI in this dissertation work. The interferogram formed by the interference among the envelopes of the reflected intensity modulated light can provide us the location information for each reflector in the sensing system, so it is one of the most important part in those two types of sensing systems. However, as we look into the time domain signal of CMPI as

shown in Eq. (4.7), it contains two parts. The first part is a constant which is the product of the interference of the microwave envelope. This constant is essential when it comes to measurement by using OCMI type sensing system. However, for CMPI type of sensing system, the sensing information is only provided by the second term which is the product of the optical interference, and there will be many benefits such as decreasing the noise level, if one can eliminate the constant from the sensing signal.

Phase modulation is another modulation pattern that encodes information as variations in the instantaneous phase of a carrier wave. When we put it in the CMPI system, the signal out from the new configuration will only provide the optical interference related term. The phase modulated lightwave reflected by the *i*th reflector can be expressed as

$$E_i = A_i J_0(\alpha) e^{j(\omega t - \phi_i)} + A_i J_1(\alpha) e^{j\left[(\omega-\Omega)t - \Phi_i - \phi_i\right]} - A_i J_1(\alpha) e^{j\left[(\omega+\Omega)t + \Phi_i - \phi_i\right]} \tag{7.1}$$

Assume the modulated light has been reflected by two in fiber weak reflectors with the separation much smaller than the coherence length between then. Thus, the complex frequency response S_{21} of the system, i.e., complex reflectivity normalized with respect to the input signal, is (All the deductions follow the steps from Eq. (2.5) to (2.8)and from Eq. (4.1) to (4.2)

$$S_{21}(\Omega) = A_1 A_2 J_0(\alpha) J_1(\alpha) 2i \sin \Delta\phi \left(-e^{-j\frac{\Omega z_1}{c}} + e^{-j\frac{\Omega z_2}{c}} \right) \tag{7.2}$$

Where z_1 and z_2 are the optical distances that from the two reflectors to the microwave input port on the phase modulator. The time domain signal after Fourier transform is expressed as

$$F(t) = A_1 A_2 J_0(\alpha) J_1(\alpha) 2i \sin \Delta\phi \cdot \sum_{i=1}^{2} \delta(t - \frac{z_i}{c}) \tag{7.3}$$

The signal contains two time domain pulses, and the amplitude of each pulse is directly decided by the optical phase difference between the two reflected optical wave.

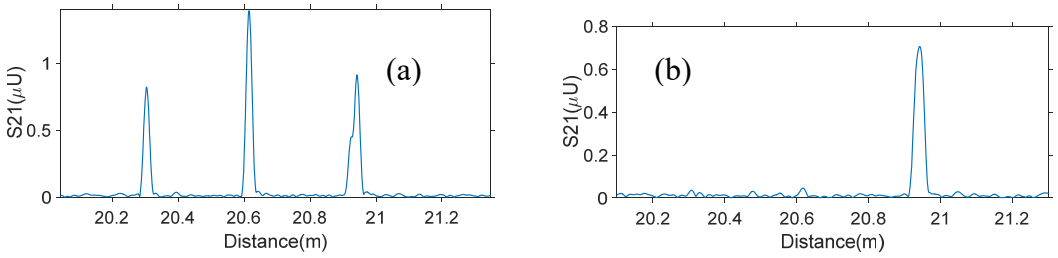

Fig. 7.4 Time domain signal by using (a)Intensity modulation (b) phase modulation

A quick experimental revealed the time domain signal difference between the intensity modulation and phase modulation. The configuration of the system was exactly the same as shown in Fig. 4.2. Microwave band was set from 200 MHz to 10 GHz. The filtered FP laser with coherence length about 6 cm in the configuration was used to demonstrate the idea. Four inline weak reflected reflectors with separation of 30 cm, 30 cm, and 1 cm between any two adjacent ones were used. Intensity modulation EOM was used first and the amplitude of the time domain signal is shown in Fig. 7.4(a), where three time peaks corresponding to the reflection from the four reflectors shows up (The peaks with separation of 1cm merged together). Next, we substituted the intensity modulator into a phase modulator. Fig. 7.4(b) shows the amplitude spectrum of the time domain signal after substitution. As we expected, only the reflectors with separation of 1cm appeared in that spectrum as a strong high contrast pulse.

REFERENCE

1. A. Minardo, G. Persichetti, G. Testa, L. Zeni, and R. Bernini, "Long term structural health monitoring by Brillouin fibre-optic sensing: a real case," J. Geophys. Eng. **9**, S64–S69 (2012).
2. A. Barrias, J. R. Casas, and S. Villalba, "A Review of Distributed Optical Fiber Sensors for Civil Engineering Applications," Sensors **16**, 1–35 (2016).
3. J. S. Selker, L. Thévenaz, H. Huwald, A. Mallet, W. Luxemburg, N. Van De Giesen, M. Stejskal, J. Zeman, M. Westhoff, and M. B. Parlange, "Distributed fiber-optic temperature sensing for hydrologic systems," Water Resour. Res. **42**, 1–8 (2006).
4. D. Y. Wang, Y. Wang, M. Han, J. Gong, and A. Wang, "Fully distributed fiber-optic biological sensing," IEEE Photonics Technol. Lett. **22**, 1553–1555 (2010).
5. S. Poeggel, D. Tosi, D. Duraibabu, G. Leen, D. McGrath, and E. Lewis, "Optical Fibre Pressure Sensors in Medical Applications," Sensors **15**, 17115–17148 (2015).
6. M. Majumder, T. K. Gangopadhyay, A. K. Chakraborty, K. Dasgupta, and D. K. Bhattacharya, "Fibre Bragg gratings in structural health monitoring-Present status and applications," Sensors Actuators, A Phys. **147**, 150–164 (2008).
7. Y. Dong, L. Chen, and X. Bao, "Time-division multiplexing-based BOTDA over 100 km sensing length.," Opt. Lett. **36**, 277–9 (2011).
8. I. R. Husdi, K. Nakamura, and S. Ueha, "Sensing characteristics of plastic optical fibres measured by optical time-domain reflectometry," Meas. Sci. Technol. **15**, 1553–1559 (2004).

9. B. L. Danielson, "Optical time-domain reflectometer specifications and performance testing," Appl. Opt. **24**, (1985).

10. X. Bao, D.-P. Zhou, C. Baker, and L. Chen, "Recent Development in the Distributed Fiber Optic Acoustic and Ultrasonic Detection," J. Light. Technol. **8724**, 1 (2016).

11. J. Pastor-Graells, H. F. Martins, A. Garcia-Ruiz, S. Martin-Lopez, and M. Gonzalez-Herraez, "Single-shot distributed temperature and strain tracking using direct detection phase-sensitive OTDR with chirped pulses," Opt. Express **24**, 13121 (2016).

12. Z. Qin, L. Chen, and X. Bao, "Distributed vibration / acoustic sensing with high frequency response and spatial resolution based on time-division multiplexing," Opt. Commun. **331**, 287–290 (2014).

13. Z. Zhang and X. Bao, "Distributed optical fiber vibration sensor based on spectrum analysis of Polarization-OTDR system.," Opt. Express **16**, 10240–10247 (2008).

14. J. Dakin, D. Pratt, G. Bibby, and J. Ross, "Distributed optical fibre Raman temperature sensor using a semiconductor light source and detector," Electron. Lett. (1985).

15. J. Song, W. Li, P. Lu, Y. Xu, L. Chen, and X. Bao, "Long-Range High Spatial Resolution Distributed Temperature and Strain Sensing Based on Optical Frequency-Domain Reflectometry," IEEE Photonics J. **6**, 1–8 (2014).

16. D. Yang, Z. Ding, D. Yang, Y. Du, and K. Liu, "Distributed Strain and Temperature Discrimination Using Two Types of Fiber in OFDR Distributed Strain and Temperature Discrimination Using Two Types of Fiber in OFDR," **8**, (2016).

17. W. Eickhoff and R. Ulrich, "Optical frequency domain reflectometry in single-mode fiber," Appl. Phys. Lett. **39**, 693–695 (1981).

18. J. Jasenek, "Capabilities and Limitations of Coherent Optical Frequency – Domain Reflectometry," **52**, 187–192 (2001).

19. T. Zhu, Q. He, X. Xiao, and X. Bao, "Modulated pulses based distributed vibration sensing with high frequency response and spatial resolution.," Opt. Express **21**, 2953–63 (2013).

20. Q. He, T. Zhu, X. Xiao, B. Zhang, D. Diao, and X. Bao, "All fiber distributed vibration sensing using modulated time-difference pulses," IEEE Photonics Technol. Lett. **25**, 1955–1957 (2013).

21. Y. Shi, H. Feng, and Z. Zeng, "Distributed fiber sensing system with wide frequency response and accurate location," Opt. Lasers Eng. **77**, 219–224 (2016).

22. H. F. Martins, S. Martin-Lopez, P. Corredera, M. L. Filograno, O. Frazao, and M. Gonzalez-Herraez, "Coherent noise reduction in high visibility phase-sensitive optical time domain reflectometer for distributed sensing of ultrasonic waves," J. Light. Technol. **31**, 3631–3637 (2013).

23. R. Bernini, A. Minardo, and L. Zeni, "Dynamic strain measurement in optical fibers by stimulated Brillouin scattering.," Opt. Lett. **34**, 2613–2615 (2009).

24. L. Zhou, F. Wang, X. Wang, Y. Pan, Z. Sun, J. Hua, and X. Zhang, "Distributed strain and vibration sensing system based on phase-sensitive OTDR," IEEE Photonics Technol. Lett. **27**, 1884–1887 (2015).

25. J. Hervás, A. L. Ricchiuti, W. Li, N. H. Zhu, and C. R. Fernández-pousa,

"Microwave Photonics for Optical Fiber Sensors," IEEE J. Sel. Top. Quantum Electron. **23**, 327–339 (2017).

26. J. Huang, X. Lan, Y. Song, Y. Li, L. Hua, and H. Xiao, "Microwave Interrogated Sapphire Fiber Michelson Interferometer for High Temperature Sensing," IEEE Photonics Technol. Lett. **27**, 1398–1401 (2015).

27. L. Hua, Y. Song, J. Huang, X. Lan, Y. Li, and H. Xiao, "Microwave interrogated large core fused silica fiber Michelson interferometer for strain sensing," Appl. Opt. **54**, 7181–7187 (2015).

28. B. Cheng, L. Hua, Q. Zhang, J. Lei, and H. Xiao, "Microwave-assisted frequency domain measurement of fiber-loop ring-down system," Opt. Lett. **42**, 1209 (2017).

29. A. L. Ricchiuti, J. Hervas, D. Barrera, S. Sales, and J. Capmany, "Microwave Photonics Filtering Technique for Interrogating a Very-Weak Fiber Bragg Grating Cascade Sensor," IEEE Photonics J. **6**, 1–10 (2014).

30. J. Huang, L. Hua, X. Lan, T. Wei, and H. Xiao, "Microwave assisted reconstruction of optical interferograms for distributed fiber optic sensing.," Opt. Express **21**, 18152–18159 (2013).

31. J. Huang, X. Lan, M. Luo, and H. Xiao, "Spatially continuous distributed fiber optic sensing using optical carrier based microwave interferometry.," Opt. Express **22**, 18757–69 (2014).

32. S. Liehr and K. Krebber, "Phase-OFDR for Distributed Disturbance Measurement," in *SPIE 9916, Sixth European Workshop on Optical Fibre Sensors* (2016), Vol. 9916, pp. 19–22.

33. J. Huang, X. Lan, M. Luo, and H. Xiao, "Spatially continuous distributed fiber optic sensing using optical carrier based microwave interferometry," Opt. Express **22**, 18757 (2014).

34. W. Mathlouthi, M. Menif, and L. A. Rusch, "Beat noise effects on spectrum-sliced WDM," in *SPIE 5260, Applications of Photonic Technology 6* (2003).

35. "Time Domain Analysis Using a Network Analyze," http://cp.literature.agilent.com/litweb/pdf/5989-5723EN.pdf.

36. J. Harris, "On then Use of Windows with the Discrete for Harmonic Analysis Fourier Transform," Proc. IEEE **66**, 51–83 (1978).

37. Rohde & Schwarz USA Inc., "Fundamentals of Vector Network Analysis," 46 (2011).

38. A. V Oppenheim, R. W. Schafer, and J. R. Buck, *Discrete Time Signal Processing* (1999), Vol. 1999.

39. J. Huang, T. Wang, L. Hua, J. Fan, H. Xiao, and M. Luo, "A coaxial cable fabry-perot interferometer for sensing applications.," Sensors (Basel). **13**, 15252–60 (2013).

40. M. Han and A. Wang, "Mode power distribution effect in white-light multimode fiber extrinsic Fabry-Perot interferometric sensor systems," Opt. Lett. **31**, 1202 (2006).

41. W. W. Morey, G. Meltz, and J. M. Weiss, "High-temperature capabilities and limitations of fiber grating sensors," in *10th Optical Fibre Sensors Conference*, B. Culshaw and J. D. C. Jones, eds. (International Society for Optics and Photonics,

1994), pp. 234–237.

42. W. Zhao and R. O. Claus, "Optical fiber grating sensors in multimode fibers," Smart Mater. Struct. **9**, 212–214 (2000).

43. M. Han and A. Wang, "Exact Analysis of Low-Finesse Multimode Fiber Extrinsic Fabry-Perot Interferometers," Appl. Opt. **43**, 4659 (2004).

44. E. Li, "Sensitivity-Enhanced Fiber-Optic Strain Sensor Based on Interference of Higher Order Modes in Circular Fibers," IEEE Photonics Technol. Lett. **19**, 1266–1268 (2007).

45. J. Huang, X. Lan, H. Wang, L. Yuan, T. Wei, Z. Gao, and H. Xiao, "Polymer optical fiber for large strain measurement based on multimode interference.," Opt. Lett. **37**, 4308–10 (2012).

46. Y. Liu and L. Wei, "Low-cost high-sensitivity strain and temperature sensing using graded-index multimode fibers," Appl. Opt. **46**, 2516 (2007).

47. D. Donlagic and B. Culshaw, "Propagation of the fundamental mode in curved graded index multimode fiber and its application in sensor systems," J. Light. Technol. **18**, 334–342 (2000).

48. H. Fu, W. Zhang, C. Mou, X. Shu, L. Zhang, S. He, and I. Bennion, "High-Frequency Fiber Bragg Grating Sensing Interrogation System Using Sagnac-Loop-Based Microwave Photonic Filtering," IEEE Photonics Technol. Lett. **21**, 519–521 (2009).

49. A. L. Ricchiuti, D. Barrera, S. Sales, L. Thevenaz, and J. Capmany, "Long fiber Bragg grating sensor interrogation using discrete-time microwave photonic filtering

techniques.," Opt. Express **21**, 28175–81 (2013).

50. J. Huang, X. Lan, H. Wang, L. Yuan, and H. Xiao, "Optical carrier-based microwave interferometers for sensing application," **9098**, 90980H (2014).

51. C. D. Butter and G. B. Hocker, "Fiber optics strain gauge.," Appl. Opt. **17**, 2867–9 (1978).

52. N. F. Borrelli and R. A. Miller, "Determination of the individual strain-optic coefficients of glass by an ultrasonic technique.," Appl. Opt. **7**, 745–50 (1968).

53. W. Wang, Y. Yu, Y. Geng, and X. Li, "Measurements of thermo-optic coefficient of standard single mode fiber in large temperature range," in *SPIE 9620,9620, 2015 International Conference on Optical Instruments and Technology: Optical Sensors and Applications, 96200Y* (2015), p. 96200Y.

54. L. Hua, Y. Song, J. Huang, B. Cheng, W. Zhu, and H. Xiao, "Femtosecond laser fabricated multimode fiber sensors interrogated by optical-carrier-based microwave interferometry technique for distributed strain sensing," **9754**, 97540V (2016).

55. L. Yuan, J. Huang, X. W. Lan, H. Z. Wang, L. Jiang, and H. Xiao, "All-in-fiber optofluidic sensor fabricated by femtosecond laser assisted chemical etching," Opt. Lett. **39**, 2358–2361 (2014).

56. O. Ziemann, J. Krauser, P. E. Zamzow, and W. Daum, *POF Handbook: Optical Short Range Transmission Systems* (2008).

57. D. X. Yang, J. Yu, X. Tao, and H. Tam, "Structural and mechanical properties of polymeric optical fiber," Mater. Sci. Eng. A **364**, 256–259 (2004).

58. J. Missinne, "Artificial skin based on flexible optical tactile sensors," SPIE

Newsroom 10–12 (2010).

59. K. Peters, "Polymer optical fiber sensors—a review," Smart Mater. Struct. **20**, 13002 (2011).

60. J. Zubia and J. Arrue, "Plastic Optical Fibers: An Introduction to Their Technological Processes and Applications," Opt. Fiber Technol. **7**, 101–140 (2001).

61. Y. Koike, T. Ishigure, and E. Nihei, "High-Bandwidth Graded-Index Polymer Optical Fiber," J. Light. Technol. **13**, 1475–1489 (1995).

62. C. Lethien, C. Loyez, J. P. Vilcot, N. Rolland, and P. A. Rolland, "Exploit the bandwidth capacities of the perfluorinated graded index polymer optical fiber for multi-services distribution," Polymers (Basel). **3**, 1006–1028 (2011).

63. J. Vucic and K.-D. Langer, "High-Speed Visible Light Communications: State-of-the-Art," in *Optical Fiber Communication Conference* (2012), p. OTh3G.3.

64. F. P. Beer, R. Johnston, J. DeWolf, and D. Mazurek, "Stress and Strain—Axial Loading," Mech. Mater. 57–69 (2011).

65. Z. S. Wu, B. Xu, T. Takahashi, and T. Harada, "Performance of a BOTDR optical fibre sensing technique for crack detection in concrete structures," Struct. Infrastruct. Eng. **4**, 311–323 (2008).

66. L. Hua, Y. Song, B. Cheng, W. Zhu, Q. Zhang, and H. Xiao, "Coherence-length-gated distributed optical fiber sensing based on microwave-photonic interferometry," Opt. Express **25**, 31362–31376 (2017).

67. R. John and S. a Boppart, "Coherence Imaging," Mol. Imaging 235–270 (2002).

68. Z. Chen, G. Hefferman, L. Yuan, Y. Song, and T. Wei, "Ultraweak Waveguide

Modification with Intact Buffer Coating Using Femtosecond Laser Pulses," IEEE Photonics Technol. Lett. **27**, 1705–1708 (2015).

69. Y. Song, L. Hua, J. Lei, Q. Zhang, J. Liu, L. Ye, and H. Xiao, "An IFPI Temperature Sensor Fabricated in an Unstriped Optical Fiber with Self-Strain-Compensation Function," J. Sensors **2016**, 6419623 (2016).

70. Y. Sorel and J. F. Kerdiles, "Simple measurement of fiber dispersion and of chirp parameter of intensity modulated light emitter," J. Light. Technol. **11**, 1937–1940 (1993).

71. S. C. Her and C. Y. Huang, "Effect of coating on the strain transfer of optical fiber sensors," Sensors **11**, 6926–6941 (2011).

72. C. Kirkendall, "Distributed acoustic and seismic sensing," in *OFC/NFOEC 2007 - Optical Fiber Communication and the National Fiber Optic Engineers Conference 2007* (2007).

73. A. Masoudi and T. P. Newson, "Contributed Review: Distributed optical fibre dynamic strain sensing," Rev. Sci. Instrum. **87**, (2016).

74. Y. Wang, B. Jin, Y. Wang, D. Wang, X. Liu, and Q. Dong, "Distributed fiber-optic vibration detection system," 2016 13th Int. Conf. Ubiquitous Robot. Ambient Intell. URAI 2016 277–278 (2016).

75. X. Fang, "A variable-loop sagnac interferometer for distributed impact sensing," J. Light. Technol. **14**, 2250–2254 (1996).

76. Q. Sun, D. Liu, J. Wang, and H. Liu, "Distributed fiber-optic vibration sensor using a ring Mach-Zehnder interferometer," Opt. Commun. **281**, 1538–1544 (2008).

77. H. F. Martins, S. Martin-Lopez, P. Corredera, M. L. Filograno, O. Frazao, and M. Gonzalez-Herraez, "Phase-sensitive optical time domain reflectometer assisted by first-order raman amplification for distributed vibration sensing over >100 km," J. Light. Technol. **32**, 1510–1518 (2014).

78. H. F. Martins, S. Martin-Lopez, P. Corredera, J. D. Ania-Castanon, O. Frazao, and M. Gonzalez-Herraez, "Distributed vibration sensing over 125 km with enhanced SNR using Phi-OTDR over a URFL cavity," J. Light. Technol. **33**, 2628–2632 (2015).

79. Z. N. Wang, J. J. Zeng, J. Li, M. Q. Fan, H. Wu, F. Peng, L. Zhang, Y. Zhou, and Y. J. Rao, "Ultra-long phase-sensitive OTDR with hybrid distributed amplification," Opt. Lett. **39**, 5866 (2014).

80. R. Paschotta, "relative intensity noise," https://www.rp-photonics.com/relative_intensity_noise.html.

81. J. Camparo and J. Coffer, "Conversion of laser phase noise to amplitude noise in a resonant atomic vapor: The role of laser linewidth," Phys. Rev. A **59**, 728–735 (1999).

82. I. D. M Cvijetic, *Advanced Optical Communication System and Networks* (n.d.).

83. X. Wang and K. I. Kitayama, "Analysis of beat noise in coherent and incoherent time-spreading OCDMA," J. Light. Technol. **22**, 2226–2235 (2004).

84. S. L. Woodward, J. W. Stayt, D. M. Romero, J. M. Freund, and G. J. Przybylek, "A study of optical beat interference between Fabry-Perot lasers," IEEE Photonics Technol. Lett. **10**, 731–733 (1998).

85. S. Okuyama, *Technology Trends & Issues in High-Speed Digital Systems* (n.d.).

86. R. Paschotta, "Fiber Amplifiers," .

87. C. M. Caves, "Quantum limits on noise in linear amplifiers," Phys. Rev. D **26**, 1817–1839 (1982).

88. R. Paschotta, J. Nilsson, A. C. Tropper, and D. C. Hanna, "Ytterbium-doped fiber amplifiers," IEEE J. Quantum Electron. **33**, 1049–1056 (1997).

89. J. L. Gimlett and N. K. Cheung, "Effects of Phase-to-Intensity Noise Conversion by Multiple Reflections on Gigabit-per-Second DFB Laser Transmission Systems," J. Light. Technol. **7**, 888–895 (1989).

90. S. Liehr, "Fibre Optic Sensing Techniques Based on Incoherent Optical Frequency Domain Refl ectometry," (2015).

91. D. S. Walker, W. M. Reichert, and C. J. Berry, "Corning 7059, Silicon Oxynitride, and Silicon Dioxide Thin-Film Integrated Optical Waveguides: In Search of Low Loss, Nonfluorescent, Reusable Glass Waveguides," Appl. Spectrosc. **46**, 1437–1441 (1992).